1975

Thermal stress initiated fracture as a fragmentation mechanism in the UO(2)-sodium fuel-coolant interaction.

Knapp, Roland Bertram

Massachusetts Institute of Technology

THERMAL STRESS INITIATED FRACTURE AS A FRAGMENTATION MECHANISM IN THE UO_2-SODIUM FUEL-COOLANT INTERACTION

Roland Bertram Knapp

THERMAL STRESS INITIATED FRACTURE AS A FRAGMENTATION MECHANISM IN THE UO_2-SODIUM FUEL-COOLANT INTERACTION

by

Roland Bertram Knapp

B.S., United States Naval Academy
(1969)

Submitted in Partial Fulfillment of the

Requirements for the Degree of

Naval Architect

and the Degree of

Master of Science in Nuclear Engineering

at the

Massachusetts Institute of Technology

May 1975

THERMAL STRESS INITIATED FRACTURE AS A FRAGMENTATION MECHANISM IN THE UO_2-SODIUM FUEL-COOLANT INTERACTION

by

Roland Bertram Knapp

Submitted to the Department of Ocean Engineering on May 9, 1975, in partial fulfillment of the requirements for the degree of Naval Architect and the degree of Master of Science in Nuclear Engineering at the Massachusetts Institute of Technology.

ABSTRACT

An analytic study was carried out to determine the applicability of the concept of thermal stress fragmentation to the UO_2/sodium Fuel-Coolant Interaction. Major emphasis was put on the fracture mechanics approach to assessing whether or not the solidifying UO_2 would fracture under the thermally induced stresses. It was found that the stress levels were sufficient to generate K_I values substantially in excess of the UO_2 fracture toughness, K_{IC}. Thus, rapid instantaneous propagation of inherent flaws is anticipated. Parametric studies in which the surface heat transfer boundary condition was varied did not alter this conclusion.

Extension of the thermal stress fracture concept to Al_2O_3 resulted in similar behavior. Subsequently, this material was selected as a good simulant for use in experimental studies of the mechanism. Additional studies on tin led to the conclusion that thermal stress fracture was not an applicable mode of fragmentation inducement in ductile metal/water interactions.

It was concluded that thermal stress fragmentation is a feasible mode of fragmentation in the UO_2/sodium system. However, further experimental and analytical work is necessary to establish firm verification of this model.

Thesis Supervisor: Neil E. Todreas

Title: Professor of Nuclear Engineering

Acknowledgements

It is with sincere gratitude that I express my appreciation to Professor Niel E. Todreas for his suggestions, constructive criticism and most importantly, his encouragement pertaining to the development of this work.

Discussions with and assistance from Professor Frank McClintok, Professor Warren Rohsenow, Professor Borijove Mikic, and peer critics William Idsinga and Daniel Golden were also most helpful.

My most heartfelt thanks go to my wife, Jean, who through the trying years of graduate school performed above and beyond the call of duty. Without her backing and understanding this work would not have been possible.

Sponsorship of this work was provided through the auspices of the Argonne National Laboratory and the U.S. Atomic Energy Commission.

Table of Contents

List of Figures

Nomenclature

a = position of the solidification front (radial)

A = surface area

Bi = (hR/k) = Biot number (nondimensional)

c = crack length

c_p = specific

E = modulus of electricity

E_n = energy

h = surface heat transfer coefficient

k = thermal conductivity (k_H-hot material, k_C-coolant material)

K = bulk modulus

K_I = stress intensity factor

K_{IC} = critical stress intensity factor (fracture toughness)

K_{IP} = stress intensity factor due to pressure stresses

K_{IT} = stress intensity factor due to thermal stresses

L = latent heat of fusion

m = mass

P = pressure in the solidifying droplet

r = radial position in solidifying shell

R = external radius of drop

r_y = radius of plastic zone at the crack tip

$\bar{r}$ = (a/r) = nondimensional solidification front position

$T(r,t)$ = temperature in solidifying shell

$\bar{T}(r,t)$ = $T_m - T(r,t)$

$T(a)$ = temperature at solidification front (= T_m)

T_m = melting point of molten material

T_c = coolant temperature

T_I = interface temperature (at r = R)

$T_s(t)$ = variable surface temperature (T_I)

t = time

$\bar{t}$ = $(kT_m t/LR^2)$ = nondimensional time

V = volume

α = thermal contraction coefficient

α' = thermal diffusivity

δ = vapor layer thickness

ρ = material density

σ_f = fracture stress

σ_r = total radial stress

σ_{rP} = radial pressure stress

σ_{rt} = radial thermal stress

σ_t = total tangential stress

σ_{tP} = tangential pressure stress

σ_{tt} = tangential thermal stress

ν = Poisson's ratio

(Note: a bar over a symbol indicates nondimensionalizing.)

CHAPTER ONE

INTRODUCTION

Possible accident situations, such as the melt down of a reactor core with the subsequent interaction of the fuel with the coolant, have been of major concern since the inception of reactor systems. It is known that sudden contacting of a hot liquid with a cold vaporizable one may result in a violent explosion. This process, regardless of whether explosive or not, will herin be referred to as a fuel-coolant interaction (FCI). The hot liquid is the fuel, the cold liquid the coolant, and the excess heat in the fuel provides the energy which drives the interaction. This type of interaction process is not limited to reactor systems. However, the fact that toxic radioactivity is coupled to the problem in reactors increases the hazards involved. Therefore, extensive safety analyses are a necessity in an effort to develop design constraints capable of minimizing the probability of such an accident occurring. These safety analyses will also provide an advance assessment of post-accident system behavior, and thereby allow for pre-planned measures of damage containment. This present work is linked to a portion of this type of

safety analysis, specifically concerning the liquid metal fast breeder reactor (LMFBR). In this particular case, the fuel is UO_2 and the coolant is liquid sodium.

The specific type of accident referred to above results from some type of power excursion, causing fuel element failure, which allows the dispersion of molten fuel in the liquid sodium. This accident situation, although highly unlikely, must be considered. The main concern is whether or not such an interaction of large quantities of molten fuel and coolant will yield vapor production fast enough to result in rapid pressurization coupled with the development of a local shock wave.

Although the precise outcome of the FCI is subject to speculation at present, existing models have resulted in predictions of sizeable amounts of mechanical work being generated from the thermal energy input (49, 65). Normally, in these models, a relatively large amount of fuel is assumed to interact with a small, constrained volume of coolant. Results substantiating such predictions have not been obtained experimentally for molten UO_2 in sodium. In one instance, though, where small amounts of liquid sodium were injected into molten UO_2 (the inverse experiment) high energy conversion rates were observed (20). Thus, a better assessment of the contact modes, energy transfer rates between the hot molten fuel and the coolant are required to better understand the interaction.

For explosive vapor generation to result from a fuel-coolant interaction, either an extraordinary heat transfer rate must occur, or the contact area for heat transfer must be increased substantially. The precise sequence of events and the controlling factors leading to such an explosion are subject to some controversy. There are essentially two basic themes as to what takes place. One centers around the spontaneous nucleation theory (74). In this case, perfect liquid-liquid contact, a lack of nucleation sites allowing for coolant superheating, and the elevation of the interface temperature to the spontaneous nucleation temperature are required. Spontaneous nucleation is predicted to result in extremely high pressure pulses. This mechanism does not occur in the case of the UO_2 in sodium interaction since the interface temperature remains below the spontaneous nucleation temperature of sodium.

The other proposed method of initiating explosive vapor generation is based on the assumption that one of the fluids (normally the fuel) fragments, rapidly increasing the surface area available for heat transfer. Experimental fragmentation of UO_2 in sodium has resulted only in low order pressurizations (20). However, if the interaction is constrained to a small volume of the coolant as mentioned above, existing models predict that potentially large amounts of mechanical work could be generated.

It is not known whether fragmentation is a required condition for vapor explosions. Yet knowledge of the process itself would permit evaluation of the known low-pressure interactions, and the resultant impact on the reactor system as a whole in an accident situation.

The present lack of understanding of the fragmentation process in a UO_2-sodium FCI and the inability to accurately predict the subsequently generated heat transfer area prohibits formulation of an accurately descriptive accident model, based on the second theme, for use in design. As long as this lack of understanding persists, the time dependent, mixing phenomena will remain unknown.

The broad spectrum of experimental and analytical work reviewed in the next chapter demonstrates the wide variety of concepts considered thus far. It appears that for the specific case of fragmentation in the UO_2-sodium FCI, the solid shell theories are the most promising. Specifically, the thermal stress mode of fragmentation during solidification, which is the one under consideration here, is the most promising.

This work is primarily intended to further evaluate and extend the thermal stress fragmentation theory. Of primary interest is the determination of the solid UO_2 shell's susceptibility to fracture under the developed stresses. Of secondary importance is an evaluation of the effect on the fracture potential of gases covering the

surface of the UO_2 particles undergoing thermal stress fracture. As well, an estimate of the constraint provided by the solidifying UO_2 surrounding liquid sodium is made (the inverse problem). Finally, the applicability of thermal stress fracture to other simulant systems is included.

In conducting this analysis, extensive use was made of the existing experimental works and analytical models described herein. Hopefully, the results advance the "state-of-the-art" one step closer to allowing for a realistic evaluation of potential LMFBR accident situations involving a fuel-coolant interaction.

CHAPTER TWO

REVIEW OF EXPERIMENTAL AND THEORETICAL STUDIES OF MOLTEN MATERIAL/COOLANT THERMAL INTERACTIONS

2.1 Introduction

The complexity of the fuel-coolant interaction and the lack of understanding associated therewith are illustrated by the extensive number of published articles relating to this and its associated problems. The following is an attempt to enumerate and briefly summarize some of the major experimental studies conducted to date. Reactor system safety analyses, as well as work in non-nuclear fields, have generated numerous studies of thermal interactions involving a wide variety of materials. Until recently, published work concerning molten UO_2 and sodium was somewhat limited. In today's energy-conscious world, however, the push for LMFBR completion has stimulated a more concentrated effort in this particular area. This review is by no means all-inclusive, but the intent is to point up some of the important results recorded thus far.

2.2 Experimental studies

Active experimental programs have been undertaken internationally involving numerous materials. In recent

years, reported experimental work related to the molten fuel-sodium interactions has come out of the international CREST meetings at Grenoble in 1972 and Ispra in 1973, in particular. A summary of presentations at the former can be found in Ref. 1 and of those at the latter in Refs. 2 and 3.

Earlier work concerning the fuel-coolant interaction, i.e., during the 1950's and 1960's, was primarily directed at thermal reactors utilizing a water coolant. The emergent problem was found to be extremely complex and the actual mechanisms involved, as well as the interdependence of such mechanisms still remain somewhat in question. The majority of the work done with respect to the thermal reactor systems is not directly applicable to the LMFBR. However, it has been the valuable experience gained from such studies that has paved the way for the more recent fast reactor analyses.

2.2.1 Accidental thermal explosions

Accidental thermal explosions encountered in industry resulting from the sudden contact of molten metals with damp surfaces or cool liquids have been recorded (4, 5) and reviewed (6) covering a time frame extending from the middle 1800's to the last decade. Some of these accidents have resulted in extremely heavy damage, and in some cases have even been responsible for numerous deaths.

An early indication that a metal-water thermal interaction is a potential safety problem in reactor systems resulted from the core meltdown accident of the NRX Canadian test reactor in 1952. This accident, as well as others which can be explained in terms of high energy thermal interactions are directly responsible for the research push into this particular area. Reference 7 provides a good summary of these accidents and their causes. Following the NRX accident, a set of destructive reactor experiments was conducted in the Borax reactors. As reported by Dietrich (8), the melting of the fuel plates and the following contact of the molten metal with the water coolant resulted in the generation of extremely high pressures of approximately 6-10,000 psi.

In another accident involving an experimental reactor, the EBR-1, the first case of a core meltdown with a coolant other than water was encountered. In this instance, the coolant was NaK and a large destructive explosion did not take place. During post-accident analysis the remains were found to be in a porous condition. It was subsequently postulated by Kittel (9) that vaporization of entrained NaK may have been responsible for the observed spongy remains. Post-accident analysis of the well-known SL-1 boiling water reactor accident (the first fatal reactor accident) pointed strongly to a violent molten metal-water reaction following fuel element meltdown as being responsible

for the extensive damage incurred (10). The magnitude of the pressures developed was enormous as the reactor vessel rose approximately nine feet off its foundation. Further destructive experimental test results, such as those from the SPERT reactor tests, tend to support conclusions that thermal interactions, and not nuclear explosions, resulting from extremely rapid vapor generation cause the destructive mechanical work.

2.2.2 Laboratory experiments

As a result of the accidents enumerated above, extensive experimental research into the mechanisms responsible for thermal interactions was initiated. Some of the earliest experiments were conducted by Long (6), followed later by Elgert and Brown (11). These experiments all centered around Molten metal-water interactions. A significant outcome of such studies was the ruling out of chemical reactions as a causative mechanism. This hypothesis was later verified analytically through a study of chemical reaction kinetics by Epstein (12).

The experiments conducted by Long (6), which are becoming something of a clasic in the field, consisted of pouring fifty pounds of molten aluminum into a tank containing water. He concluded that a thin layer of water trapped between the molten metal and the container vaporized and thereby initiated fragmentation of the molten aluminum.

The resulting fragments allowed an increased rate of heat transfer to the surrounding water and thereby created an explosion. This mechanism has since been entitled the entrapment theory. In an attempt to further substantiate his theory, Long demonstrated that when the container was coated with grease, no longer allowing entrapment, the interaction was suppressed. Further verification of Long's results was subsequently provided by Hess and Brondyke (13). Other experiments, such as those of Sallack (26) on the quenching of paper smelt, culminated in a proposal that the mechanism for spontaneous fragmentation of the molten material resulted from the vaporization of liquid entrained in cracks in the melt's solidified surface.

2.2.3 Small-scale dropping experiments

Experimental investigation of the fragmentation of small molten drops in cold liquids has been a fairly widespread method of analysis. More emphasis has been placed on this particular mode of contact as it is believed to be somewhat representative of the type of results expected in a UO_2-sodium free contact situation. A good review of the results of these particular experiments can be found in Ref. 14.

Experimenters at Argonne National Laboratory (ANL) have conducted numerous dropping experiments consisting of dropping various materials into liquid sodium (15-18). Some

of the earliest of these experiments were carried out by Swift and Pavlick (16). A significant observation was the fact that initially solid materials, when dropped, were simply quenched by the sodium. Molten samples, on the other hand, fragmented, and it was later found that this applies to molten uranium (17) and UO_2 (20), as well. Other important results include the decreasing size of fragments with increasing initial temperature (18), and the enhancement of fragmentation with increased sodium pool temperature up to a peak value, followed by decreasing fragmentation with further increases (15).

Resulting from a strong desire for "observability", water has become widely utilized as the coolant for experimental applications. Swift and Pavlik (16, 17) extended the scope of their experiments by using water as well as sodium in the coolant pool. A major finding was the fact that while some molten metals will fragment in sodium, they will not in water. To ensure that these results were not dependent on an oxide film effect, they utilized noble metals (Ag and Au) and the results were the same. In an effort to explain these results the violent-boiling theory of fragmentation was postulated (16). It was thought that perhaps the turbulence associated with the violent boiling of either the nucleate or transition regimes was responsible for initiating breakup. Then, based on Westwater's (21) demonstration that under

equilibrium conditions nucleate boiling occurs below the fluid critical temperature, fluids with a low critical temperature would tend to quench the molten material in the quiet film region allowing solidification. However, those with a high critical temperature may incur violent boiling prior to solidification resulting in fragmentation. This seems compatible with the observed results in water and sodium. It must be noted that this mode of fragmentation has not been observed in the case of UO_2 in sodium (17).

In an isothermal investigation conducted by Ivins (22) consisting of mercury dropping into room temperature water, a Weber Number effect was observed. For values above a certain critical contact velocity fragmentation occurred. The fragmentation was considered to be a hydrodynamic phenomenon which occurred as a result of inertial forces overcoming the surface tension of the drop. It was shown by Hinze (23), in a further study of the hydrodynamic mode of fragmentation that a critical value of the Weber Number results in fragments that are stable in nature. The attempt was to validate a method of fragmentation for coolants which exceed their critical temperature, but the results have not proven universally true.

Cho (15) attempted to show the dependence of the extent of fragmentation on the initial temperature of the hot material and the coolant temperature for different molten materials dropped into water. The results demonstrated that

there is no consistent pattern as to the extent of fragmentation when altering the hot material temperature. It was concluded, however, that decreasing the coolant temperature results in an increase in fragmentation.

Qualitative discussions of similar experiments (molten metal-water) reported by Brauer (24) and Flory (25), supporting the ideas of enhanced fragmentation with increasing Weber Number, and decreasing pool temperature, have yielded additional observations. No violent boiling occurred around the hot material and fragmentation took place almost immediately following contact. It was observed (25) that fragmentation resulted from an outward burst of the metal and that the residue was spongy in appearance. In the specific case of aluminum, many of the drops swelled into hollow thin-shelled "bubbles", some of which later burst. Further, chemically reducing the molten material's surface tension increased the tendency for fragmentation while similarly increasing the viscosity of the water reduced fragmentation. The resulting interpretation led the investigators to believe that encapsulation of the coolant in the hot material via surface instabilities (Helmholtz instabilities) was responsible for the observed fragmentation mechanism. Alternative encapsulation mechanisms have also been proposed (19, 26, 27).

Amblard et al. (19) observed that in UO_2/water experiments no fragmentation took place. This was subsequently confirmed by Witte et al. (28). In an attempt to extend their results to the case of UO_2/sodium, Amblard et al. proposed that either an encapsulation mechanism or thermal stresses developed in the UO_2, or a combination of both may be responsable for fragmentation in this system.

In contrast to the above, some large-scale experiments consisting of dropping kilogram quantities of UO_2 into a pool of sodium were conducted by Johnson et al. (50). The UO_2 was heated to 5500°-5800°F via a thermite-type reaction. These experiments were similar to the small-scale experiments conducted at ANL (15) and the results were similar as well. Extensive fragmentation occurred but the interactions were mild in nature, and large pressure pulses of low energy content were observed.

In a follow-on effort aimed at more precisely identifying the actual mechanism leading to fragmentation, Stevens et al. (30) conducted experiments on transient film and transition boiling around spheres in water. It was observed that when the sphere temperature was lowered below a point where stable film boiling could be sustained, a very rapid collapse of the film layer took place. This rapid film collapse was suggested as a feasible method of fragmentation inducement.

Experiments consisting of dropping molten tin into water as reported by Board et al. (31) have revealed yet another set of observations. Various perturbations consisting of varying the tin temperature, varying the water temperature, changing the system pressure and introducing external mechanical impulses were carried out. The results led to the conclusion that fragmentation was triggered by the development of unstable film boiling between the two liquids. The main cause of dispersion was determined to result from vapor collapse which possibly generated a small coolant jet that penetrated the molten material, dispersed, and resulted in fragmentation.

In an extension of his initial experiments, Board (31) investigated the effect of rapid vapor-blanket collapse. Once the molten material was in the coolant a rapid pressure increase was initiated by rupturing a diaphragm, thus collapsing the vapor blanket surrounding the molten material. An explosion was generated following the blanket collapse. These results were obtained using both tin and aluminum as the hot material and they seemed to confirm his earlier hypothesis.

Other molten metal/water experiments conducted by Witte et al. (31a) using low melting point materials (mercury, lead, zinc, bismuth, tin and aluminum) appear to further substantiate Board's hypothesis. The results lead to a rejection of earlier theories, and resulted in the

conclusion that fragmentation is a response to an external stimulus while the sample is still molten. It was further concluded that vapor film collapse was a highly likely, indirect initiating mechanism, while the direct mechanism for fragmentation was seen as being one of pressure differences, surface tension changes, or a thermal shock phenomenon. The results, however, were not sufficient to detail the exact cause of fragmentation.

2.2.4 Coolant injection experiments

Small-scale coolant injection experiments have been carried out at ANL utilizing various combinations of materials. Armstrong and Cho (15) injected small amounts of water at room temperature into a variety of molten materials. Both above and subsurface injections were carried out, and in some cases explosive interactions were recorded. Anderson and Armstrong (32) noted that the existence of a gas layer between the two fluids seemed to prevent development of an explosion (similar to observations in Ref. 29 on the inverse experiment).

Other experiments involving the injection of molten metal jets into water were reported in Ref. 29. The jet surface temperature had a major impact on the extent of fragmentation. Additionally, when the jet was blanketed by a vapor film the initiation of fragmentation could be completely suppressed. Prior to the fragmentation explosion

a bulge in the jet was noticed (at the point of subsequent fragmentation), similar to the phenomenon reported earlier by Flory (28).

Small-scale coolant injection experiments have also been carried out utilizing sodium into UO_2. The results are similar to those noted for water, as in some cases explosions developed, and a comparable time delay was observed. In this particular case it was suggested that fragmentation of the coolant, followed by mixing with the molten material, resulted in the explosive interaction. An alternative explanation offered by Fauske (33) suggests that spontaneous nucleation of superheated sodium may have been the cause. He does not, however, exclude the possibility of an alternative mode of coolant fragmentation prior to spontaneous nucleation.

2.2.5 Shock tube experiments

Another of the early efforts to ascertain the mechanism driving the high pressure levels encountered during a reactor accident led to a series of experiments designed so as to impart a significant thermal transient to the coolant via a heat source (34, 35). The results demonstrated that rapid heating of water from a flat surface and thereby producing vaporization yielded relatively low pressures. These pressures were even lower if non-condensable gases were present. Subsequently, the experimental methodology

was reviewed and a new type of experiment was devised: that of utilizing a shock tube. Shock tube experiments consist of supporting a column of liquid coolant above the hot material via a diaphragm, then puncturing or removing the diaphragm and allowing the liquid column to impact on the hot material. Wright (36) conducted shock tube experiments with water as the coolant and alternatively solid and molten aluminum, silver and UO_2 powder as the hot material. When solid materials were used, only low pressures were developed. However, when impacting molten materials, very high (nearly 6,000 psi) pressures were obtained, as well as dispersion (fragmentation) of the material. The resulting pressure was directly related to the molten material temperature, and the duration of pressure build-up was on the order of 0.5 msec. Hillary and Darby (1) later verified Wright's results and showed that non-condensable gas in the interaction zone (under low pressure) can stifle the explosive interaction altogether.

Holtbecker et al. (1) utilized a sodium column in a shock tube impacting on alumina at 2670° K. Their results demonstrate repeated small-magnitude pressures too low to be destructive.

2.2.6 In-pile testing

Extensive fuel pin failure experiments involving molten fuel-coolant interactions have been performed as a part of

thermal reactor safety studies (37, 38, 39). Recently a parallel effort concerning in-pile experiments related to LMFBR systems safety has been taking place (40-47), and a summary of recent tests can be found in Ref. 48. The bulk of the LMFBR fuel pin failure studies have been carried out in the Transient Reactor Test Facility (TREAT). Data with respect to the threshold and mode of fuel-element failure, movement of fuel during transient heating, swelling, melting, and post failure effects of fuel-coolant interactions has been recorded.

In an attempt to derive information relating to the pressures and the mechanical energy generated in molten fuel-sodium interactions, ANL set up the stagnant sodium piston-autoclave tests (S-series). These tests provide the most significant results relating to the fuel-coolant interaction in an LMFBR as a result of an over-power transient. Here the energy input yielding fuel melting and pin failure is actually supplied by a nuclear power pulse. The resultant fuel-coolant interaction involves fragmentation and pressure pulse generation. Yet, the energy conversion (nuclear to mechanical) is several orders of magnitude less than the maximum thermodynamic limit (49). Analytical interpretation of these experiments by Epstein and Cho (47) shows that the molten fuel was the only fluid capable of performing expansion work and that the liquid sodium acted as an energy-dissipative fluid rather than a working fluid.

It appears likely that the initial pressure pulses and mechanical work measured results from fuel vapor pressure and bond-gas pressurization without involving any process of rapid sodium vaporization (48). Similar results have been obtained in the E and H series tests which use flowing sodium, and L and R series tests which simulate a loss of flow. That is, in all cases only mild interactions with a low energy conversion ratio have been observed. Further, the results of the UO_2-sodium interactions experiments indicate that the energy conversion ratios are less than for the UO_2-water case, for a comparable nuclear energy input (38, 39).

The overall outcome of the TREAT experiments, although limited in scope, have provided valuable information and have advanced the understanding of fuel-failure mechanisms. It has been demonstrated, however, that large-scale vapor explosions are not a necessary outcome of a reactor transient. This remains to be verified analytically and/or experimentally.

2.3 Theoretical studies

In attempting theoretical investigations of the problem, two basic approaches have been undertaken. The first consists of attempting to parametrically model the overall thermal interaction from either a thermodynamic point of view, estimating the maximum work available, or from a

transient, rate-limited viewpoint. The second approach breaks the problem down to a subsystem level and involves studying only the possible mechanisms which lead to fragmentation of the fuel. In all cases it has been the intent to enable one to ascertain the energy conversion rates and subsequent mechanical work generated, the effect on the reactor system dynamics, and specifically the potential for large-scale vapor explosions.

2.3.1 Thermodynamic models (parametric)

The first attempt at determining the destructive work potential of a molten fuel-sodium interaction was carried out by Hickes and Menzies (49). It was a limiting case calculation which resulted in an upper bound on the expansion work available from the coolant. Initially upon contact the fuel and coolant were assumed to be in thermal equilibrium, sharing the thermal energy which had been previously stored in the core fuel. Then the resulting internal energy change which would be incurred by the fuel under an isentropic expansion to atmospheric pressure was taken to represent the work potential available. Later work has offered up modifications, perturbations and improvements to this original model (50, 51, 52, 53), with the most notable being that of Judd (52), which utilizes a more accurate equation of state for high-temperature sodium.

Although this type of thermodynamic approach provides an upper bound for the problem, it does not take into account the transient heat transfer and expulsion rates which actually occur, nor does it allow for the time dependence of the pressure rise or the mechanical work generation. As the problem is a dynamic one, the time dependence should be a key parameter in any realistic model.

2.3.2 Rate-limited parametric models

In an attempt to account for the transient nature of the fuel-sodium interaction, models which describe it in terms of time-dependent pressurization, voiding and rate-limited heat transfer have been developed. These models vary between those investigating a local interface phenomenon and those which assure that the fuel fragments and disperses within the coolant.

Models of the limited interface type which have been proposed (54, 55) yield values on the opposite end of the spectrum from those of Hicks and Menzies (49). In these models, the heat transfer is assumed to stop following vaporization of sodium at the interface and the pressure work developed from a shock wave produced in the coolant is then evaluated. The speed at which vaporization takes place (less than 1 msec) accounts for the low work potentials developed.

A model designed to incorporate the transient intertependence between the heat-transport and expansion

processes was developed by Padilla (56). He formulated the problem as consisting of spherical fuel particles uniformly distributed and in intimate contact with liquid sodium in an interaction region. It was further assumed that boiling was suppressed and that the liquid sodium was restrained by the remaining colder sodium from expanding when heated. The energy transfer to the sodium results in pressurization and subsequent acceleration of the surrounding liquid. Once the sodium pressure falls below the saturation pressure of the heated zone, the onset of boiling occurs. At this point the heat transfer to the sodium ceases and an isentropic expansion continues. During the heating process the only mechanism for pressure release results from the compressibility of the liquid plug above the interaction region. In this model, the effects of condensable and non-condensable gases are neglected, which could affect the peak pressures calculated. In addition, it may not be on the conservative side to assume heat transfer cutoff at the inception of boiling as it does not allow for energy transfer to the system during boiling.

Building on Padilla's model, Cho et al. (57) at ANL developed a parametric model for the fuel-coolant interaction (ANL-FCI). A significant variation from the original formulation was that of allowing for a rate-limited generation of fuel surface area, accounting for the finite fragmentation and mixing rate of the fuel in sodium. The

time-dependent area generation formula was not based on any physical picture of the process involved, and altering the generating time constant allows significant variation in the maximum pressures attainable (predicted). It was demonstrated that non-condensable gases reduced peak pressures as well as delaying its time of occurrence. To allow for the inclusion of non-condensable vapor blanketing of the fuel in thermal resistance, a later option has been added to the model (58). As a result of parametric studies using the ANL model (59), it has been demonstrated that noncoherence in the interaction leads to reduced mechanical work. However, this reduction is estimated to be small for realistic mixing times.

Similar model development has taken place in other countries, and reviews of principal aspects have been presented by various authors (1, 2, 3, 60). The majority of these models have followed the above Cho-Padilla type formulation. The approach is to consider that particle dispersion has already taken place and that the fuel is contained in a finite volume of sodium prior to the interaction. Variations in the postulated heat transfer mechanisms, particle size and distribution, mixing modes, equations of state utilized, etc. contribute to the variations in predicted pressures.

An initial attempt at the incorporation of a fragmentation model in the overall fuel-coolant interaction

calculation has been set forth by Grossgut et al. (61). Here, both solidification of the fuel and hydrodynamic impact forces are considered. Results appear to agree favorably with experiments. However, as pointed out by Caldarola (2), the number of parameters in the model may allow the generation of reasonable results just through a judicious choice of numerical values.

The large number of optional parameters involved in any and all of the models generated thus far, coupled with the degree of uncertainty involved preclude blind acceptance of their results. They do, however, provide a convenient mechanism for sensitivity analysis of these various parameters. Two of the basic inputs which have a strong influence on the generated pressure and mechanical work are the contact mode and the fragmentation phenomenon, and until these can be determined with a reasonable degree of accuracy, the predictions of parametric models will be in doubt.

2.3.3 Models for specific applications

Models of this type are developed for a contact mode determined by the specific casualty sequence under consideration. A typical model of this type is that based on a jet-type ejection of molten fuel through an orifice in a failed fuel rod (62). Two others are the multichannel core dissembly code (FISFAX) (63), and ANL's

SAS/FCI (64) model. The latter is primarily based on the ANL-FCI parametric model discussed previously. These models are strongly dependent on the underlying assumptions for the specific postulated accident, and their results are severely restricted in applicability.

2.3.4 Fragmentation theory

An excellent review of fragmentation theories/models to date has been compiled by Cronnenberg and Grolmes (65). As a result, only a generalized look into these models will be given here, with only significant details noted. As fragmentation and the subsequent mixing, contact, etc. of the fuel and coolant are major determining factors in evaluating the amount of mechanical work developed in a fuel-coolant interaction it is of great importance to understand these phenomena. As can be seen from the quantity and variety of theories proposed thus far it is evident that this understanding is largely lacking at present.

It is convenient for organizational, comparative and discussion purposes to divide the existing models into three categories as per Ref. 65. These classes consist of: those models associated with hydrodynamic effects between the molten material and coolant independent of thermal conditions, the molten droplet models which assume that the liquid material is readily deformable and

undergoes fragmentation due to pressure forces initiated in the coolant, and the solid shell theories which consider thermal cooling effects and surface solidification.

One type of hydrodynamic fragmentation model is that based on impact fragmentation as postulated by Hinze (23). This model, as previously cited, was based on a Weber Number dependence and the fact that a critical Weber Number corresponded to the onset of the fragmentation phenomenon. Another of the postulated hydrodynamic models is that based on Helmholtz surface instabilities (25, 66, 67). Wave-like ripples which encapsulate coolant leading to breakup are postulated to form on the hot material's surface. These shear-induced waves depend on relative velocities of the materials and their magnitude and frequency depend on the material viscosities. A serious contradiction results as fragmentation has been shown to occur when only low or no velocities of consequence exist.

The most widely postulated models are those based on a molten droplet form for the hot material. One mode of fragmentation falling into this group is that as suggested by Swift and Baker (68) involving vapor bubble growth and collapse. Considerable effort has been given to this mode of fragmentation, and variations thereon (7, 15, 69). In the dynamic bubble collapse mechanism set forth by Caldarola and Kastenberg (70) the destructive energy is considered as derived from the impingement of microjets generated via

bubble collapse. This formulation was a result of evaluation of photographic experiments (71). The jet impingement is described as generating an elastic wave in the molten material which then generates acoustic energy resulting in fragmentation.

The results of calculations based on these molten drop models, with sodium as the coolant, indicates that the maximum thermodynamic work potential is more than that necessary to account for the observed fragmentation. However, when estimating the actual amount of energy converted it is found insufficient to result in fragmentation. Thus, as fragmentation is known to occur, a more definitive estimate of the percent of energy conversion is required.

Another of the molten drop models consists of the generation of an acoustic pressure pulse in the coolant (69). The pressure pulse is a result of thermal expansion of sodium at the fuel-coolant interface as a result of heat transfer. However, again the maximum work potential is smaller than that required for fragmentation.

Still another possibility is that of the previously noted concept of spontaneous nucleation of the coolant following liquid-liquid contact as considered by Fauske (72). Whereas this mechanism is plausible for some metal-water interactions, the UO_2-sodium contact temperature is lower than the spontaneous nucleation

temperature of sodium. It has been pointed out, however, that for large amounts of UO_2 surrounding a small sodium droplet the requirements for spontaneous nucleation can be met (73).

A final molten drop mechanism is that based on internal acoustic cavitation in the hot material (14). In this case surface boiling generates internal pressure waves which then produce internal cavitation leading to breakup.

Epstein (75) has proposed a violent gas release mechanism from a metastable supersaturated solution as a fragmentation mechanism. This model is in a category of its own, and is highly dependent on the solubility of gases in the molten material. As of now the mechanical work potential of this model has not been calculated. A significant fact is that such a mechanism is capable of accounting for the sponge-like appearance of some fragmented materials.

In contrast to the molten drop models, recent efforts to take into account the possibility of solidification of the hot material have resulted in solid shell theories of fragmentation (76-79). Initially, Hsiao et al. considered the pressurization of a solidifying sphere of aluminum in an infinite water cooling medium. It was concluded that the tangential stresses will exceed the radial stresses and that the maximum surface tangential stresses occur as solidification begins, which should allow for immediate

rupture. Ref. 77 extended Hsiao's results to the case of UO_2 and sodium with similar results. The cornerstone of these models is the solidification kinetics of the hot material. For the case of UO_2-sodium (78, 79), the time for molecular reordering was found to be short compared to the time constant for heat transfer. Fragmentation is assumed to result from coolant penetration of fissures developed in the outer frozen shell or from boiling within these cracks. The fact that the surface stresses developed in the solidifying shell are found to exceed the yield strength of UO_2 by several orders of magnitude led to the conclusion that fracture should occur. The actual fracture mechanisms, as well as the energy conversion rates, and the particle size and distribution rates have not as yet been determined.

CHAPTER THREE

THERMAL STRESS GENERATION

3.1 Introduction

The solid shell theory of fragmentation, under consideration here, appears to be consistent with the limited experimental observations (i.e., Armstrong, Ref. 20) for the case of UO_2-Na. The work conducted to date (75-76), although limited in scope, has shown it to be both feasible and relevant. As pointed up in the literature review, the fracture mechanisms, time scales, particle size distribution, etc. have not, as yet, been determined. In order to make use of this fragmentation theory in an overall Fuel-Coolant Interaction model, these quantities must be known. Thus, the ability to determine them in a straightforward analytic manner is highly desireable. Prior to making an attempt at extending the theory, a brief review of the solid-shell fragmentation theory is necessary to obtain a first-order estimate of the desired quantites. This existing theory will then provide the foundation for fracture calculations and time scale estimations.

The analysis consisted of making use of Adams's (82) approximate solution to the heat conduction equation for a constant surface temperature to determine the liquid-solid interface velocity with time. The constant temperature boundary condition was determined from the contact interface temperature formulation of Ref. 83. Utilizing molten UO_2 initially at its melting point (2800°C) and 200°C sodium, an asymptotic solid-liquid interface velocity of 2 cm/sec was found to exist for times greater than 1 msec (Figure 3.2). This result was based strictly on heat transfer considerations.

Secondly, classical crystallization theory was used to determine the rate of crystal growth in the melt (see, for example, Ref. 78). Based on the maximum solid-liquid interfacial surface tension the homogenous nucleation temperature was determined to be 700°C below the melting point of UO_2. A more realistic estimate of the solid-liquid interfacial energy was made and this value was then revised to be a few hundred degrees. If any nucleation sites are activated prior to this temperature, heterogenous nucleation would be initiated and solidification would commence immediately. Nonetheless, for the UO_2-Na temperatures under consideration, the contact interface temperature is well below even the lower limit homogenous nucleation temperature and solidification is sure to occur. An investigation of the various temperatures associated

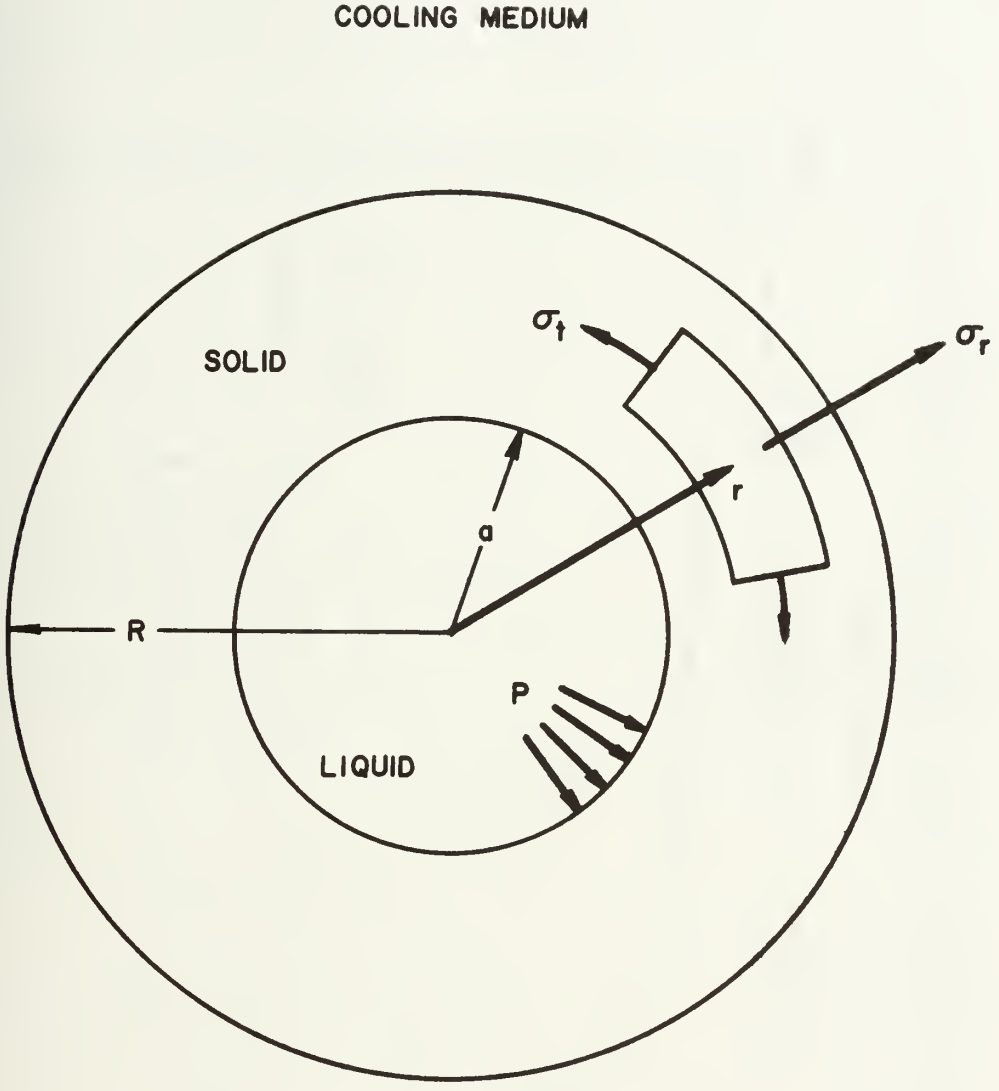

Figure 3.1--Model for solidification induced stresses.

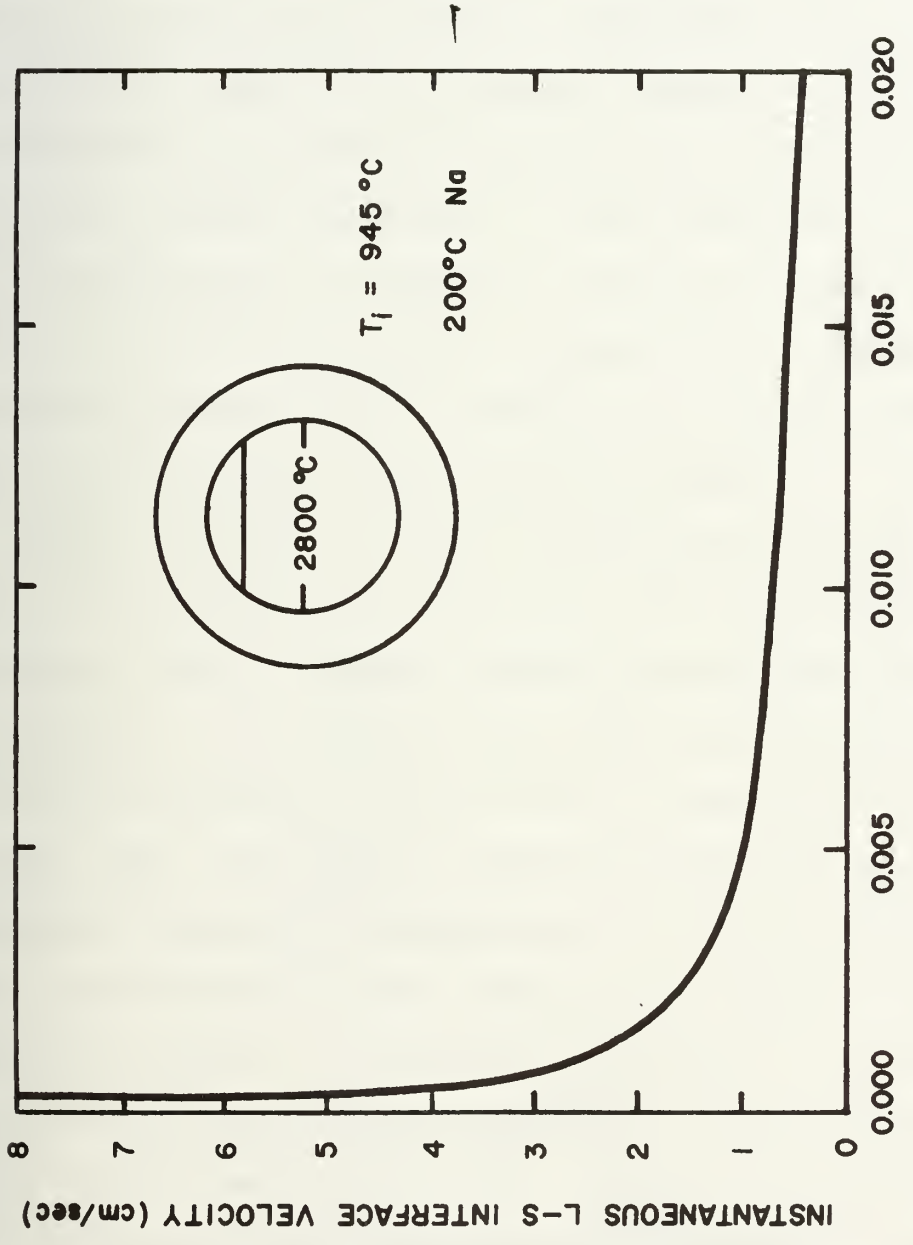

Figure 3.2--The velocity of the liquid-solid interface versus time determined from the heat transfer process (77).

with all realistic LMFBR accident conditions revealed that this would also be the case. The net rate of crystallization for the 1218°K contact interface (the same as that used in the heat transfer calculations) was found to be 71 cm/sec (Figure 3.3). When this value was compared to the mean solidification velocity of approximately 2 cm/sec found from heat transfer conditions, it was concluded that the UO_2 solidification is limited by the heat transfer process and not the time for molecular reordering. Consequently, it can be assumed that the solidification begins immediately upon contact of the molten UO_2 with sodium.

Armed with the fact that solidification of UO_2 will occur, and the knowledge that Hsiao (76) had demonstrated the feasibility of thermal stress fragmentation, an evaluation of the pressurization and thermal stresses in the UO_2-Na system was carried out by Cronenberg et al. (77). In this case, the effects of temperature dependence of the mechanical properties, compressibility of the molten liquid core, and variation of the surface heat transfer conditions were investigated. In conducting parametric evaluations of the validity of various assumptions, both Al-water and UO_2-Na systems were analyzed for comparative purposes.

The solution for the temperature-dependent thermoelastic stress problem of Ref. 84 was used for rotationally symmetric stress and strain. It was further noted that for the case of constant properties and a Poisson's ratio less than 0.5,

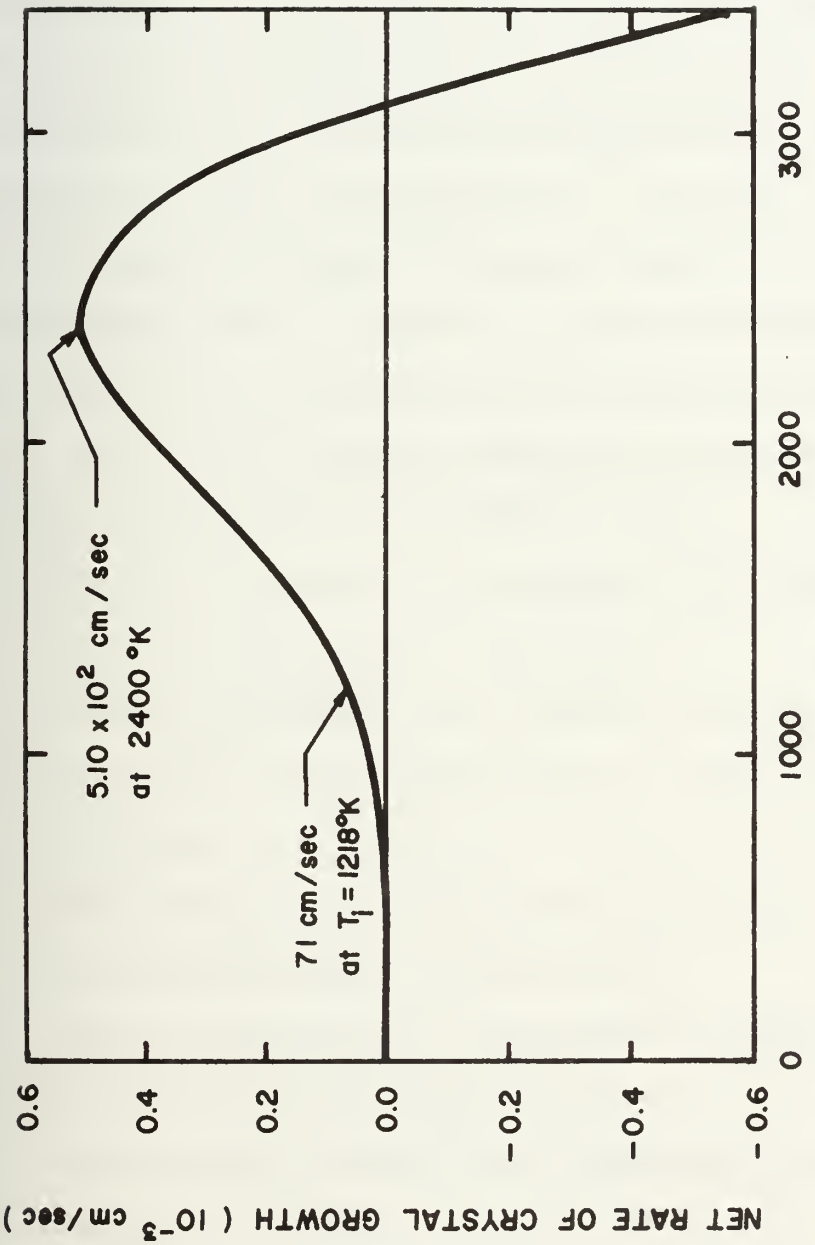

Figure 3.3--Net rate of solid growth versus temperature as determined from crystallization theory (77).

3.2 Solid shell fragmentation theory

The initial attempt at analytically modeling the fragmentation of solidifying hot material in a coolant was that of Hsiao (76). His investigation was centered around determining the pressurization of a solidifying sphere of molten material in an infinite cooling medium (in his case, aluminum and water, respectively). In order to attack the heat-conduction problem (a partial differential boundary value problem with a nonlinear surface boundary condition) the steady-state approximation of London and Seban (80) was used. To gain the desired approximate solution, the following assumptions were imposed (76):

1. The molten material was taken at the uniform melting temperature, initially.
2. Thermal properties were taken as constant.
3. The unit surface conductance, h, was taken as constant.
4. The temperature of the liquid phase was considered uniform and constant.
5. The hot material was considered to have a discrete melting temperature.
6. The density of both phases was taken as the same.

In addition, the molten material was taken as a small sphere, suddenly immersed in the coolant; solidification was assumed to begin instantaneously, and the compressibility

of the liquid core was neglected. The geometry of the situation is as illustrated in Figure 3.1.

Based on the foregoing assumptions, the steady-state approximation was then employed to obtain an evaluation of the rate of solidification front movement and the temperature profile in the solidified shell. Then, calculating the induced pressure and the thermal gradient, the pressure and thermal stresses were evaluated. The maximum total stress was found to occur in a tangential direction at the surface of the drop, almost immediately after solidification began. It was concluded that if the temprature was such as to yield stress levels which exceed the ultimate tensile stress of the shell, failure would occur.

The stress calculations were based on elasticity theory, and in light of the observations of Ref. 81 concerning the high strain rate and rapid temperature change, modeling the material behavior as elastic was considered adequate.

Before extending this type of model to the UO_2-Na system, Cronenberg et al. (78, 79) investigated the validity of the assumption of solidification initiation upon contact. The analysis was based on a calculation of the crystallization kinetics in an effort to determine if the time for molecular reordering to form solid from the melt is short compared to the heat transfer time constant.

the pertinent equations reduced to the familiar form (85)

$$\sigma_r = \frac{2\alpha E}{1-\nu}\left[\frac{r^3-a^3}{(R^3-a^3)r^3}\int_a^R \bar{T}(r,t)r^2dr - \frac{1}{r^3}\int_a^r \bar{T}(r,t)r^2dr\right] - \frac{Pa^3(R^3-r^3)}{r^3(a^3-R^3)} \quad (3.1)$$

$$\sigma_t = \frac{2\alpha E}{1-\nu}\left[\frac{2r^3+a^3}{2(R^3-a^3)r^3}\int_a^R \bar{T}(r,t)r^2dr + \frac{1}{2r^3}\int_a^r \bar{T}(r,t)r^2dr - \frac{1}{2}\bar{T}(r,t)\right] + \frac{Pa^3(2r^3+R^3)}{2r^3(a^3-R^3)} \quad (3.2)$$

$$P = \frac{6\alpha E}{R^3+2a^3-\nu(4a^3-R^3)+\frac{2}{3}\frac{E}{K}(R^3-a^3)}\int_a^R \bar{T}(r,t)r^2dr \quad (3.3)$$

where $\bar{T}(r,t)$ is the temperature difference between the present and initially unstressed states.

In order to determine the thermal stresses, both the temperature and the velocity of the solidification front need to be evaluated. For constant thermophysical properties, the Fourier heat conduction equation in spherical geometry was formulated as

$$\alpha'\left[\frac{\partial^2 T(r,t)}{\partial r^2} + \frac{2}{r}\frac{T(r,t)}{2r}\right] = \frac{\partial T(r,t)}{\partial r} \quad (3.4)$$

with α' the thermal diffusivity, and the initial condition being

$$T(r,o) = T_m \quad (3.5)$$

The liquid-solid interface conditions are given as

$$k\left.\frac{\partial T(r,t)}{\partial r}\right|_{r=a} = \rho L\frac{da(t)}{dt} \quad (3.6)$$

for an energy balance, and

$$T(a,t) = T_m \tag{3.7}$$

for continuity.

The external surface boundary condition is

$$-k \left.\frac{\partial T(r,t)}{\partial r}\right|_R = h(T_s(t) - T_c) \tag{3.8}$$

where the coefficient of heat transfer, h, is dependent on the mode of heat transfer.

In contrast to the convective boundary condition, the previously mentioned constant contact interface temperature condition could exist if perfect wetting occurs (a highly likely situation). In this case, the interface temperature is given as

$$T_I = \frac{T_H(k_H/\sqrt{\alpha_H}) + T_C(k_C/\sqrt{\alpha_C})\text{erf } \lambda}{(k_H/\sqrt{\alpha_H}) + (k_C/\sqrt{\alpha_C})\text{erf } \lambda} \tag{3.9}$$

where H and C denote the hot and cold materials respectively. Incorporation of the erf λ term results from the movement of the solidification front in the UO_2 and its value is determined from the transcendental equation (77)

$$\left(\frac{C_p T_m}{L\sqrt{\pi}}\right)_{UO_2} = \lambda e^{\lambda^2}\left[\frac{k_H\sqrt{\alpha_C}}{k_C\sqrt{\alpha_H}} + \text{erf } \lambda\right] \tag{3.10}$$

for UO_2 liquid initially at its melting point. The values for bulk UO_2 at its melting point in 200°C sodium are given as: $\lambda = 0.94$, erf $\lambda = 0.82$, and the temperature of the interface is 945°C (77). The contact interface temperature will remain approximately constant for as long as the UO_2 and Na remain in contact and the entire UO_2 sphere has not solidified.

The number of approximate solutions is extremely limited, especially for spherical geometry. In the study under discussion here, two separate approaches were taken. First, a numerical solution of the equations was utilized in an effort to include transient effects. Second, an analytic solution based on the constant surface temperature condition was employed. The constant surface temperature solution utilized the approximate solution of Adams (82) with the temperature in the solidified shell given as

$$T(r,t) = T_I(t) - \frac{L}{\alpha' C_p}\left(\frac{R-r}{Rr}\right) a^2 \frac{da}{dt} + a\left(\frac{da}{dt}\right)^2 \frac{L}{C_p}\left(\frac{1}{\alpha'}\right)^2 \left(\frac{R-r}{R-a}\right) \times \left(\frac{R}{3} - \frac{r}{6} - \frac{a^2}{2r} + \frac{a^3}{3Rr}\right) \tag{3.11}$$

with the freezing rate given as:

$$\frac{da}{dt} = \frac{2\alpha' C_p (T_m - T_I)}{(La - La^2/R)\left(1 + \sqrt{1 + \frac{4}{3}\frac{R}{a}\frac{C_p}{L}(T_m - T_I)}\right)} \tag{3.12}$$

The position of the solid-liquid interface at any time is found by integrating the above equation.

Of major interest in the initial heat transfer analysis was the determination of the proper cooling surface boundary condition and its range of applicability. A comparison was made between the constant surface temperature condition and a convective nucleate boiling heat transfer coefficient. The selection of the nucleate boiling coefficient for use was based on the prediction of Henry's correlation (86) which required a temperature of 9500°C for Na film boiling. Figure 3.4 illustrates the

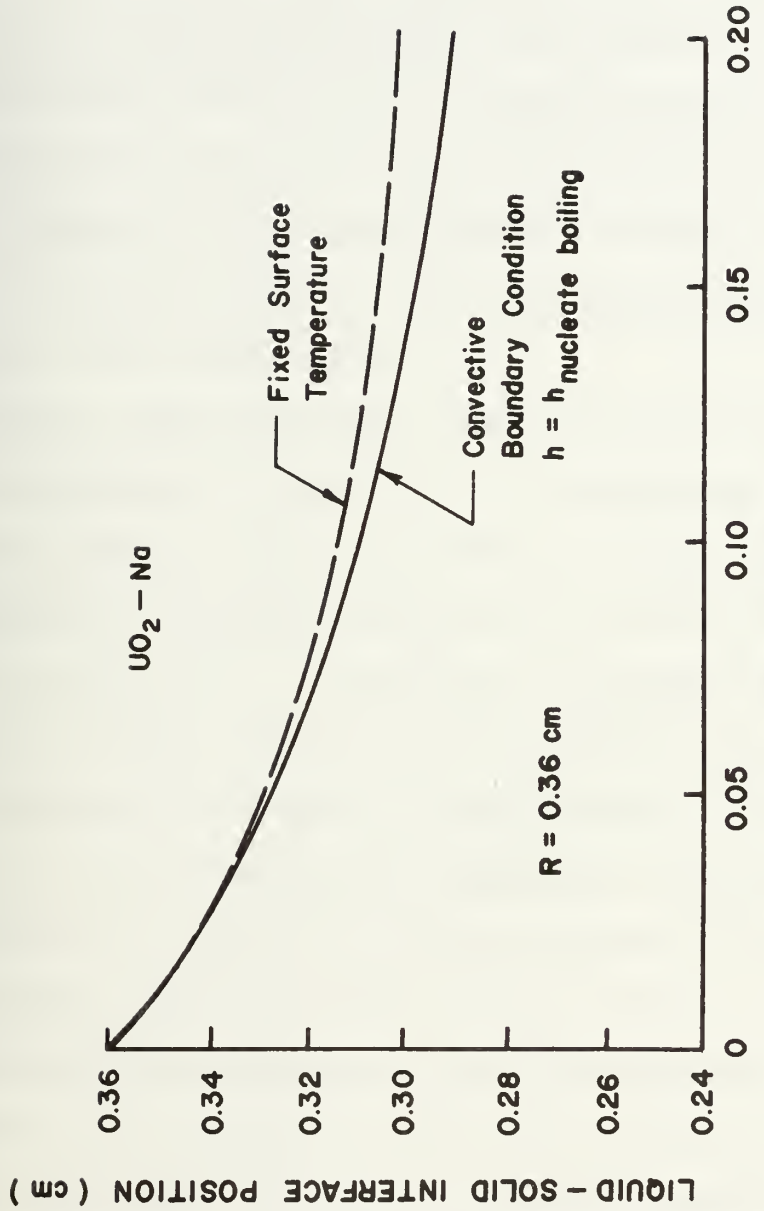

Figure 3.4--Comparison between the solidification rates for a convective heat transfer boundary condition and a constant surface temperature (76).

effect of changing the surface boundary condition on the liquid-solid interface position. As stated (77), the solidification of UO_2 in Na is limited primarily by its low conductivity and not by the heat transport process, and the choice of the cooling surface boundary condition is not extremely critical for $h = h_{\text{nucleate boiling}}$, especially over short times.

Several other parametric evaluations were carried out by Cronenberg, as well (77). A comparison of the transient numerical solution with the steady-state approximation of London and Seban (80) used by Hsiao (76) was made (Figure 3.5). The results indicated that neglecting thermal inertia, as the steady-state approximation does, results in deviation of the solution. It was further found that using temperature independent properties (with mean values of α and E) or varying Poisson's ratio from 0.3 to its upper limit of 0.5 had little effect. Similarly, the limited compressibility of the molten liquid core only produced a small decrease in the internal pressurization.

As was found in Ref. 76, the total tangential stress at the surface was the dominant factor in the UO_2-Na case, as well. Figure 3.6 illustrates the thermal, pressurization, and total stress components at the outer surface as a function of time. The total surface tangential stress is shown to go through a maximum at approximately 50 msec after quenching, a value in line with the observed breakup

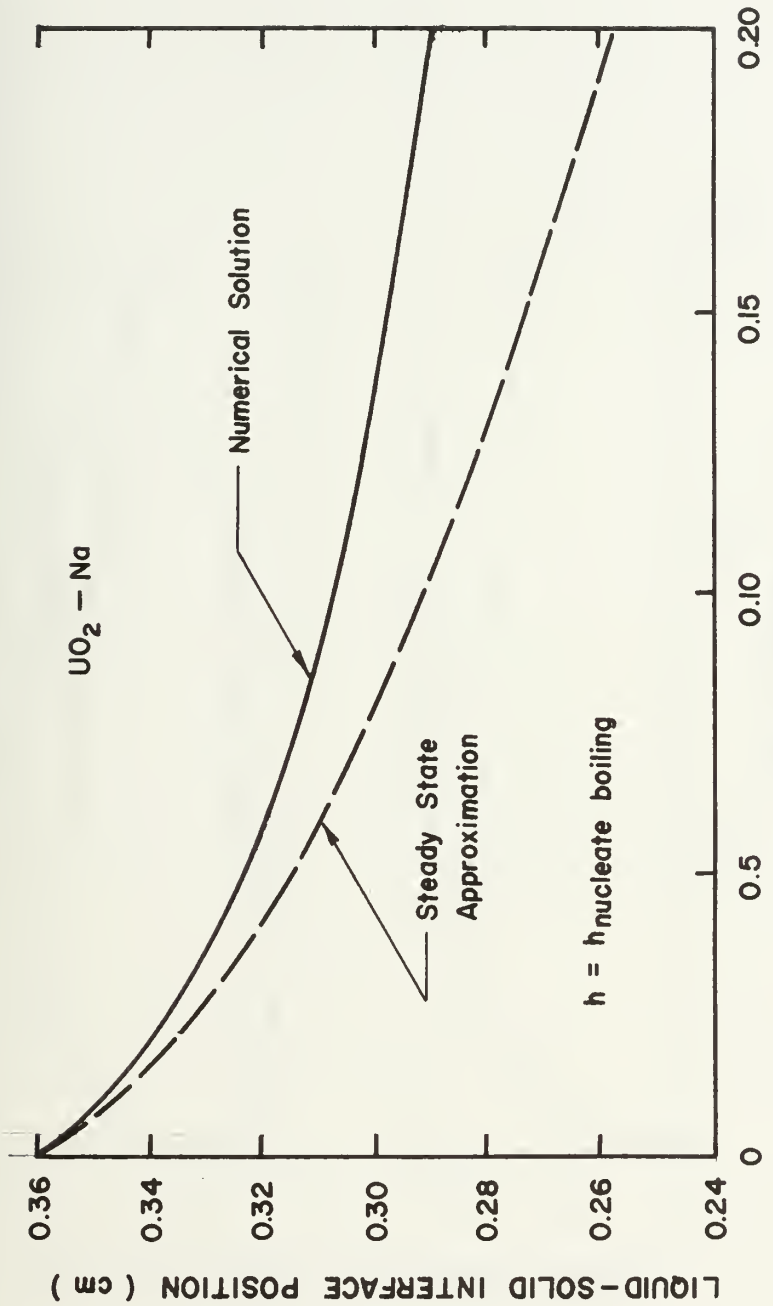

Figure 3.5--Comparison of the transient numerical heat transfer solution with the steady-state approximation for the convective boundary condition (76).

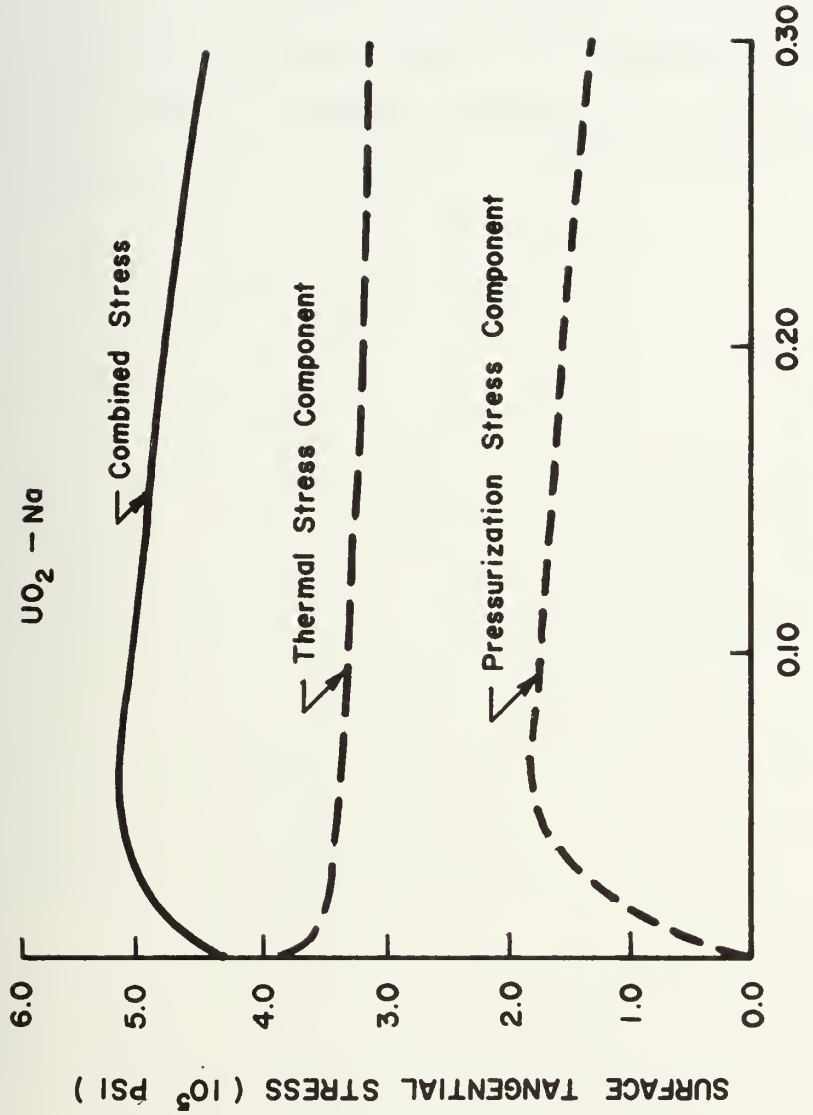

Figure 3.6--The outer surface tangential stress components versus time; UO_2 in Na ($\sigma_t(O^-) = 0.0$; $\sigma_t(O^+) = \infty$) (76)

time of UO_2 in Na observed experimentally (20). This point coupled with the fact that the total stress at the surface exceeds the yield stress of UO_2 (5000 psi at 2000 C) by a significant amount led to the conclusion that the thermal stress theory of fragmentation in the case of UO_2 in sodium is indeed plausible and it deserves further consideration.

CHAPTER FOUR

FRACTURE THEORY

4.1 Introduction

The intent here is to briefly review some basic theories of fracture of ideal solids, the fundamentals of the fracture mechanics approach to fracture analysis, and the alternative surface energy criterion for fracture in ceramics. As all work on the fuel-coolant interaction to date has been based primarily on heat transfer/thermodynamic type analyses, a review of these basics was considered essential prior to attacking the modeling concept considered here. Although this treatment is somewhat superficial, it is believed that the concepts and terminology will provide sufficient understanding where application of the principles of fracture is required.

4.2 Crack propagation in homogenous materials

In an ideal, homogenous, isotropic, elastic solid, the tensile strength is on the order of its molecular cohesion force. While the strengths of small whiskers, or carefully produced fibers, are found to approach this value, the experimental strengths of bulk material are generally only 1/1000 - 1/100 of the ideal value. The reason for

this discrepancy, as explained by Griffith (87), is the presence of small flaws or cracks which result in severe stress concentrations in even the unstressed state. Thus, even though the average stress in the solid may be relatively low, the theoretical fracture strength can be locally exceeded.

When attacking the problem from an energy standpoint, it can be seen that when a material is stretched, the interatomic spacing of planes of atoms is increased. This increase in distance is proportional to the stored elastic energy. It is this potential energy, as ascertained by Griffith (87), that provides the surface energy required to form new surfaces during fracture. For most materials, other than the most brittle, it has since been found (88) that a significant amount of the apparent effective surface energy is absorbed in plastic flow and the formation of branch cracks. Furthermore, when fracture propagates at high speed, energy is lost in the production of sonic waves (88).

Griffith's analysis was for a plane flat plate of two dimensions with a stationary central crack, elliptical in shape. He allowed the crack to become very sharp at its ends. Then, assuming Hooke's Law valid, he extended Inglis' analysis (87) to calculate the critical nominal stress. Inglis described the locally magnified stress at the crack tip as:

$$\sigma_{max} = 2\sigma\sqrt{\frac{c}{\rho}} \tag{4.1}$$

where σ_{max} = stress at crack tip

σ = applied nominal stress

c = half crack length

ρ = radius of curvature at the crack tip

The radius of a sharp crack tip is difficult to measure, and so σ_{max} cannot easily be evaluated by this formula. Griffith therefore extended the analysis based on energy considerations. From the stress distribution around the elliptical crack, he determined the stored elastic strain energy. Then, equating this stored energy to the energy required by the newly formed surfaces, he found the critical stress to cause crack propagation (for plane strain conditions):

$$\sigma_c = \sqrt{\frac{2E\gamma}{\pi c(1-\nu)}} \tag{4.2}$$

where

σ_c = critical applied nominal stress causing fracture

E = Young's modulus of elasticity

c = crack half length

γ = fracture surface energy

ν = Poisson's ratio

Under conditions of plane stress, this equation becomes:

$$\sigma_c = \sqrt{\frac{2E\gamma}{\pi C}} \tag{4.3}$$

In the above, plane stress is defined as a state of stress which is described in every volume element by a set of principle stresses, one of which is zero. Generally, a plane stress condition exists in thin sections in which the stress normal to the surface is nearly zero. On the other hand, plane strain is defined as a state of stress which results in a zero strain along a specific direction.

Prior to the initiation of crack growth, in the Griffith theory, the system strain energy increases directly with the applied stress. Once the growth begins, however, the change in strain energy becomes a function of the magnitude of both the crack opening kinetic energy and the energy required to form new crack surfaces (surface energy). The kinetic energy here results from the fact that as the ends of the crack move forward, the material at the sides of the crack moves apart with a finite velocity. Thus, a kinetic energy can be associated with this movement of material near the end of the crack. This kinetic energy, initially zero, increases as the crack grows. This relation can be graphically illustrated as shown in Figure 4.1, as a function of the half crack length.

The locus of the stress and strain at the onset of crack instability can be illustrated as shown in Figure 4.2. Then, where the stress-strain curve of the material intersects this locus, fracture should occur. Typically,

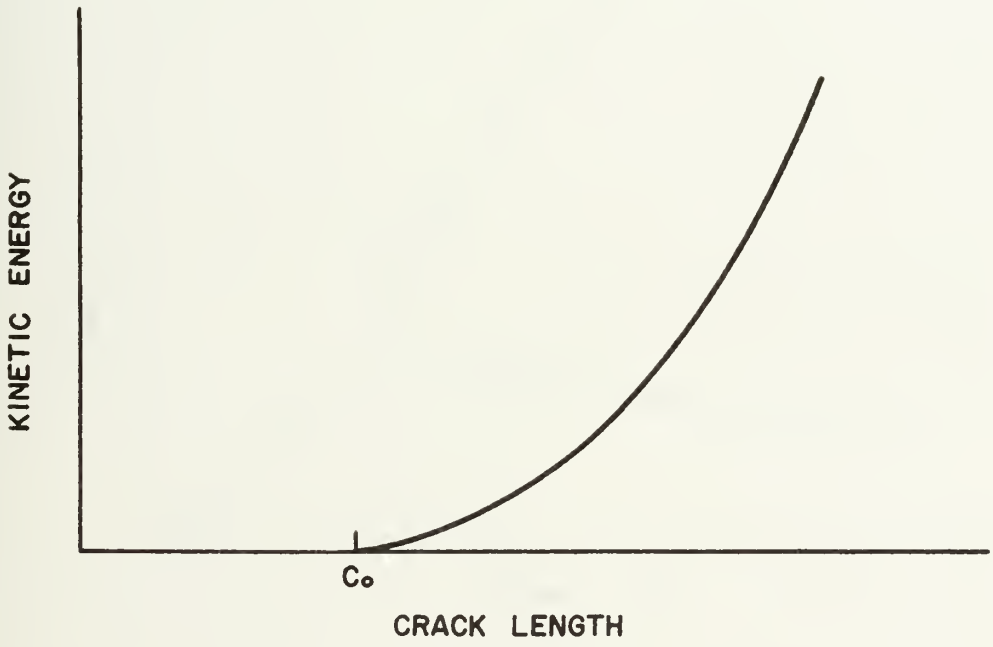

Figure 4.1--Kinetic energy versus half crack length (89).

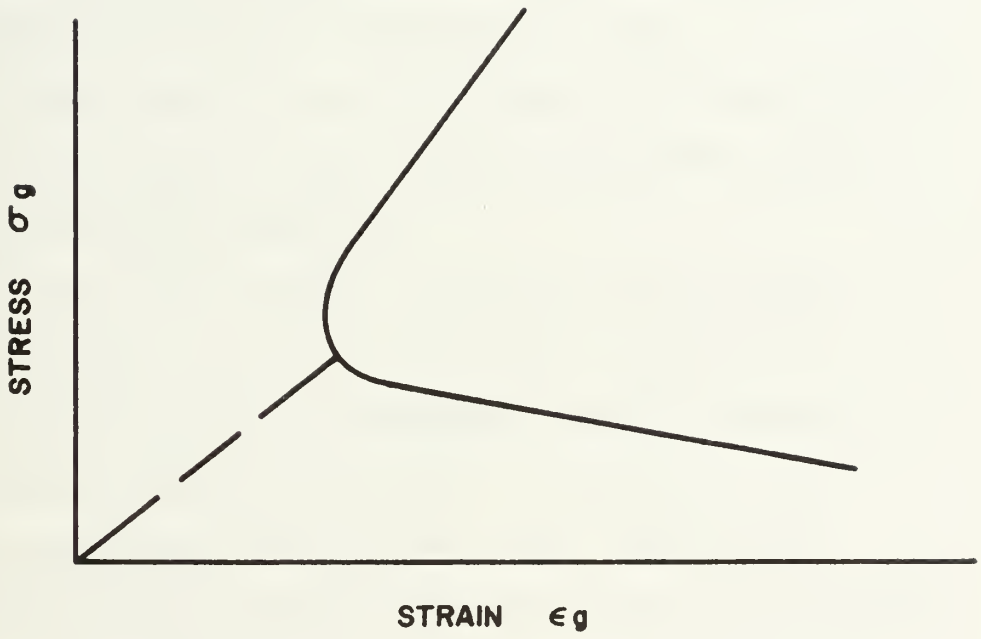

Figure 4.2--Stress-strain relation based on Griffith criterion

the point of intersection occurs in the region where the slope of the locus is positive. The possible discrepancy between observed fracture stress values and those predicted by the Griffith equation (4.2) is related to the angle between the stress-strain curve of the sample and the locus at the point of intersection. With increasing crack length, the value of this angle approaches ninety degrees, where the Griffith criterion is satisfied. The implication is that, due to the difference in the strain-energy stored prior to fracture, a small crack would have a higher starting velocity than a large one.

Further, the kinetic energy, fracture surface energy and the strain energy can all be determined graphically from the fracture locus (89). Consider a sample containing a crack of length 2c which is extended to fracture, with the ultimate stress maintained during crack propagation. If the path OAB shown in Figure 4.3 is followed, the breakdown of the work into its various energy components, at any time following the onset of crack propagation, can be determined (Fig. 4.3).

Sack (90) and Sneddon (91) extended the Griffith criterion to a two-dimensional crack (disk shaped) in a three-dimensional solid. The basic assumption underlying this analysis is that the tensile strength of the brittle material in one direction is unaffected by the stresses at right angles to it. Then the highest allowable stress

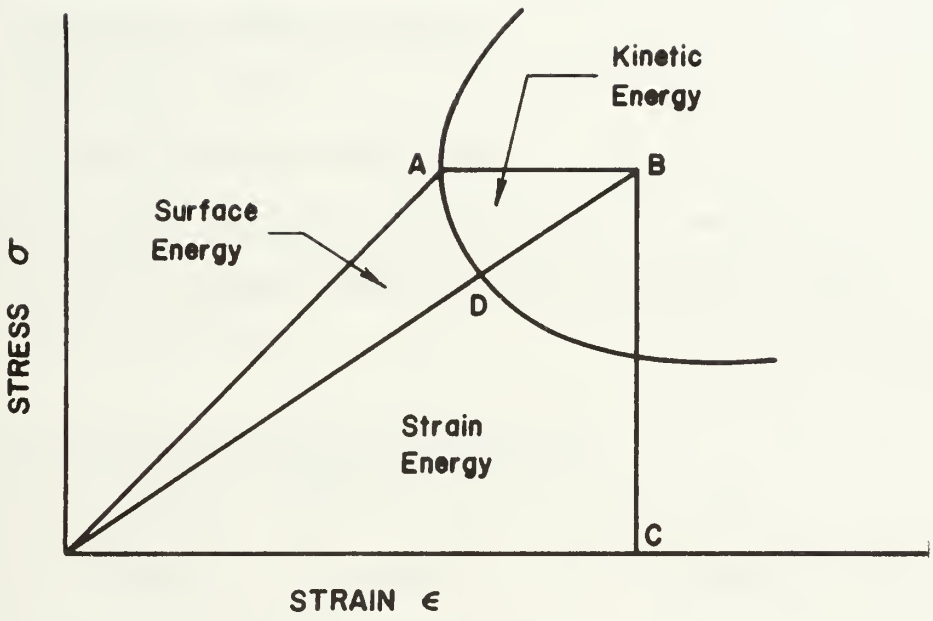

Figure 4.3--Graphical determination of fracture surface energy and kinetic energy (89).

normal to the plane of the crack is given by:

$$\sigma_c = \sqrt{\frac{\pi E \gamma}{2c(1-\nu^2)}} \qquad (4.4)$$

where

σ_c = nominal stress applied perpendicular to the plane of the crack to cause fracture

E = Young's Modulus of elasticity

γ = fracture surface energy

ν = Poisson's ratio

c = radius of the disk (crack)

Depending on the value of Poisson's ratio for the material, σ_c from equation (4.4) differs from Griffith's solution by a factor of 1.57 to 1.8 (90, 91).

4.3 Crack propagation velocity and branching

The crack propagation velocity is dependent upon various factors, including: the material, the imposed stress pattern, and the amount of stored strain energy at the time of fracture initiation. There is a velocity limit, referred to as the terminal velocity, and it is a material property. When the available energy exceeds that necessary to propogate the crack at its terminal velocity, the excess will appear in other forms or it will cause crack oscillation or branching.

In comparing theoretical and experimental values (92) of the terminal crack velocity in brittle materials, it has been found that the governing factor is the kinetic

energy supply. The extent to which the kinetic energy is supplied to various parts of the body determines the terminal velocity. The terminal crack velocity is then given as (92):

$$V = 0.38 \sqrt{\frac{E}{\rho(1-\nu^2)}} \sqrt{1 - \frac{c_o}{c}} \qquad (4.5)$$

V = terminal crack velocity

E = modulus of elasticity

ρ = density of the material

c_o = original length of the crack

c = extended length of the crack

ν = Poisson's ratio

It has been found that the terminal crack velocity is independent of the surface energy, and that the stress state in the material surrounding the crack is approximately equal to that in the static case (92, 93, 94). The foregoing solution yields a terminal velocity of approximately 38% of the velocity of sound in the material: $\sqrt{E/\rho}$.

The relationship between crack velocity and the stress required to sustain it can be seen in Figure 4.4: the stress decreases with increasing speed (88). Therefore, once a crack is initiated, it may continue to propagate even though the stress level decreases. It is possible then to have catastrophic propagation even under a rapidly decreasing load (i.e., decreasing from a maximum). Since the crack tends to be self-sustaining at high velocities,

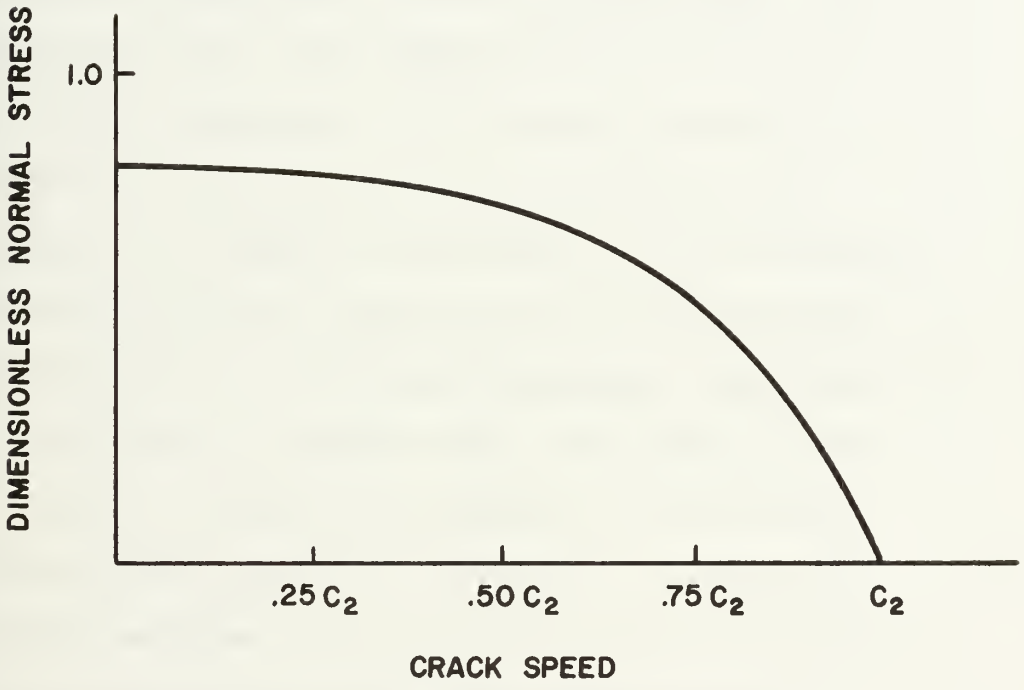

Figure 4.4--Tensile stress to sustain crack velocity versus propagation velocity (92).

it is reasonable to assume that branching must occur prior to the occurrence of this condition.

It is possible to obtain a solution for a two-dimensional crack in a three-dimensional medium by evaluating the stresses and displacements in a semi-infinite solid (95). In this case, it has been found that the terminal crack velocity is again independent of the surface energy (96). The conclusion was that a two-dimensional crack moves in one plane, with no branching, at a constant velocity.

When the Griffith criterion is satisfied by the stress condition in a sample, the sample is in an unstable state and crack propagation begins with an infinitesimal increase in the stress. Practically speaking, the stress would then continuously increase until the sample breaks. The actual fracture stress value depends on the loading rate and the specimen geometry. Figure 4.5 illustrates the relationship between the crack length and the elapsed time following crack initiation. The time required to obtain a given crack length decreases as the applied stress increases. The reason for this behavior results from the different initial velocities of crack propagation for different stress levels. However, the terminal velocity is the same for all levels; this is illustrated in Figure 4.6. Figure 4.6 also shows that for lower stress levels, a longer crack is required prior to attaining the terminal velocity.

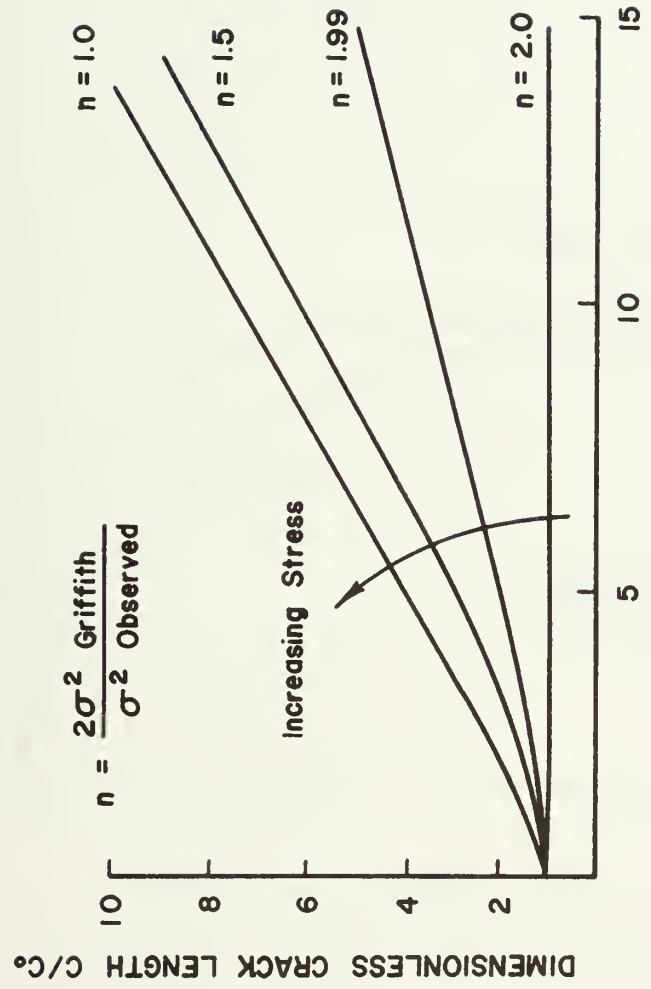

Figure 4.5--Crack length versus elapsed time after initiation of crack (89).

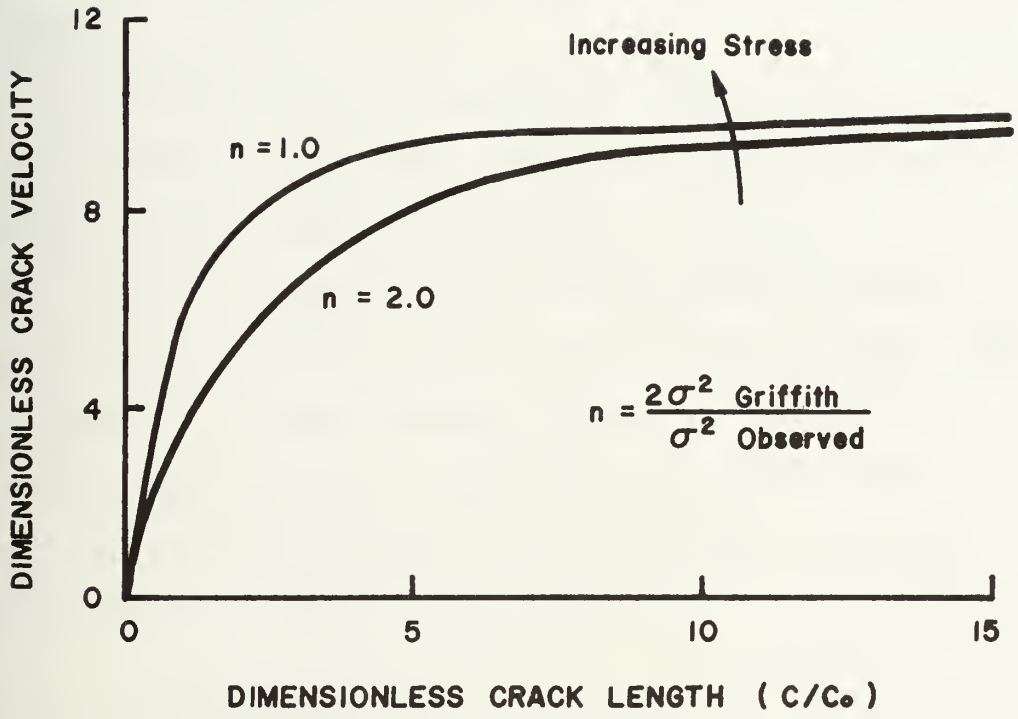

Figure 4.6--Crack propagation velocity versus crack length (89).

It has been demonstrated from experiments on glass (97, 98) that the terminal velocity of all cracks is the same, unless the crack slows down or stops as a result of branching. The crack propagation velocity, however, is not uniform across the specimen width (99). The velocity of each individual fracture is influenced by such factors as the degree of load relaxation during the dynamic phase of the process.

In a specimen subject to bending, the velocity history is somewhat different. The crack initiates and propagates through a zone of transition, but as the terminal velocity is approached, the specimen's neutral axis cannot shift fast enough as the crack approaches. The resulting velocity versus depth is shown in Figure 4.7: the velocity decreases with depth under flexure. The decrease results from the fact that the crack has passed beyond the original neutral axis location.

4.4 Basic fracture mechanics

As most recent trends in crack propagation analysis have centered around the local stress and strain relations at the crack tip via what is known as fracture mechanics, a brief review of this concept is considered essential. This type of analysis is based on the belief that crack growth will occur when certain critical conditions are reached at the crack tip (100). Essentially, the

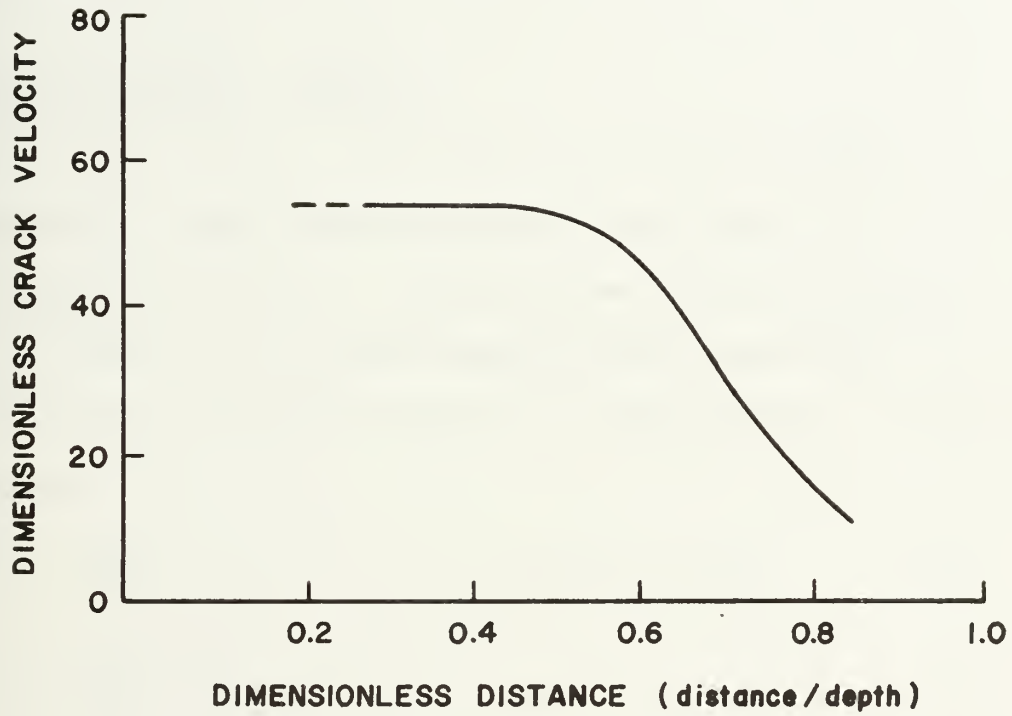

Figure 4.7--Fracture velocity versus depth for a glass bar in bending (100).

application of fracture mechanics depends on knowing the material behavior under various crack loading conditions from experimental results. Then, comparing this behavior to the applied conditions at the crack tip of any crack a determination as to whether the critical conditions are reached can be made.

4.4.1 Brittle fracture (linear elastic fracture mechanics)

As previously related, Griffith's original work (87) for fracture of an ideal brittle material was based on an energy balance criterion. This work was later extended by Irwin (101) and the Griffith equations were rewritten in terms of a crack extension force, g, (required for crack movement) as:

$$g = \frac{\pi c \sigma^2}{E} \qquad \text{(plane stress)} \qquad (4.6)$$

$$g = \frac{\pi c \sigma^2}{E} (1 - \nu^2) \qquad \text{(plane strain)} \qquad (4.7)$$

where

c = the half crack length

σ = the applied stress

ν = Poisson's ratio

This crack extension force must be greater than a critical crack extension force for crack propagation.

Griffith introduced cracks of various lengths and by recording the loads at failure he was able to determine that the product of the original crack length and the load

at failure was essentially a constant for a given material. Irwin (101) then related the crack extension force to a stress intensity factor, K, which took the place of Griffith's experimental constant in the stress equations describing the stress field around the crack tip. Physically, K may be regarded as the intensity of the load transmittal through the crack tip region resulting from the introduction of the crack, and it therefore represents the magnitude of the stress field in this region. Irwin's relations were given as (101):

$$g = \frac{K^2}{E} \qquad \text{(plane stress)} \qquad (4.8)$$

$$g = \frac{K^2}{E}(1 - \nu^2) \qquad \text{(plane strain)} \qquad (4.9)$$

The symbol K_c is normally used to represent $g\sqrt{\pi c}$ (the critical value) and it is called the fracture toughness of the material. For a given material, all combinations of crack geometry and loading at incipient fracture yeild the same value of K_c making it a constant for that material. The fracture toughness, or critical stress intensity factor as it is sometimes called, K_c, can be a function of temperature or loading rate (99), and it represents the critical value of the stress field in the immediate vicinity of a sharp crack tip as illustrated in Figure 4.8.

The general form of the equation representing the crack tip stress field in terms of K, when the load or the

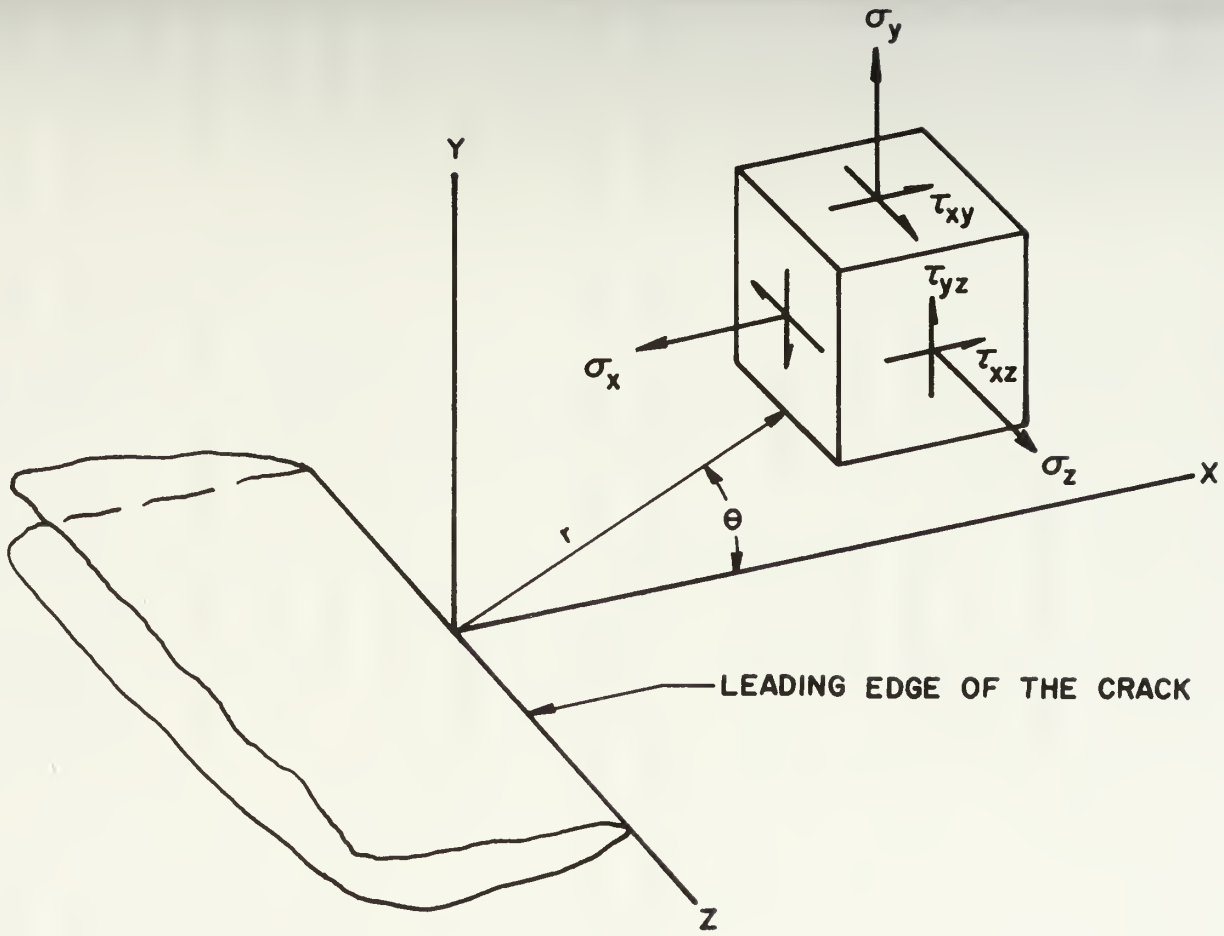

Figure 4.8--Coordinates measured from the leading edge of the crack and the stress components in the crack tip stress field (103).

crack size is below the threshold of instability is (101):

$$\sigma_{i,k} = \frac{K_n}{\sqrt{2\pi r}} F^n_{i,k}(\theta) \qquad (4.10)$$

where

i,k = x,y,z

n = failure mode (I,II,III)

$F^n_{i,k}$ = a function of the angle

K_n = constant, independent of r

σ = stress in directions i,k

r = distance from crack tip

θ = angle

The fracture modes are denoted as (I) wedge opening, (II) forward shear, and (III) parallel shear as depicted in Figure 4.9.

The factor K is analytically determined, and it varies as a function of the crack configuration and the method of load application. However, once the critical value of K for a material is determined, for a given combination of crack configuration and loading, it remains essentially unchanged for all other combinations of crack and loading conditions. Hence, as previously pointed out, the critical value of K is referred to as a material constant. An excellent compilation of the analysis of cracks and the determination of K for numerous cases and geometries can be found in Ref. 103.

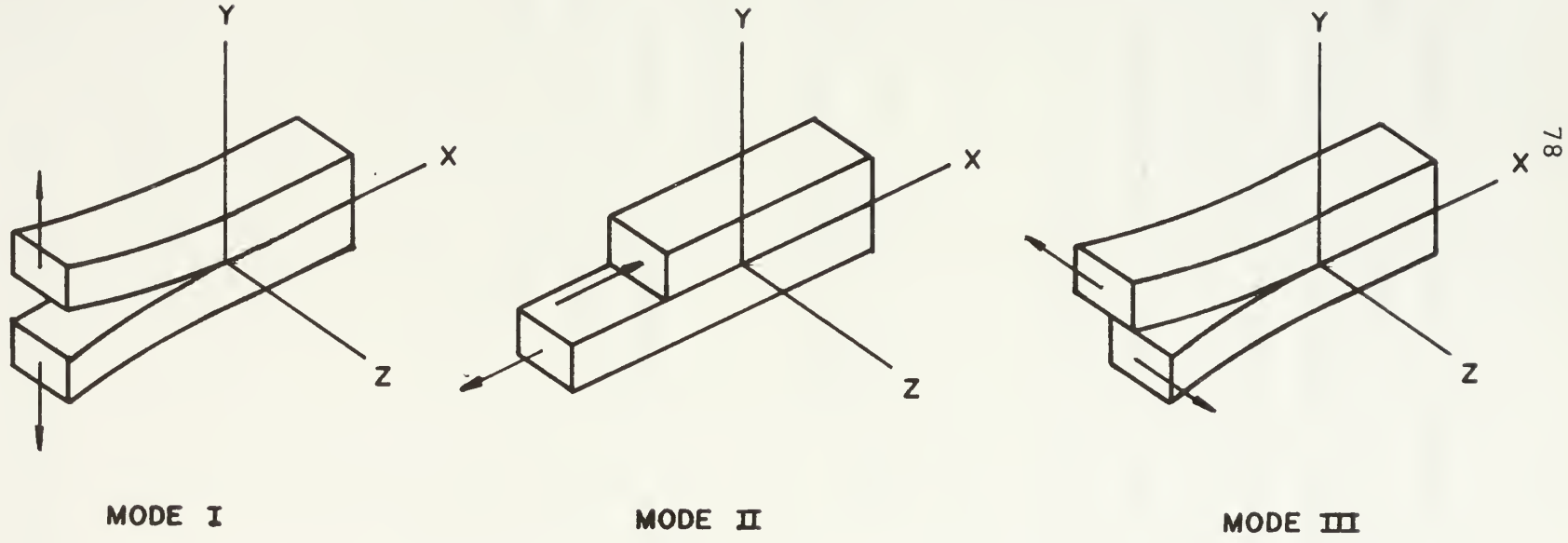

Figure 4.9--The basic modes of crack surface displacement (103).

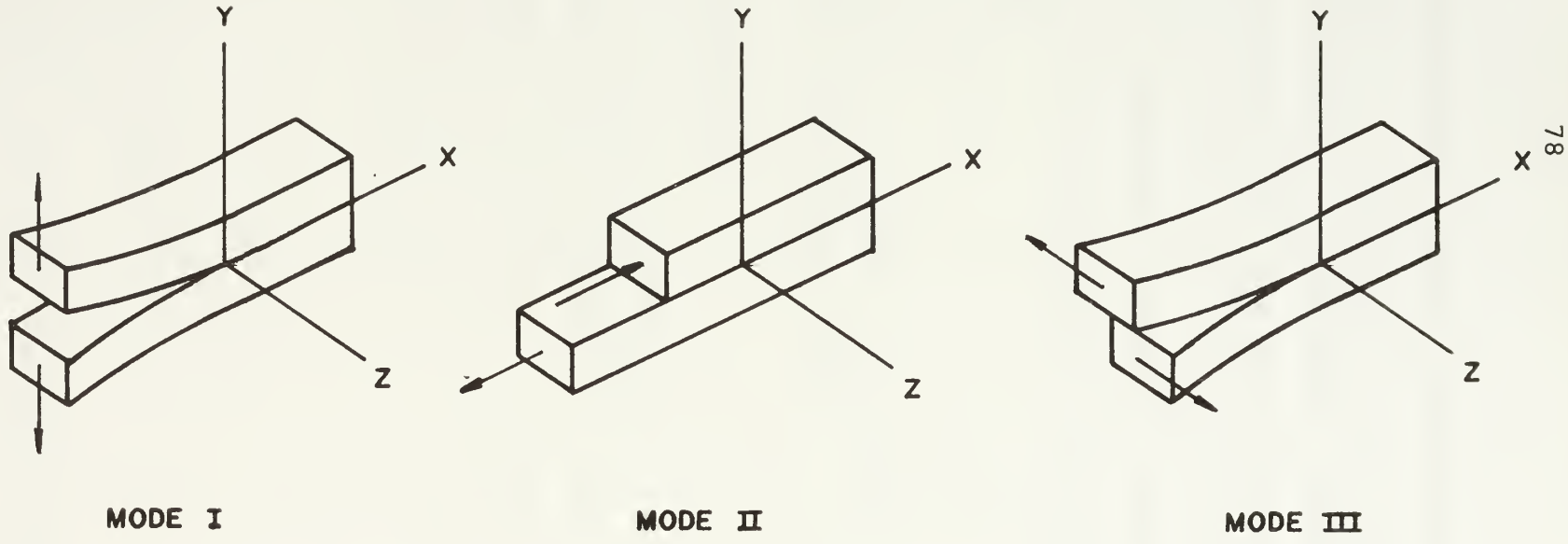

Figure 4.9--The basic modes of crack surface displacement (103).

When analyzing stresses and fracture properties under real loading conditions, it is necessary to take into account all types of loadings. For different loadings resulting in the same failure mode (stress intensities caused by pressure, temperature, etc.) the total stress intensity factor for the system is the sum of the single stress intensities of the same mode (102). As an example, for mode I this implies:

$$K_I = K_I(1) + K_I(2) + \ldots$$

This procedure and the above formulas are strictly applicable only in the linear elastic field.

4.4.2 Elastic-plastic fracture (plasticity effects)

In an effort to determine the influence of yielding at the crack tip, other models and methods of attack were developed. The procedures representative of such an analysis are given by Wells (104). Here, the plastic zone around the crack tip is described by:

$$r_y = \frac{K^2}{2\pi\sigma_y^2} \tag{4.11}$$

where

r_y = plastic zone size

σ_y = yield stress

Then from the displacement equations, the crack opening displacement is found to be:

$$\delta = \frac{K^2}{E\sigma_y} = \frac{\pi\sigma^2 c}{E\sigma_y} \tag{4.12}$$

where

δ = crack opening displacement

In this case, a critical crack opening displacement represents fracture.

In a more general form, the plastic zone is given as (103):

$$r_y = \alpha \left(\frac{K}{\sigma_y}\right)^2 \tag{4.13}$$

where

$$\alpha = \begin{cases} \frac{1}{2\pi} & \text{(plane stress)} \\ \frac{1}{6\pi} & \text{(plane strain)} \end{cases}$$

The plasticity at the crack tip causes some redistribution of the stresses to maintain equilibrium. Thus, the full width of the plastic zone is taken as twice the above result. These results are somewhat in error, as they neglect work hardening, large strains, or other influences. In some cases r_y is added to the crack length to obtain an "effective crack size" followed by conventional linear elastic analysis. This method is not extremely accurate, but has proven useful when trends are desired.

However, it has been pointed out (103) that small amounts of plasticity or other non-linearities at the crack tip do not seriously further disturb the load

redistribution around the crack tip, hence the relevance of the K values remains. Therefore, where small amounts of non-linearity are deeply embedded within the stress field, they do not have a significant impact, and a combination of K_I, K_{II} and K_{III} represents a unique stress field at the crack tip for small-scale yielding. Thus, if yielding is limited to a small enough scale, the linear-elastic theory is both reasonable and adequate.

When plasticity effects are present to the extent such that general yielding is in evidence, the elastic-plastic analysis may not be completely valid. Several basic approaches in the area of non-plane strain behavior are being developed. One such criterion being studied at Westinghouse (104), originally developed by Rice (106), is based on an energy line integral, J, defined as:

$$J = \int_r wdy - T \frac{\partial u}{\partial x} ds \qquad (4.14)$$

where

T = traction vector

u = displacement vector

w = strain energy density

The application of J is similar to that of K in the linear-elastic analysis. As yet, this method has not been developed to the point where it can be generally applied, and presently elastic-plastic analysis methods are used as approximations in many cases where extensive plasticity is found to exist.

4.5 Fracture of ceramics

Ceramics, compared to other materials, are extremely brittle. They are thus prone to catastrophic failure, particularly under conditions of shock. As a result, ceramics have come under separate study. One such study is that of Ref. 107, which provides a unified approach in determining the fracture of ceramics.

As noted before, the application of the Griffith criterion yields values of the fracture stress too small when plasticity has an effect. Since for most materials, the high shear stresses near the crack tip exceed the plastic flow stress, allowing some stress relief, the applied stress must be increased for propagation to continue. To account for these plasticity effects, the alternative energy criterion has been presented, as opposed to the K (stress intensity) type of approach of fracture mechanics. According to this approach (107-109), the effects of plastic flow can be incorporated in a surface energy for fracture initiation, γ_i, so that

$$\sigma_f = \left(\frac{2E\gamma_i}{\pi C}\right)^{1/2} \qquad \text{(plane stress conditions)} \quad (4.15)$$

In theoretical evaluations, allowances are made for all energy losses due to various forms of work (plastic flow, cleavage steps, crack branching, etc.) but crack blunting is not accounted for. Therefore, it is usually not a sufficient condition for crack propagation. It would be

sufficient, however, if an empirical γ_i which accounted for crack blunting is used. In ceramics, $\sigma_y >> \sigma_f$ (except at high temperatures) and the effects of crack blunting are likely to be small so that the measured γ_i may approach the theoretical value (110).

If the size of inherent flaws can be determined, the above equation can be used to calculate the stress to extend these flaws. If the values obtained are close to the observed fracture stress, it is likely that the fracture is a direct result of extending inherent flaws (brittle fracture). If this is not the case, fracture is most likely initiated by plastic flow. Here, the fracture stress is related to the stress to nucleate and/or propagate fresh flaws. Then the fracture control mechanism requires an analysis of the plastic flow stress. The former case, however, normally holds true for ceramic materials.

The alternative surface energy criterion is related to the K (stress intensity) concept in that at the point of catastrophic crack propagation the following holds: $K^2 = K_c^2 = 2E\gamma_i$. Utilization of γ_i in the case of ceramics is preferred in some cases because it can be directly related to the energy absorbing process occurring during crack propagation (110). In metals where blunting by plastic flow takes place, K_c is more useful.

Theoretical relationships do not exist between γ_i and grain size, porosity, temperature, or purity, and there is not enough data to obtain empirical relationships. Therefore, the utilization of this method is, at present, somewhat limited. Variation of γ_i with crack length has been evaluated for a number of materials (110, 111). At low to moderate temperatures γ_i is found to be independent of crack length for edge cracks greater than a grain diameter in length.

In estimating the theoretical fracture stress for brittle failure via extension of internal flaws, the relevant flaw size must be known. This flaw size, in ceramics, is related to the microstructure of the material through pores, voids, grains, etc. The largest flaw is controlling, if it is atomically sharp. When pores are larger than grains, they can act as flaws, themselves. In most cases, the inherent flaw size can be related to either pore or grain sizes.

Normally, the stress to extend a small flaw through a grain is much lower than the fracture stress. Therefore, in these cases, the inherent flaw existing in a ceramic can be approximated by the pore size plus the grain size (111). Then with the value of γ_i known, the fracture stress can be evaluated, or vice versa, through Equation 4.14.

CHAPTER FIVE

FRACTURE ANALYSIS OF THE UO_2-SODIUM SYSTEM

5.1 Introduction

In order to determine whether or not the solidifying shell of UO_2 will fracture, various methods of making such a calculation were investigated. In all cases, the analysis was necessarily quasi-static. After evaluating fracture stress, energy balance, and fracture mechanics type methods, an approach based on fracture mechanics was determined to be the most appropriate. This method, based on the knowledge of the stress intensity factor, K_I, and the fracture toughness, K_{IC}, will then allow determination of whether the shell will fracture from a given flaw, under the influence of the prevailing stress field. A description of the foundation of this type of fracture analysis was given in the previous chapter. In this case, due to the high strain rates and the brittle nature of the UO_2, the linear-elastic approach was considered adequate for first-order calculations.

In order to obtain immediate and inexpensive evaluations of the possibility of brittle fracture, the application of analytical methods is most desirable. These analytic methods can be checked by means of finite

element computer techniques, if the application warrents. The result is that there are three basic ways of attacking the problem; the first two being analytic and the third the finite element method. First, a one-shot approach based on existing analytic models assumes that once K_I exceeds K_{IC} catastrophic crack propagation takes place. The second, also analytic, is based on varying the crack length across the shell, ensuring that K_I exceeds K_{IC} all the way across (a progressive method). The third method is the same as the second, but it uses finite element techniques to evaluate K_I rather than existing analytic models. The first method was selected for the initial investigation.

5.2 Analytical evaluation of K_I

As shown previously, it is possible to compute the stresses caused by the internal pressure and by the temperature distribution. The components of these stresses perpendicular to the plane of the crack are needed for the computation of the stress intensity factors K_{It} (resulting from the thermal gradient) and K_{Ip} (resulting from the induced pressure). Brittle fracture will then occur when the sum of these stress intensity factors exceeds the fracture toughness, K_{IC}.

The thermal stress distribution across the shell can, for a given time step, be linearly approximated as shown in Figure 5.1. The linearized thermal stress distribution

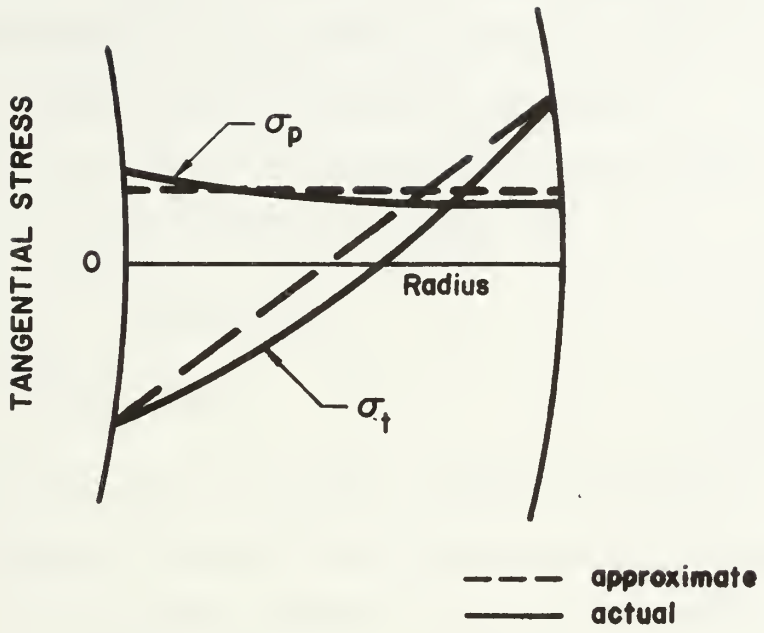

Figure 5.1--Linear approximation of thermal and pressure stress components.

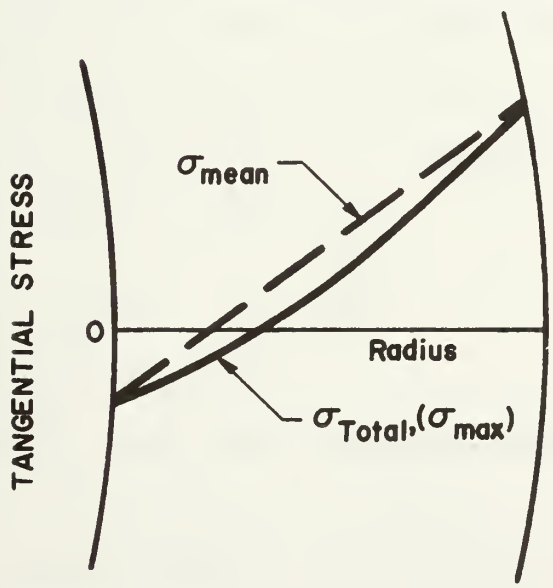

Figure 5.2--Linear approximation of total stress.

can then be combined with the pressure stress distribution (approximately constant) at the same time step. The combined stress distribution can then be completely described by stress values at two radial positions since the distribution is assumed linear (Figure 5.2).

$$\sigma_{max} = \sigma_p + \sigma_{thermal\ max} \tag{5.1}$$

$$\sigma_{mean} = \frac{\sigma_{max} + \sigma_{min}}{2} \tag{5.2}$$

In order to calculate the stress intensity factors in terms of the applied stresses, an analytical expression is then required. The linear thermal stress distribution is similar to that resulting from an applied moment. Thus, the two stress fields can be represented as the superposition of a uniform stress upon that caused by a bending moment. An analytic expression for just such a case has been developed (111) to allow for the solution of an arbitrary linear stress field. The total K_I is defined as (with a representing crack depth in this case)

$$K_{It} = \sqrt{\pi a}\left[\sigma_{max} f\left(\frac{a}{w}\right) + \sigma_{mean} g\left(\frac{a}{w}\right)\right] \tag{5.3}$$

where $g(a/w) = k(a/w) - f(a/w)$.

This expression, along with the appropriate correction factors, is summarized in Figure 5.3.

An alternate method based on the analytical models given in Ref. (103) can also be utilized. In this case the values of K_{Ip} and K_{It} are calculated separately and

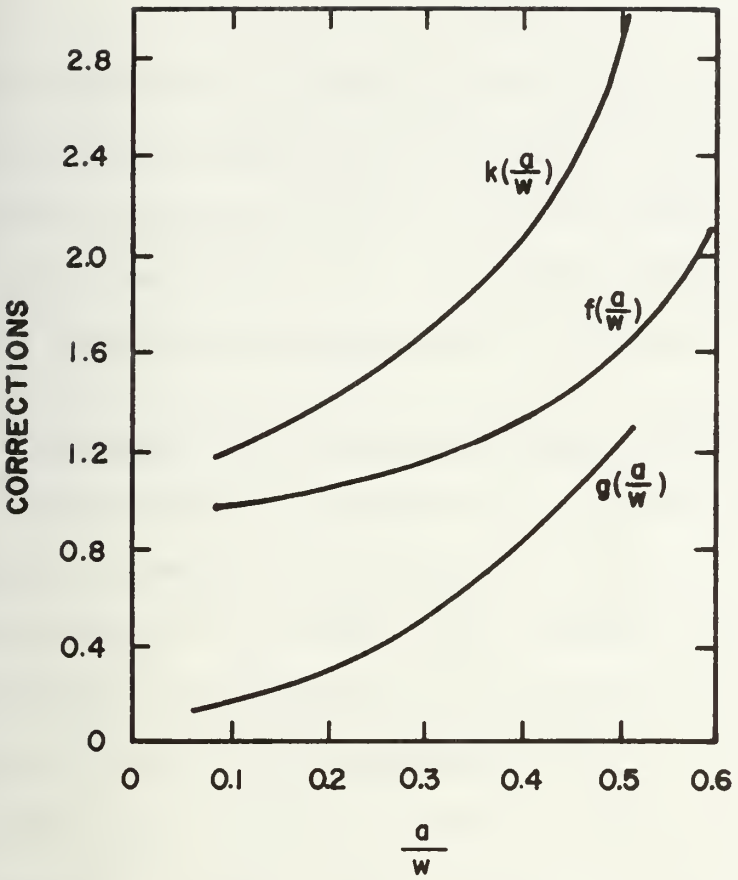

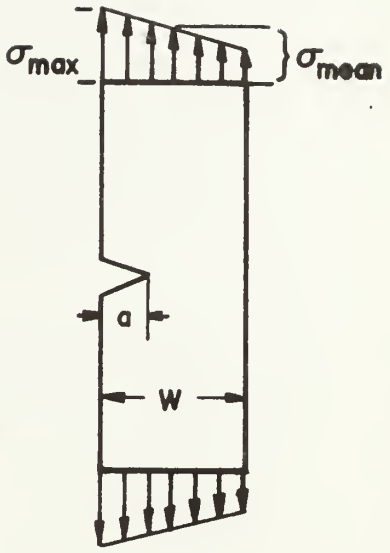

$$K_I = (\pi a)^{1/2}\left[\sigma_{max}\, f(a/w) + \sigma_{mean}\, g(a/w)\right]$$

a/w	k(a/w)	f(a/w)	g(a/w) = k(a/w) − f(a/w)
0.05	1.15	0.981	0.169
0.10	1.20	1.024	0.176
0.20	1.37	1.058	0.312
0.30	1.68	1.161	0.519
0.40	2.14	1.324	0.816
0.50	2.86	1.625	1.235
0.60		2.102	

Figure 5.3--Stress intensity factors for a single edge-notched strip in combined stretching and bending (102).

added together to yield the total K_I. Again, the two stress fields (pressure and thermal) are modeled as a uniform stress field and a linear stress field equivalent to that resulting from a comparable moment, respectively. These models are illustrated in Figures 5.4 and 5.5.

5.3 Comparative evaluation of the modeling techniques

In an effort to compare the two alternative analytical models, a sample calculation was carried out to evaluate the predicted K_I values. The stress field values in the solidified shell used in the comparison were those for a time of .044 sec as reported in Ref. (78) (see Figure 5.6), as this time is close to that at which the maximum tangential stress level is reported to occur. The linearized approximation used in the analysis is also shown in Figure 5.6. Further, an approximate flaw size of 75×10^{-4} cm was used, representing a grain size of 25 μm and a pore size of 50 μm as obtained from reference (111). This value is an estimation based on the fact that in polycrystalline UO_2 the stress to propagate a pore to fracture is accurately predicted by taking a flaw size equal to the pore size plus the grain size (111). The comparative calculations for each model can be seen in Figure 5.7. As shown, the difference in the results is within the accuracy of the calculations. Therefore, the first method was arbitrarily selected for use in succeeding evaluations of K_I values.

STRESS INTENSITY FACTOR: $K_I = \sigma\sqrt{\pi a}\, F(\frac{a}{b})$

NUMERICAL VALUES OF F(a/b):

The curve in the following figure was drawn based the results having better than 0.5 % accuracy.

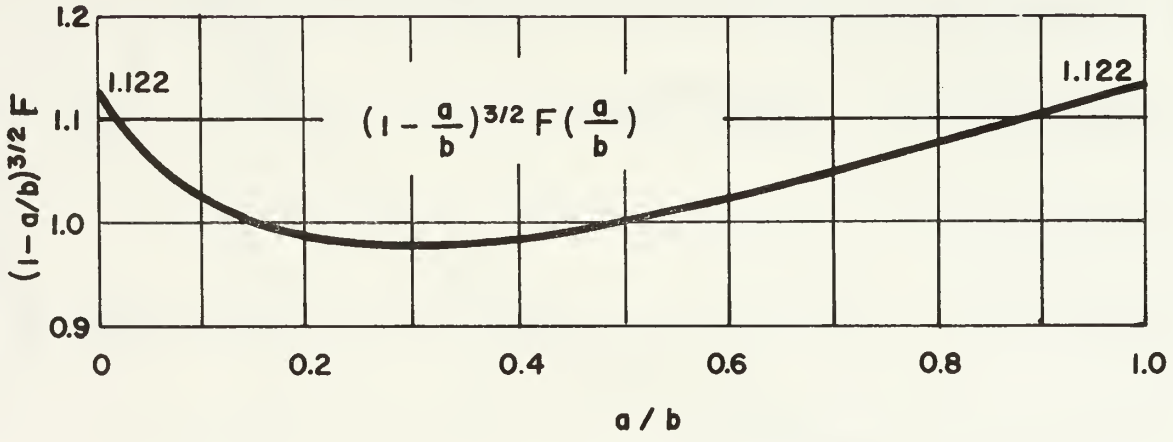

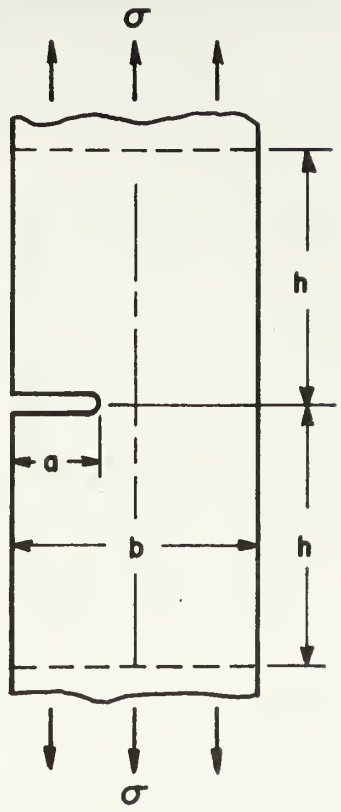

Figure 5.4--Stress intensity factor for a single edge-notched strip under uniform extension (103).

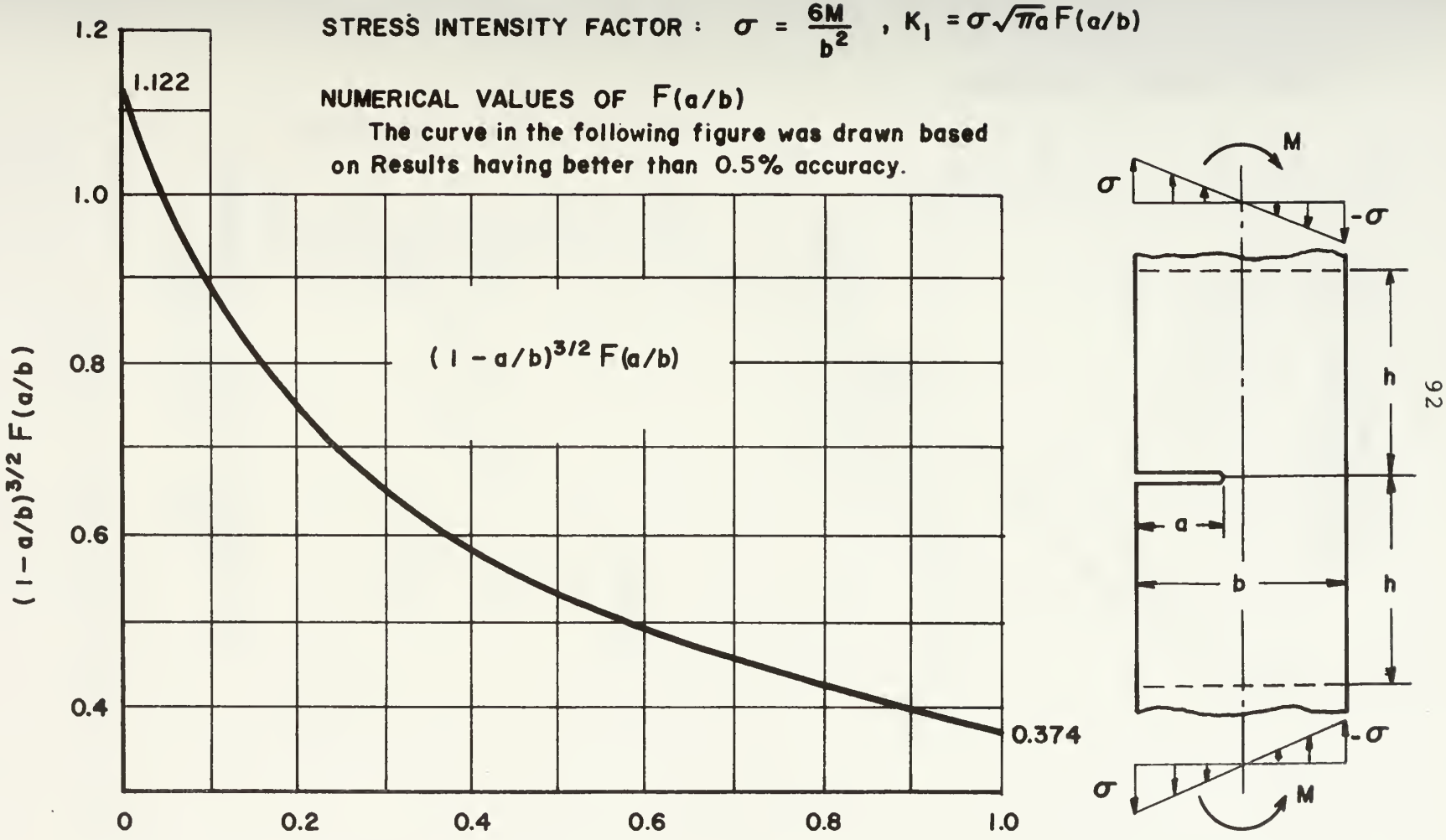

Figure 5.5---Stress intensity factor for a single edge-notched strip in bending (103).

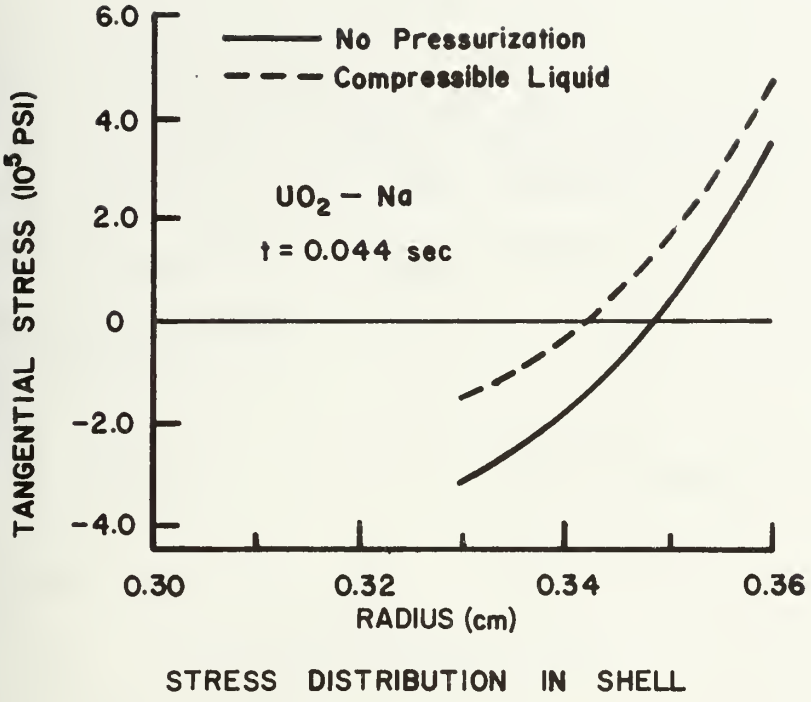

STRESS DISTRIBUTION IN SHELL

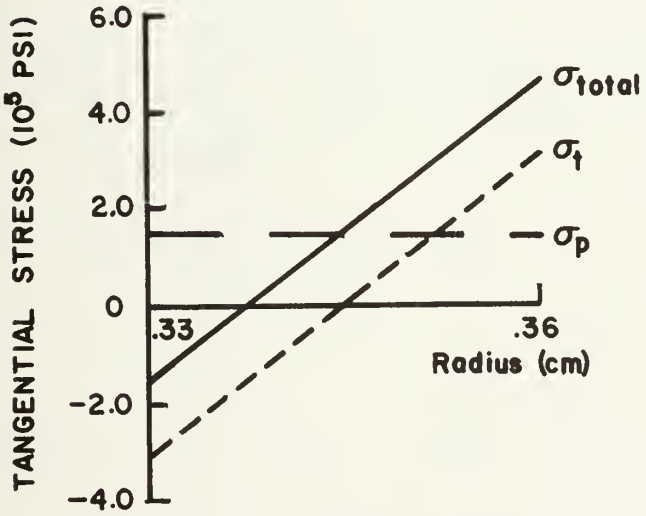

LINEARIZED STRESS APPROXIMATION
(COMPRESSIBLE LIQUID)

Figure 5.6--Actual and linearized approximation for the stress distribution in the shell.

Method 1

$\sigma_{max} = 4.7 \times 10^5$ psi $\quad \sigma_{mean} = 1.55 \times 10^5$ psi

$a/w = .167 \rightarrow g(a/w) \cong .40$ and $f(a/w) \cong 1.1$

$K_I = (\pi a)^{1/2}[\sigma_{max} \cdot f(a/w) + \sigma_{mean} \cdot g(a/w)]$

$K_I = \underline{5.58 \times 10^4 \text{ psi}\sqrt{\text{in}}}$

Method 2

$\sigma_P \cong 1.5 \times 10^5$ psi $\quad \sigma_t \cong 3.2 \times 10^5$ psi (max)

Pressure

$K_{IP} = \sigma_P \sqrt{\pi a}\, F(a/b)$

$(a/b) = .167 \rightarrow (1 - a/b)^{3/2} F(a/b) = .49$

$F(a/b) = 1.509$

$K_{IP} = 2.18 \times 10^4 \text{ psi}\sqrt{\text{in}}$

Thermal

$K_{It} = \sigma_p \sqrt{\pi a}\, F(a/b) \quad (a/b) = .167$

$(1 - a/b)^{3/2} F(a/b) \cong .8 \rightarrow F(a/b) = 1.062$

$K_{It} = 3.273 \times 10^4 \text{ psi}\sqrt{\text{in}}$

$\therefore K_I = K_{IP} + K_{It} = \underline{5.45 \times 10^4 \text{ psi}\sqrt{\text{in}}}$

Figure 5.7--Analytic evaluation of stress intensity factor, K_I, via two alternate methods.

5.4 Determination of K_{IC}

Through the analysis of extensive amounts of data on the deformation and fracture of oxide fuels (113, 114) the brittle fracture stress of UO_2 has come to be represented as

$$\sigma_f = 16{,}029 + 3.333T \qquad (5.4)$$

where T is in °C and σ_f is in psi. The input data behind equation (5.4) over the range of interest was established via three-point bending tests of 24 x 6 x 5 mm UO_2 specimens (111). Note that UO_2 specimens were prepared by powder pressing and sintering methods and may not be characteristic of UO_2 shells obtained from solidification of molten, irradiated UO_2. However, for this material it is expected that the grain size and porosity characteristics are similar, and that the resulting fracture characteristics will not vary significantly from the ones used here. It is then possible, utilizing a nominal flaw size of 75 μm, to determine the appropriate values of K_{IC} with respect to temperature. The simplest "best" estimate of K_{IC} is obtained through the use of the analytical model illustrated in Figure 5.8. Application of this model, in conjunction with the fracture stress found from equation (5.4), yields the plot of K_{IC} versus temperature as shown in Figure 5.9. To engage in first order fracture calculations, a value corresponding to a mid-range temperature is selected. In

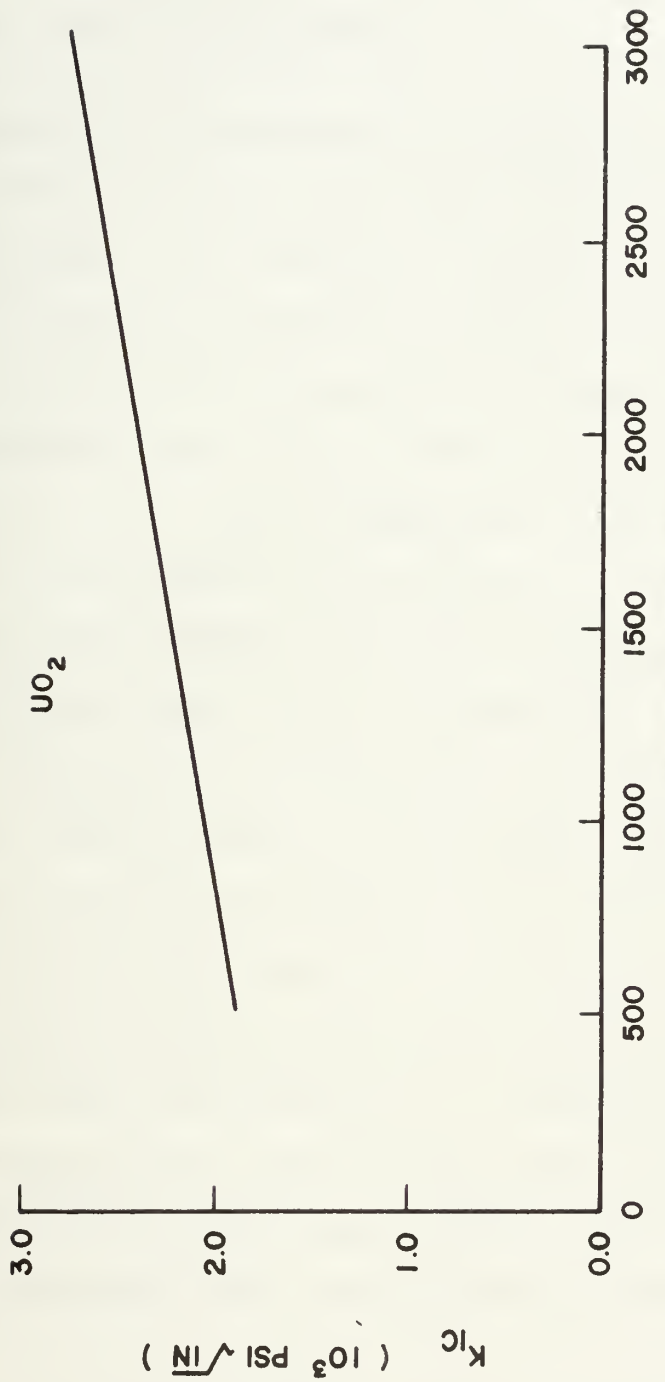

Figure 5.9--K_{IC} as a function of temperature for UO_2.

this case a value of $K_{IC} = 2.407 \times 10^3$ psi$\sqrt{in}$ (at approximately 2000°C) was chosen.

5.5 Evaluation of the stresses in the solidified shell

In an effort to obtain the stress states and their appropriate values for a variety of times, the fixed surface temperature condition, using mean property values (77) was employed for the conditions reported in Chapter 3, i.e., UO_2 at its melting point, Na at 200°C and an interface temperature of 945°C. These temperature conditions were maintained for the entire UO_2/Na analysis in this chapter. Based on Adams (82) solution for the temperature profile and solidification front velocity (equations 11 and 12 of Chapter 3), equations 1-3 of Chapter 3 were used to evaluate the induced pressure and stresses. The induced pressure, in this case, is based on the attempted thermal contraction of the solid shell with the limited compressibility of the molten UO_2 taken into account. The density change upon solidification is neglected. The resulting values of the solidification front position with time, induced pressure with time and the external tangential stress with time can be seen in Figures 5.10-5.12.

The values obtained via the above method differ somewhat from those reported in Ref. 77. In the present case, the overall stress levels are found to be higher

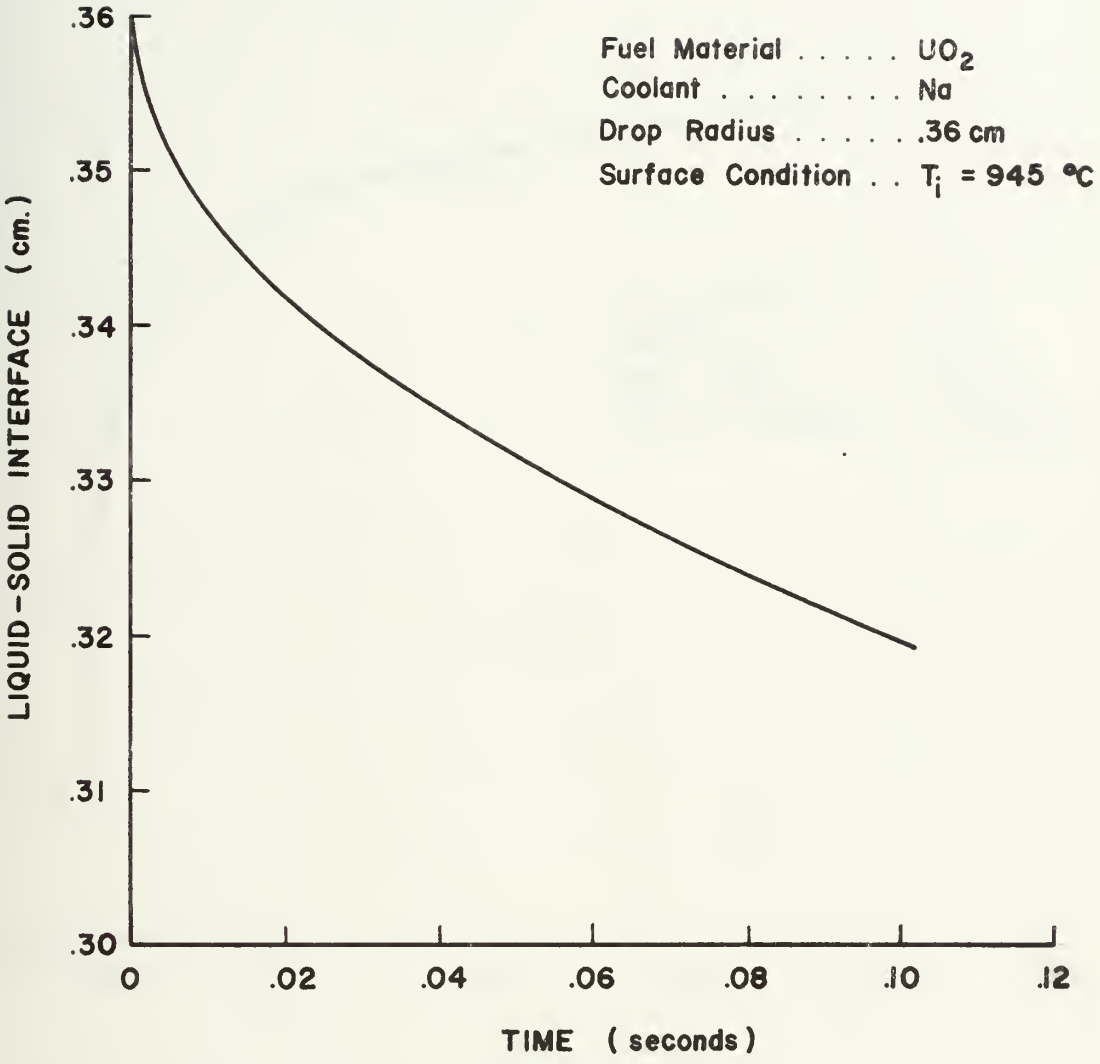

Figure 5.10--Liquid-solid interface position with fixed surface temperature.

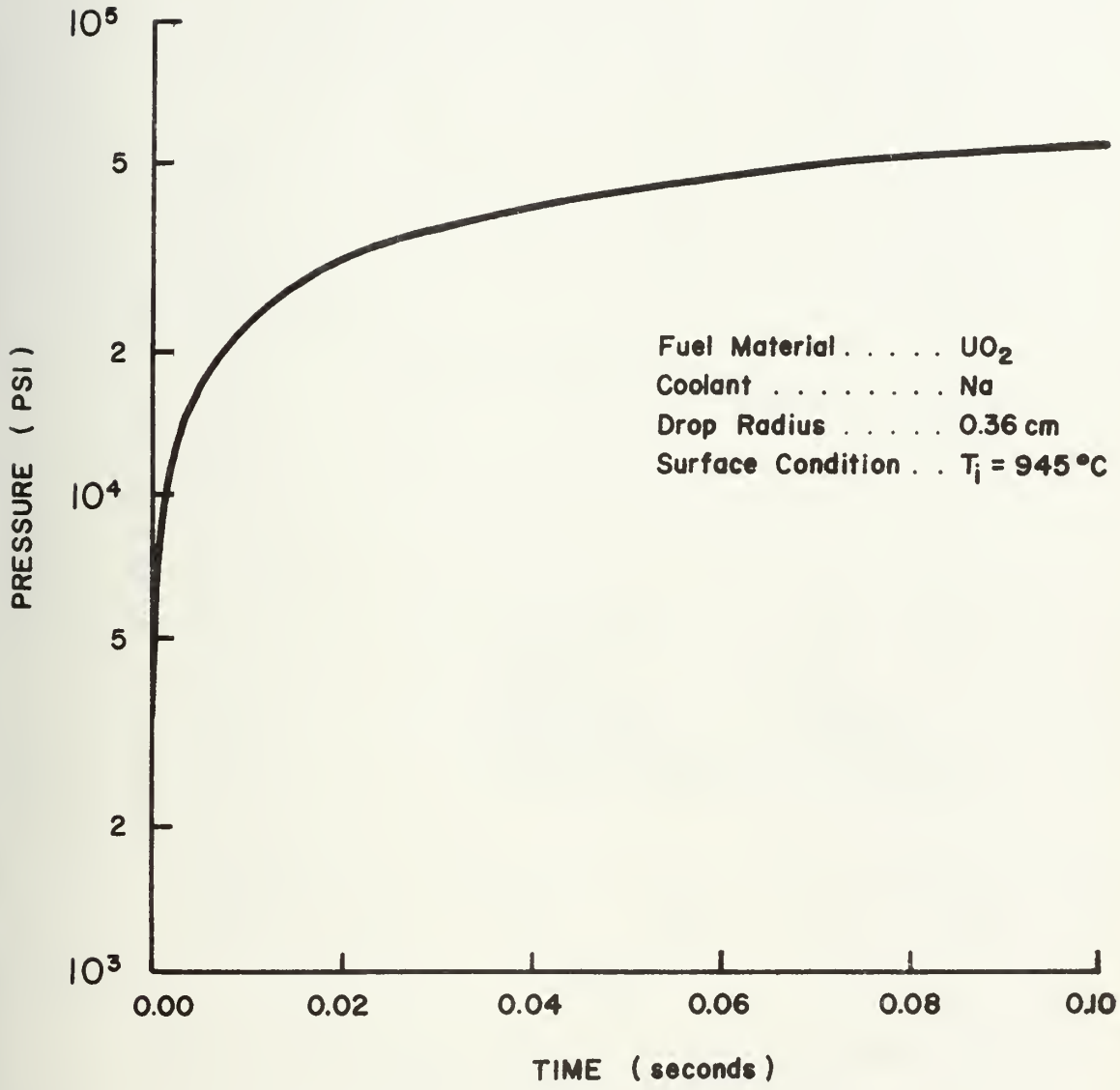

Figure 5.11--Pressurization of the molten core.

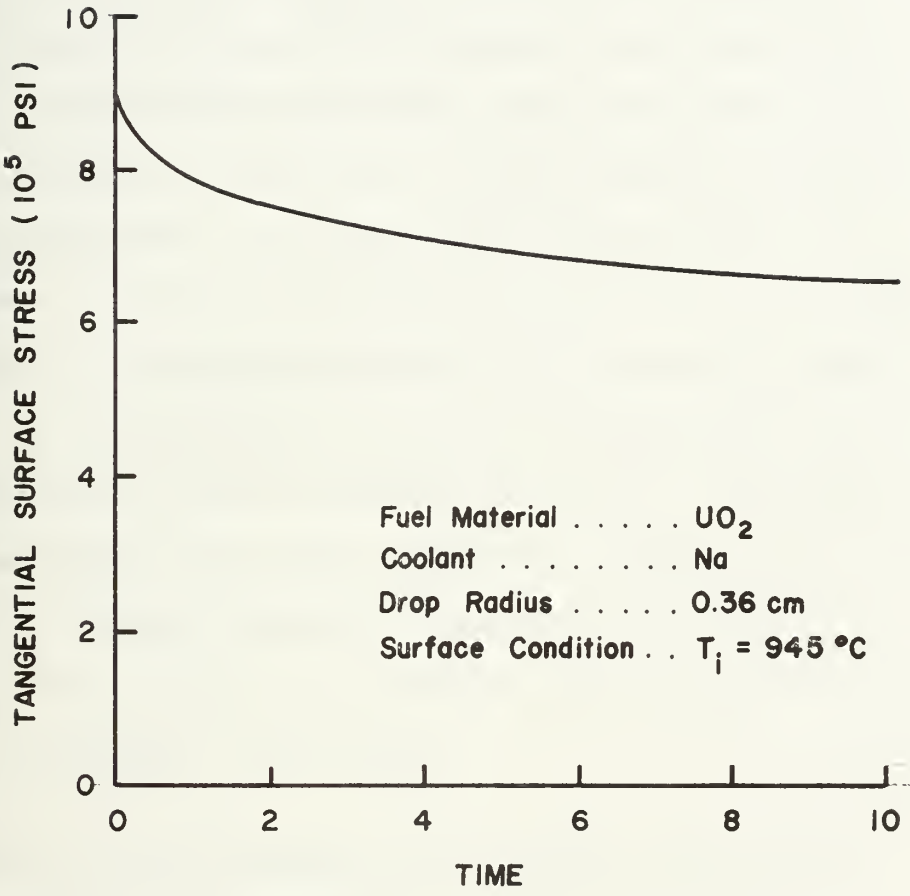

Figure 5.12--Total tangential surface stress with fixed surface temperature.

(although of the same order of magnitude) and the peaking phenomena experienced by the external tangential stress in Ref. 77 is nothing more than a minor perturbation here. This latter result came from the fact that the maximum tangential pressure stress occurs almost instaneously as, initially, the pressure rises faster than the shell thickness increases. The values of the thermal stresses developed in the shell are higher than those of Ref. 77 for all times, including the initial value at $t = 0^+$. This initial value is directly related to the values of α and E used in the stress equations and the values used here are consistent with those reported in Ref. 77. Thus, it is not clear wherein lies the difference. Hence, the values of the induced stresses obtained in the present study are taken as those to be used in the fracture analysis, to maintain consistency.

5.6 Variation of the surface heat transfer coefficient

In an effort to determine the effect of various amounts of entrapped fission gas surrounding the UO_2 particles in the sodium coolant on the generated stresses, an analysis based on varying the surface heat transfer coefficient was also carried out. Taking constant, mean values of the thermophysical properties, the governing equation and conditions are given by equations 4-8 of Chapter 3. In conducting the analysis, the steady-state

solution of London and Seban (80) was used for the heat transfer and solidification calculations in a manner similar to that used in Ref. 76. This method was considered adequate as only a comparative evaluation over relatively short times was desired. The same assumptions as enumerated earlier with respect to this method are applicable, and the geometry of the model is still that of a molten UO_2 sphere suddenly immersed in an infinite sodium pool (Figure 3.1).

The steady-state approximation, strictly valid when the latent heat of fusion is significantly greater than the internal energy change in the shell, maintains the shape of the temperature profile as solidification proceeds. The governing equations for this case, replacing 4-8 of Chapter 3, become:

$$\frac{d^2[rT(r)]}{dr^2} = 0 \qquad \text{for } a < r < R \qquad (5.5)$$

where $T(r) = T'(r) - T_c$ subject to the boundary conditions

$$-k \left.\frac{dT(r)}{dr}\right|_{r=R} = hT(R) \qquad \text{at } r = R \qquad (5.6)$$

$$T(a) = T_m = T_m' - T_c \qquad \text{at } r = a(t) \qquad (5.7)$$

$$k \left.\frac{dT(r)}{dr}\right|_{r-a} = \rho L \frac{d(a)}{dt} \qquad \text{at } r = a(t) \qquad (5.8)$$

and $a(0) = R$.

The solution of the above is

$$\frac{T(r,t) - T_c}{T_m - T_c} = \frac{\left(\frac{a}{r}\right)\left[1 + \left(\frac{r}{R}\right)\left(\frac{1}{Bi} - 1\right)\right]}{\left(\frac{r}{R}\right)\left[1 + \left(\frac{a}{R}\right)\left(\frac{1}{Bi} - 1\right)\right]} \qquad (5.9)$$

in nondimensional form. Equation (17) yields the temperature profile within the solid shell. Substitution of equation (17) into equation (16) results as

$$d\bar{r} = \frac{-\bar{t}}{\bar{r}\left[\bar{r}\left(\frac{1}{Bi} - 1\right) + 1\right]} \qquad (5.10)$$

where

$$\bar{r} = a/R$$

and

$$\bar{t} = kT_m t/LR^2$$

Then, integrating subject to the initial condition

$$\bar{r} = (a/R) = 1.0 \qquad \text{at } \bar{t} = 0$$

yields the equation for the solidification front position

$$\frac{\left(\frac{1}{Bi} - 1\right)(\bar{r}^3 - 1)}{3} + \frac{(\bar{r}^2 - 1)}{2} = -\bar{t} \qquad (5.11)$$

A plot of $\bar{r}$ vs. $\bar{t}$ for various values of h demonstrates the relative sensitivity of the solidification rate to the coefficient of heat transfer, and thus, the amount of surrounding fission gases (Figure 5.13). The constant surface temperature results are included as well for comparative purposes. It can be seen from Figure 5.13 that as the heat transfer coefficient is increased, the rate of solidification increases. Further, it is noted that, as concluded by Cronenberg et al. (77), the fixed

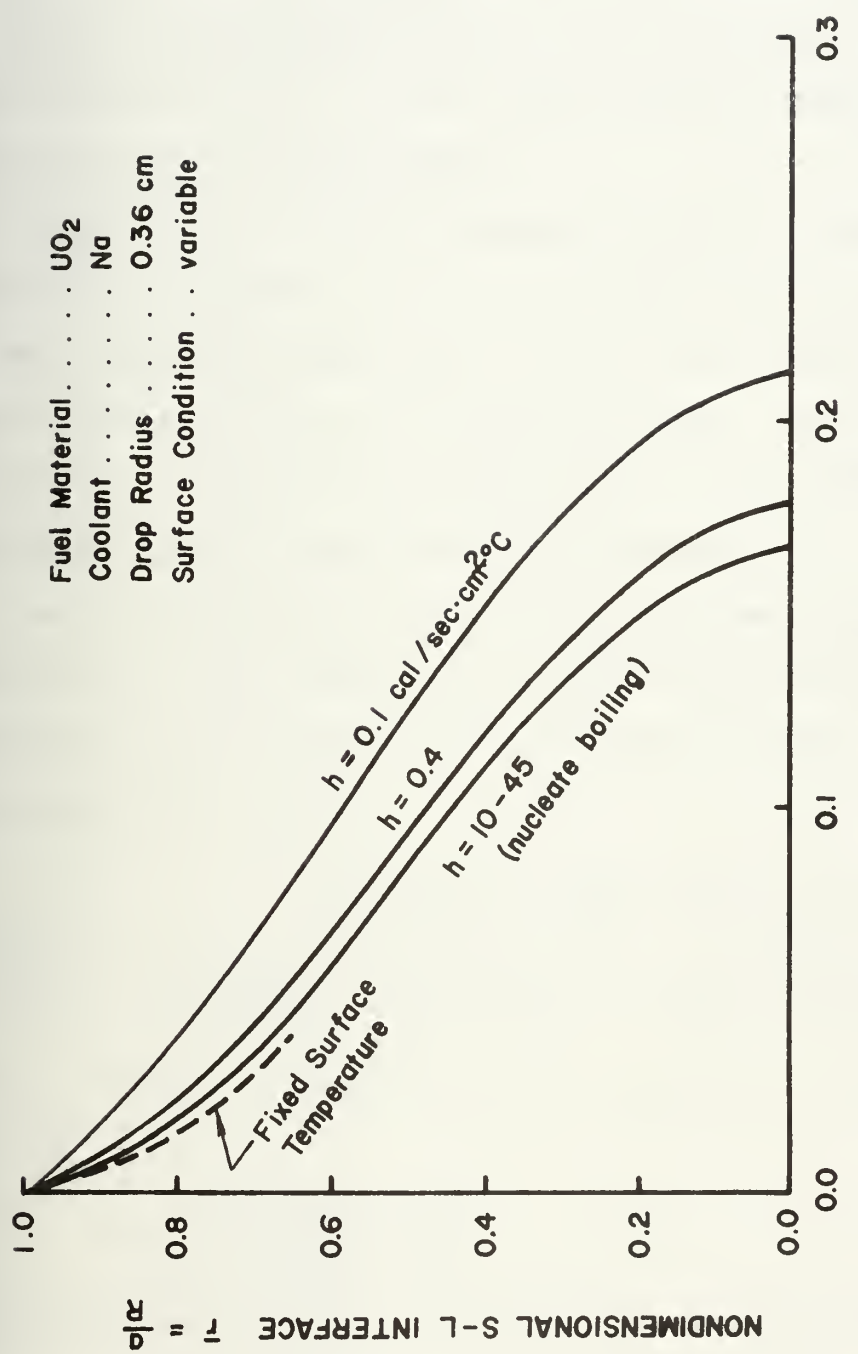

Figure 5.13--Effect of surface heat transfer coefficient on nondimensional S-L interface.

surface temperature condition results in values close to (although slightly faster than) those corresponding to a nucleate boiling coefficient (41.34 Cal/sec cm^2°C $\cong$ 10,000 Btu/hr ft^2°F), for the same coolant temperature with UO_2 at its melting point.

The second part of the comparison, and of equal importance, consists of determining the effect of varying the heat transfer coefficient on the stress levels at the external surface (point of maximum stress). Again, only a comparative evaluation is required, so the steady-state temperature profile was considered adequate.

Substituting equation (5.9) for the temperature into equation (3.3) and integrating yields the pressure developed in the molten core. The result, written in non-dimensional form, is

$$\frac{P}{E(T_m-T_c)} = \frac{3\left[\left(\frac{a}{R}\right)-\left(\frac{a}{R}\right)^3\right]+2\left[\left(\frac{a}{R}\right)-\left(\frac{a}{R}\right)^4\right]\left(\frac{1}{Bi}-1\right)}{\left[1+\left(\frac{a}{R}\right)\left(\frac{1}{Bi}-1\right)\right]\left\{1+2\left(\frac{a}{R}\right)^3+\nu-4\nu\left(\frac{a}{R}\right)^3+\frac{2}{3}\,\frac{E}{K}\left[1-\left(\frac{a}{R}\right)^3\right]\right\}} \qquad (5.12)$$

and the tangential pressure stress component of equation (3.2) is

$$\sigma_{Pt} = \frac{Pa^3(2r^3 + R^3)}{2r^3(a^3 - R^3)} \qquad (5.13)$$

Similarly, substituting equation (3.7) into the thermal stress component of equation (3.2 yields the tangential thermal stress as

$$\sigma_{tt} = \frac{2\alpha E(T_m - T_c)}{1-r}\left\{ \frac{2\left(\frac{r}{R}\right)^3 + \left(\frac{a}{R}\right)^3}{2\left[1-\left(\frac{a}{R}\right)^3\right]\left(\frac{r}{R}\right)^3} \; \frac{\frac{1}{2}\left[\left(\frac{a}{R}\right) - \left(\frac{a}{R}\right)^3\right] + \frac{1}{3}\left(\frac{1}{Bi} - 1\right)\left(\frac{a}{R}\right) - \left(\frac{a}{R}\right)^4}{\left[1+\left(\frac{a}{R}\right)\left(\frac{1}{Bi} - 1\right)\right]} \right.$$

$$+ \frac{1}{2\left(\frac{r}{R}\right)^3}\left(\frac{\frac{1}{2}\left(\frac{a}{R}\right)\left[\left(\frac{r}{R}\right)^2 - \left(\frac{a}{R}\right)^2\right] + \frac{1}{3}\left(\frac{a}{R}\right)\left(\frac{1}{Bi} - 1\right)\left[\left(\frac{r}{R}\right)^3 - \left(\frac{a}{R}\right)^3\right]}{\left[1+\left(\frac{a}{R}\right)\left(\frac{1}{Bi} - 1\right)\right]} \right) \qquad (5.14)$$

$$\left. - \frac{1}{2} \frac{\left(\frac{a}{R}\right)\left[1+\left(\frac{r}{R}\right)\left(\frac{1}{Bi} - 1\right)\right]}{\left[1 + \left(\frac{a}{R}\right)\left(\frac{1}{Bi} - 1\right)\right]} \right\}$$

Utilizing the values of the solidification front position with respect to time over the range of interest (as shown in Figure 5.14, which is an expanded view of Figure 5.13), the total surface tangential stress was calculated, and plotted as seen in Figure 5.15. Not until the value of h falls below approximately 10 cal/sec cm^2°C does any significant variation occur. The interesting fact is that even though the pressure developed in the molten core decreases with decreasing heat transfer coefficients, the solidification rate is retarded, creating a thinner shell which yields an increased pressure stress. The thermal stress, on the other hand, decreases with decreasing values of h. However, as h decreases, the pressure stress begins to dominate the thermal stress and rises rapidly enough to cause the total stress to increase over the initial value based on a nucleate boiling h. As was seen in Figure 5.13,

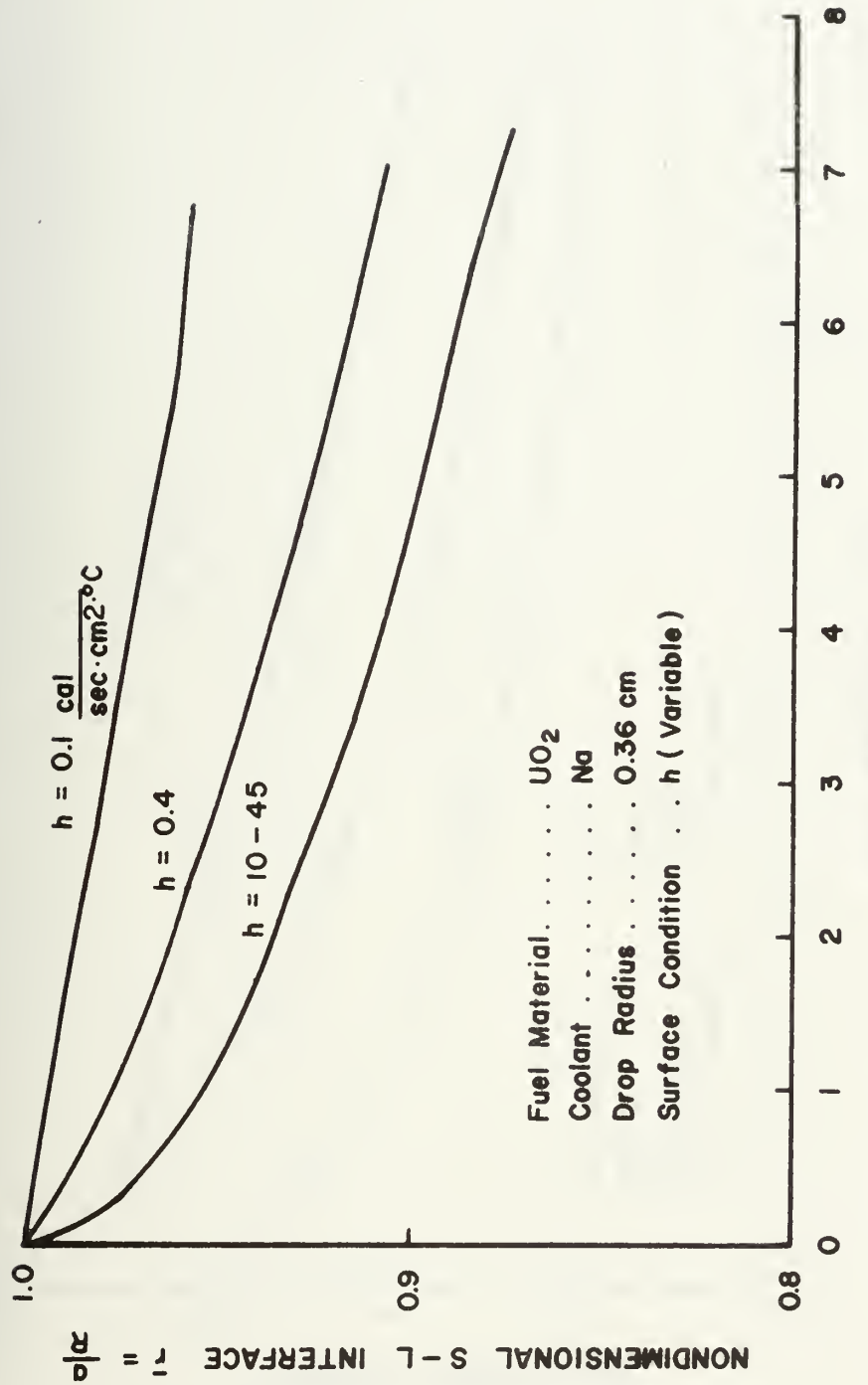

Figure 5.14--Expanded view of interface position (Figure 5.13) for short times.

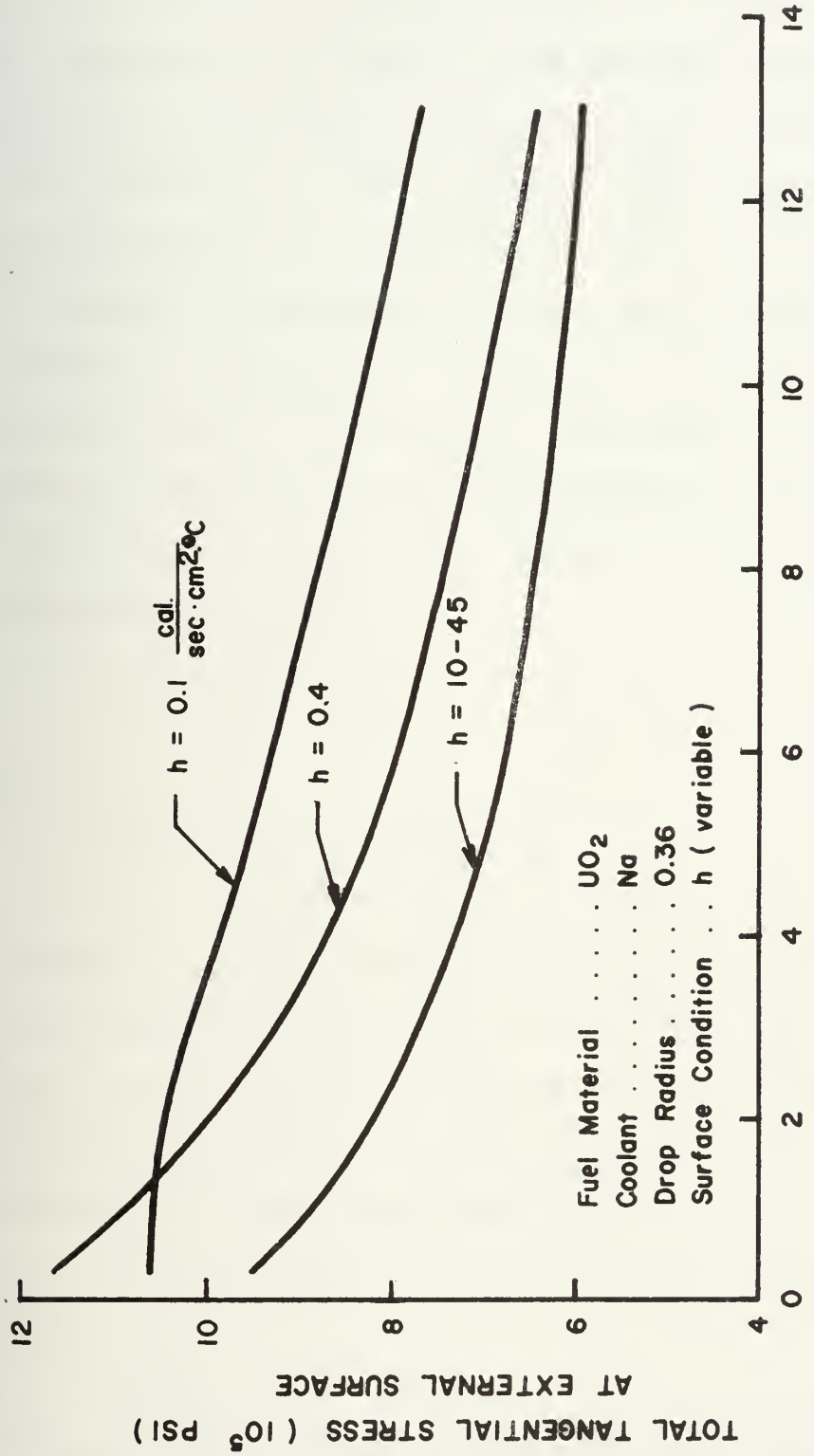

Figure 5.15--Total tangential surface stress for varying surface heat transfer coefficients (UO_2/Na).

the fixed surface temperature condition results in faster solidification. As a result, this boundary condition should provide the highest total stress level anticipated.

The values of the heat transfer coefficient were originally selected to reflect a maximum (41.34 Cal/sec $cm^2°C$) roughly corresponding to that for nucleate boiling of sodium and a minimum (.1 Cal/sec $cm^2°C$) below that which would correspond to film boiling. The manner in which these compare to approximate values for trapped fission gases is illustrated in Figure 5.17. Figure 5.17 is based on the approximation that

$$h = \frac{k}{\delta} \tag{5.15}$$

where

k = thermal conductivity

δ = film thickness

The values for thermal conductivity employed were selected with the value for helium as an upper bound and a value 1/10 of that for helium for a lower bound. The value of k for helium was taken at a mid-range film temperature from Figure 5.16 which was based on (115)

$$k = 0.002418(991 + 0.678((T/1.8 - 1200)) \tag{5.16}$$

for

$$1600°R < T < 6000°R$$

The overall range of film thicknesses which roughly corresponds to the values of h used is from 4×10^{-6} to

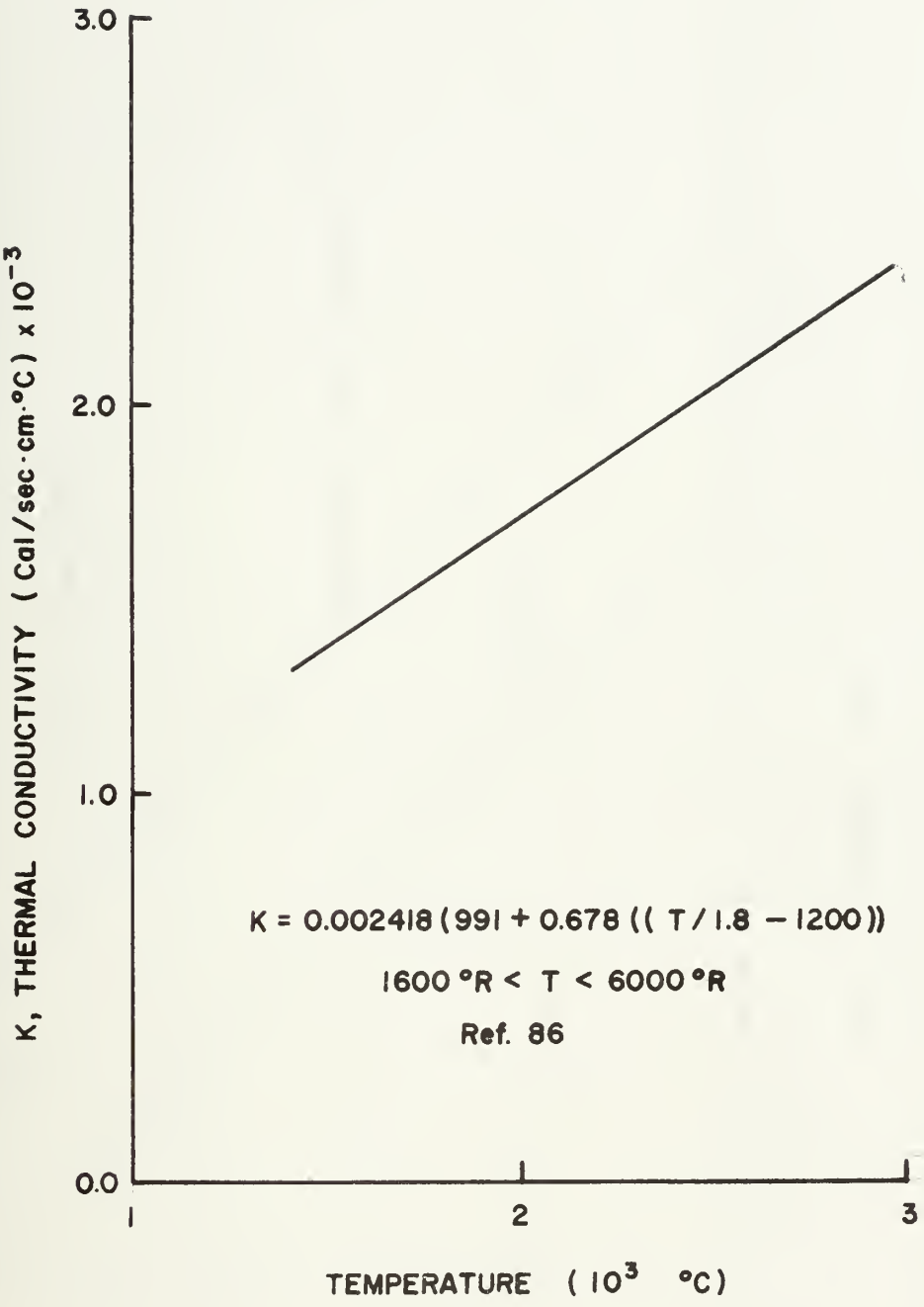

Figure 5.16--Thermal conductivity of helium.

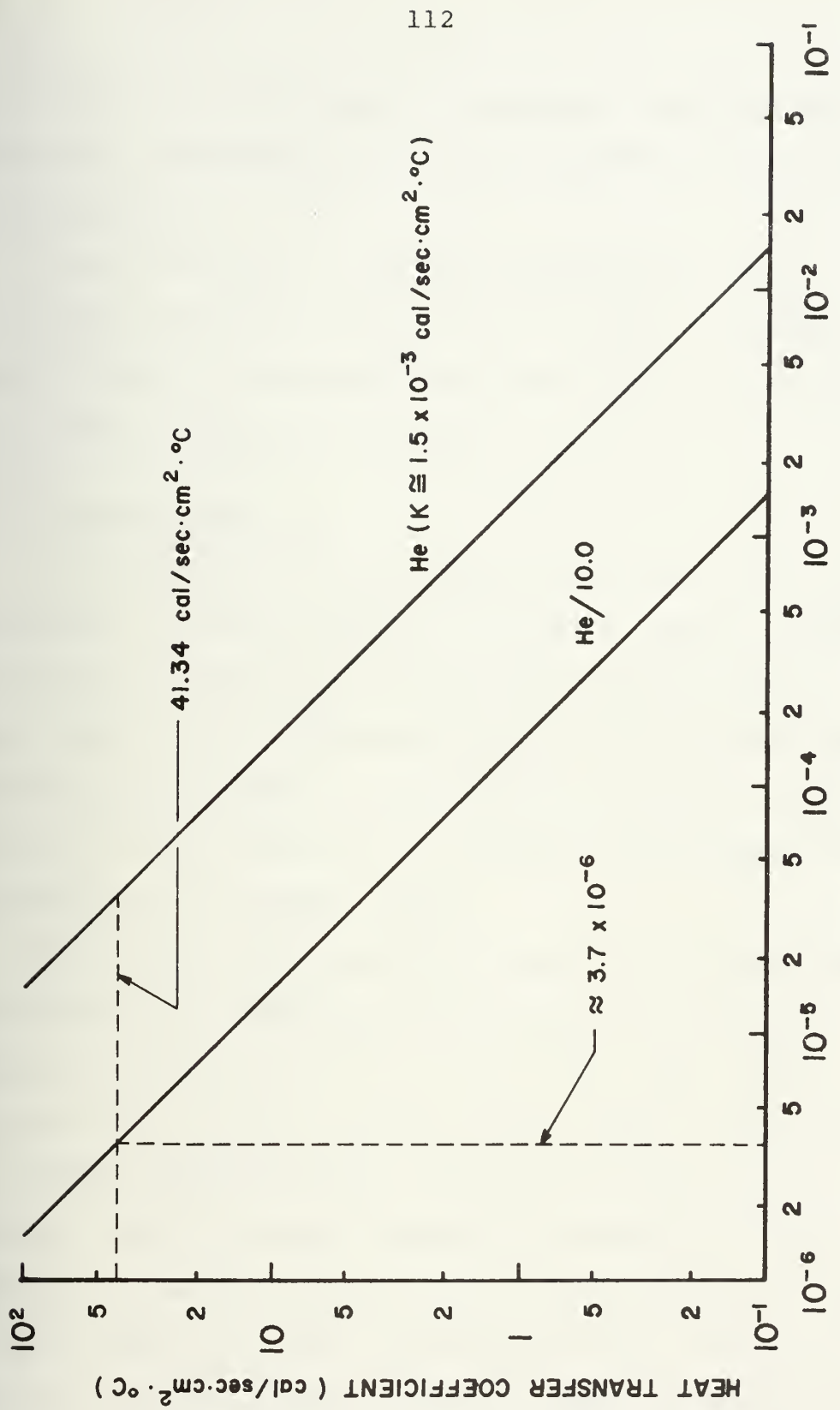

Figure 5.17--Approximate fission gas h for various film thicknesses.

1.5×10^{-2} cm. This range is considered broad enough to adequately represent the values anticipated in the actual UO_2-Na system.

From this study, it can be concluded that the entrapment of fission gases does not appear to reduce the stress levels in the solidifying shell and in fact can cause them to actually increase.

5.7 One-shot fracture

The one-shot fracture method assumes that once K_I, determined through the use of an analytic model, exceeds the critical value, K_{IC}, catastrophic fracture ensues. Thus, taking the stresses described in the last sections and the analytic model illustrated in Figure 5.3, the value of K_I at a given time can be computed and compared to K_{IC} to determine if fracture occurs.

Taking as a representative example the stress field in the shell for the UO_2-Na system with the interface temperature fixed, at $t = 5.76 \times 10^{-2}$ sec (see Figure 5.18), a value of $K_I = 7.67 \times 10^4$ psi $\sqrt{\text{in}}$ is found to exist for an assumed length of 75 μm. Since this value of K_I is greater than K_{IC}, crack propagation, according to this theory, will occur. Further, since the magnitude of the stresses does not change significantly over the first 100+ millisec, K_I will always exceed K_{IC} over this range for the same size crack or larger. Therefore, any flaw

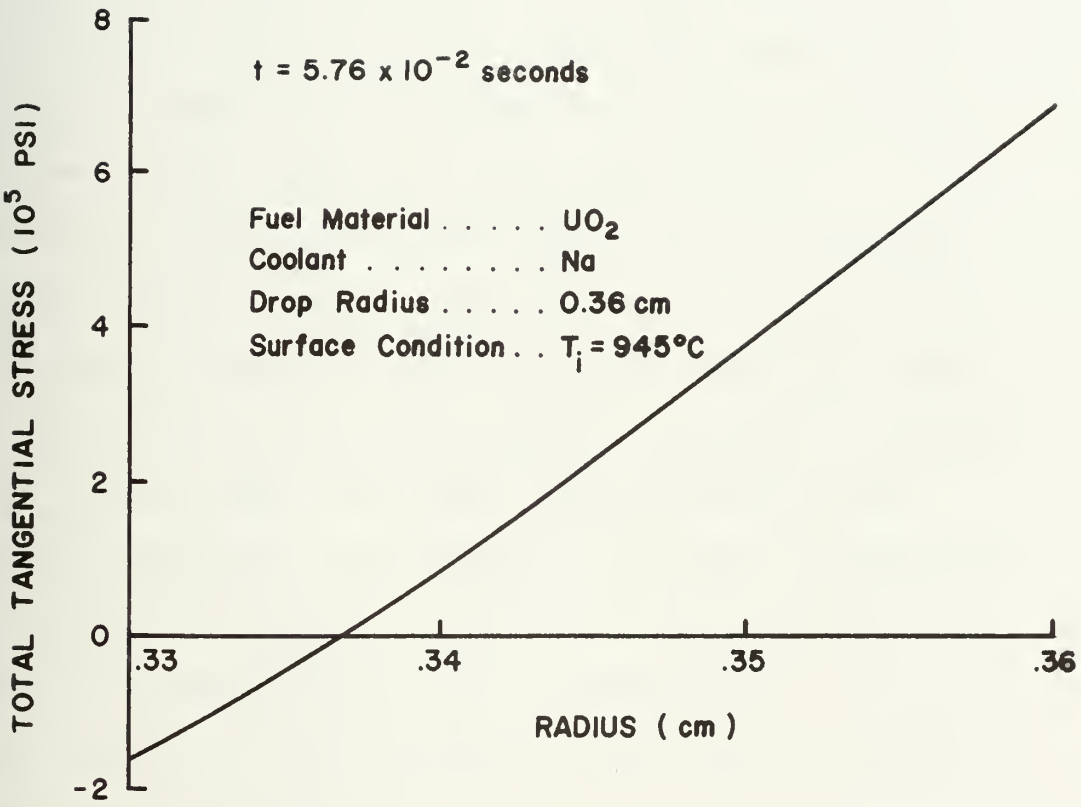

Figure 5.18--Total tangential stress distribution across the shell.

generated in the shell corresponding to a size of 75 μm or more would prove catastrophic.

5.8 Progressive crack growth evaluation

In an effort to verify the one-shot approach and to ascertain whether or not crack arrest may occur, an analytical evaluation of K_I with the crack progressing across the shell was undertaken. The model employed in this case was based on that of Ref. 116 for calculating the thermal stress intensity factor based on the superposition method. This model was initially derived for calculating the stress intensity factor for a plate with one face subject to sudden cooling, and with a flaw at or near the surface being cooled. The thermal stresses, $\sigma_y(x)|_t$, in the crack free plate (determined from the momentary temperature distribution) are used in conjunction with the known solution for a crack in an infinite plate loaded at its surfaces by a pair of wedge forces to obtain K_I via integration over the crack. The analytic solution for this case is given as

$$K_I\Big|_t = 1.12 \frac{2\sqrt{c}}{\sqrt{\pi}} \int_0^c \sigma_y(x)\Big|_t \frac{}{c^2 - x^2} dx \qquad (5.17)$$

where c is the crack depth. The y direction is parallel to the plate surface, while the x direction is parallel to the penetrating crack. The factor 1.12 describes the influence of the stress free surface where the crack

starts. The effect of the finite plate width is not considered in this formula.

In this case, as with the one-shot approach, the possibility of brittle fracture is dependent on the actual crack tip stress intensity factor, K_I, exceeding the critical stress intensity factor of the material, K_{IC}. As K_{IC} may be locally temperature dependent, and as K_I is a function of geometry (crack depth) and the time dependent thermally induced stresses, the basic criterion for rapid crack extension can be expressed as (116)

$$K_I(\sigma_{therm}, c) \equiv K_I(t,c) \geq K_{IC}(T) \qquad (5.18)$$

Using a quasi-static analysis, the variation of K_I with crack depth can be determined for each time step.

Extending this model to the case at hand, that of a sphere rather than a plate, should yield a reasonable first-order approximation. Thus, assuming the crack to be long with respect to its depth, the region of the shell containing the crack can be approximated as a rectangular flat plate. The stress intensity factor can then be determined from the stress field in the undisturbed shell via the superposition method, and equation (4) becomes

$$K_I(c)\Big|_t = 1.12 \frac{2\sqrt{c}}{\sqrt{\pi}} \int_0^c \frac{\sigma_t(r)\Big|_t}{a^2 - (R - r)^2} d(R - r) \qquad (5.19)$$

As a result of the connectivity of the sphere, a certain amount of constraint prohibiting the complete

redistribution of the stresses around the crack is inherent. Therefore, an additional moment must be incorporated in an effort to allow for the conservation of the moment across the cracked section. The result will be an added effective stress distribution acting on the crack, causing the value of K_I to increase with crack depth. Some methods have been proposed to incorporate this effect (117) but the validity of such methods is somewhat suspect where, as in this case, the tensile stress is a strong function of position. As a result, such a correction factor has been omitted in this work.

The tangential stress field in the solidified shell, for various positions of the solidification front (i.e., time steps), can be seen in Figure 5.19. The K_I values corresponding to these particular times can then be determined and illustrated as shown in Figure 5.20 (note that the crack position in the shell is non-dimensionalized for plotting convenience). The significant factor illustrated by Figure 5.20 is that the stress intensity factor exceeds the critical value, $K_{IC} = 2.407 \times 10^4$ psi$\sqrt{\text{in}}$, almost instantly and it remains so thereafter. The time to fracture is then related to the time response of the thermal effects, and as soon as solidification begins and stresses are generated, fracture will ensue. This seems to verify the initial outcome of the one-shot approach discussed earlier. Note that the reason for the

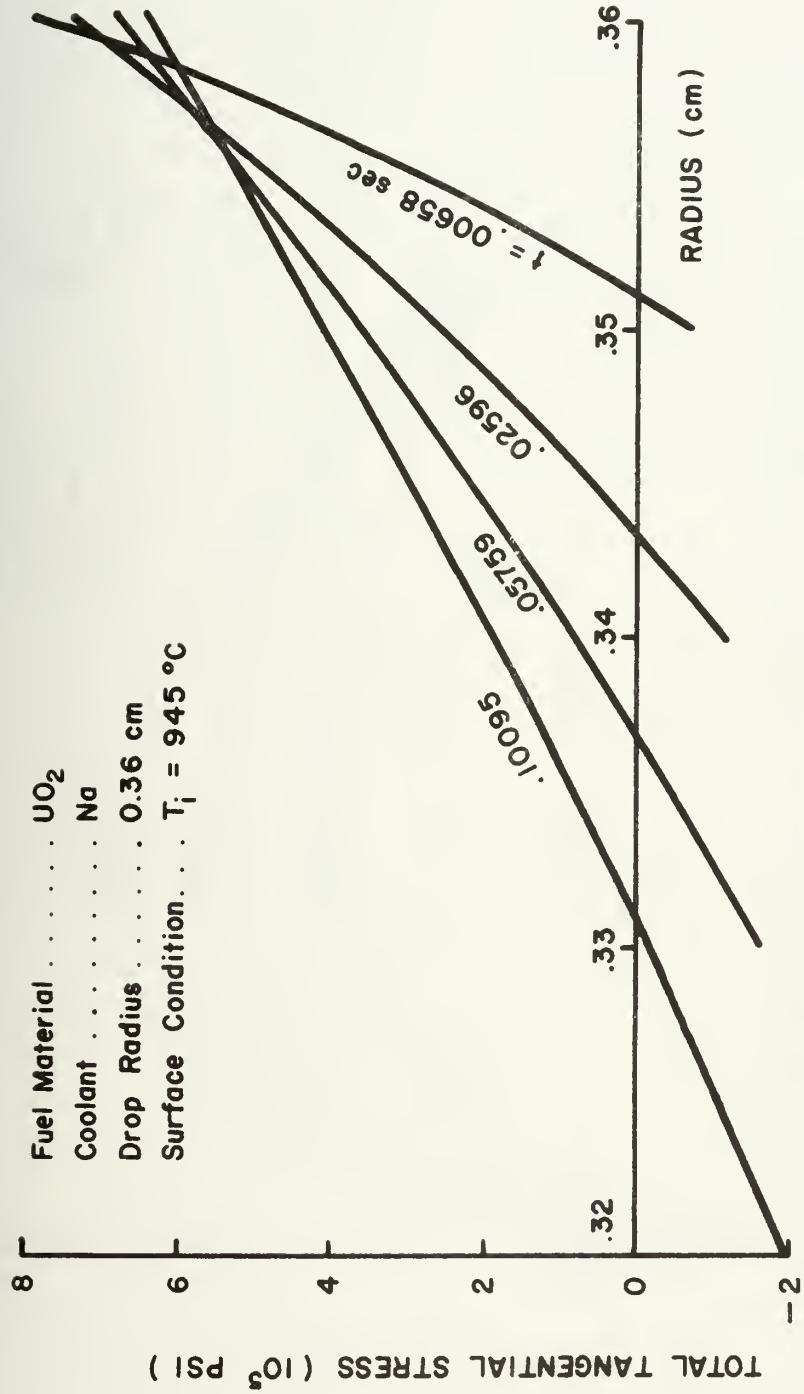

Figure 5.19--Total tangential stress distribution across the shell for progressive times.

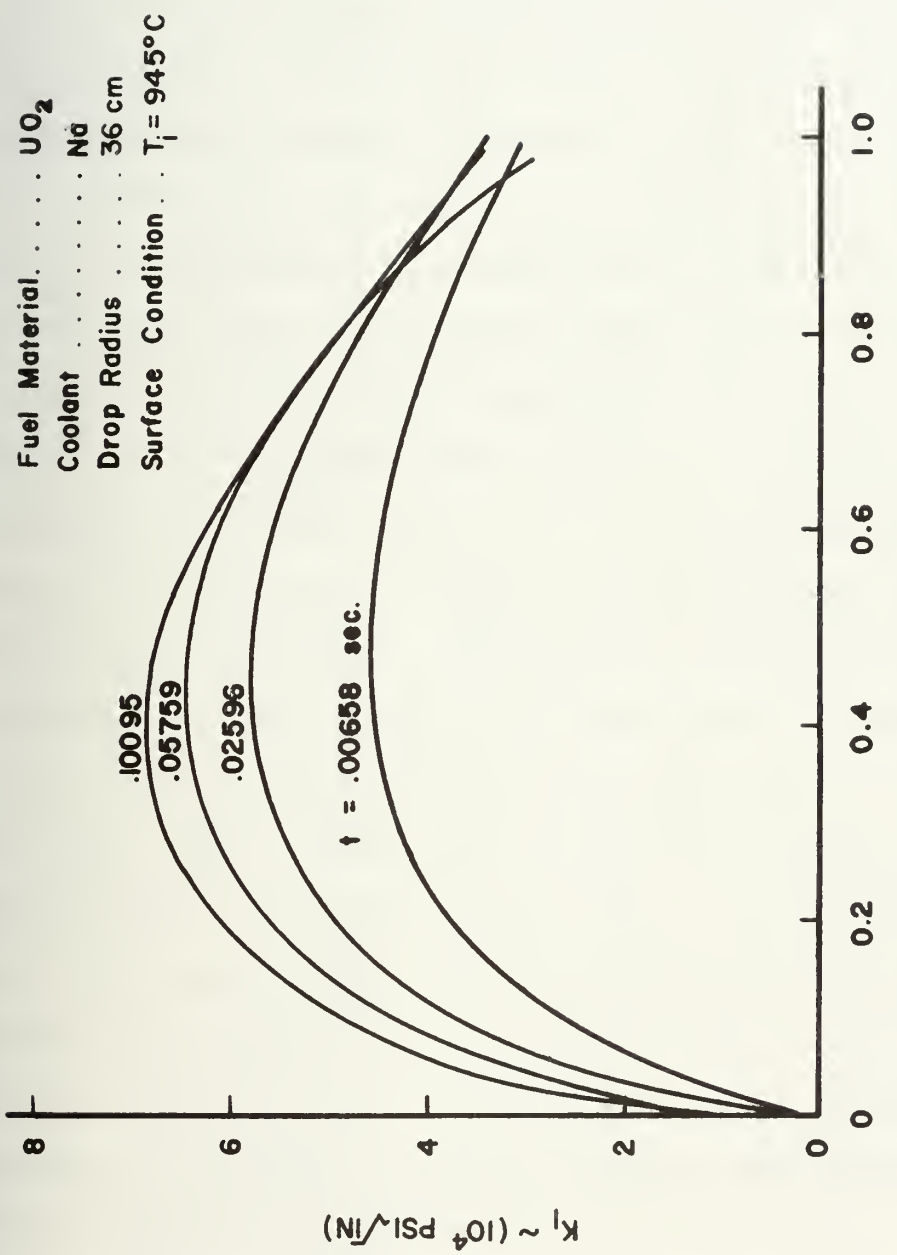

Figure 5.20--Stress intensity factor variation with crack depth.

rapid drop in the value of K_I as the crack is made deeper for a given time step is a result of the strong radial dependence of the stress field.

If, upon penetration of the shell by the initially activated flaws, the internal pressure is relieved, it may be possible to have the value of K_I for remaining flaws fall to zero within the shell. If this were the case the arrest of subsequently generated flaws is possible. Thus, the next step was to investigate this last hypothesis. Figure 5.21 was established using only the value of the thermal stresses through the shell, i.e., assuming that the pressure had been relieved. As crack propagation only results if the crack tip stress intensity factor is greater than the critical value, the decrease in the K_I curves for the case of thermal loading only would seem to imply that cracks of growing depth would be arrested as K_I falls below K_{IC}. This is only true if the crack exhibits stable growth, where no excess kinetic energy is available to drive the crack further. The exact point of arrest, directly influenced by dynamic effects, does not lend itself to simple analysis. The actual stability of the crack extension is dependent on the initiation mechanism and energy conversion rates involved.

Crack stability is difficult to accurately predict. Various studies have been carried out (118, 119, 120), and thermal stress crack stability has received some limited

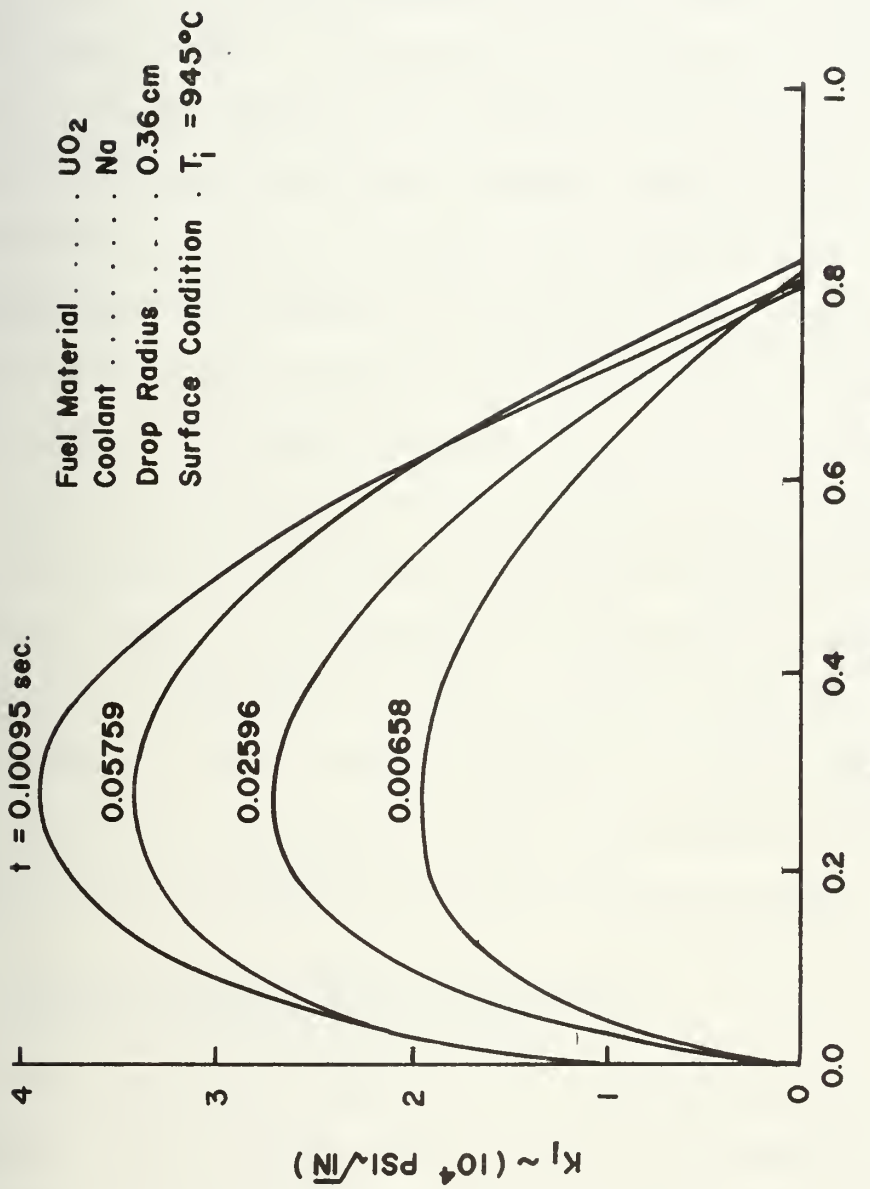

Figure 5.21--Stress intensity factor variation with crack depth (thermal stress only).

attention (119). As yet, however, no theories are available for crack stability and propagation in transient non-uniform thermal stress fields as exist in the present model. In general, if upon propagation the elastic energy release rate exceeds the surface energy required to form new crack surface, the remainder is converted into kinetic energy. The crack, once propagated, will continue to grow until all the kinetic energy and further released strain energy has been converted into surface energy.

The rapid rise of the stress level in the shell for the case at hand, along with the magnitude of those stresses leads to an assumption of unstable growth. A qualitative assessment of Refs. 118-120 tends to support this theory. Thus, even if pressure relief occurs with propagation of the initial flaws, subsequently initiated flaws are anticipated to be catastrophic as well.

5.9 Effect of grain size and porosity on brittle fracture strength

Various factors can have an influence on the fracture strength, and in turn the K_{IC} value, of a material. In the case of brittle ceramics, such as UO_2, the two most important parameters in this category are grain size and porosity. The effects of these factors are not known in detail, but general experimental trends have resulted in qualitative assessments of their influence.

One attempt at establishing an empirical relationship for the combined effect of grain size and porosity is that of Knudsen et al. (121), which is given as

$$S = KG^{-a}e^{-bP} \tag{5.20}$$

where S is the fracture strength, G represents the mean grain size (μm), P represents the fraction of porosity, and K, a and b are all empirical constants. This formulation is based on overall experimental trends, and it becomes coupled with a third influencing factor, temperature. Generally, an increase in temperature tends to strengthen specimens with a low porosity and a fine grain size, and to weaken those with a high porosity and a large grain size. Also, an increased sensitivity to changes in porosity and grain size has been noted at high temperature (122).

In many cases, the effect of grain size on the maximum stress and/or the onset of plastic strain appears to be relatively small (123). This apparant contradiction can be attributed to the fact that Knudsen et al. (121) were concerned with critical flaws on the order of the size of the grains, whereas the experimental observations of Refs. (111) and (123) were based on much larger critical flaws; thereby the grain size effect became less important. Furthermore, in the brittle fracture region, under consideration here (comparable to the low temperature region of testing) it is extension of the pre-existing,

inherent flaws which determines the fracture stress. Thus, it is the flaw size and not the grain size that becomes of major importance.

The specific effects of porosity depend on such factors as: whether deformation is elastic and fracture brittle, fracture is preceeded by plastic flow, or extensive plasticity occurs. Further, there will be a critical strength dependence on pore morphology, and the operating conditions of temperature, stress, and/or strain rate.

In the region of interest, that of brittle fracture, an increase in porosity yields a decrease in strength. The magnitude of this effect is determined by pore size, shape and distribution (124). Large pores allow for easier fracture initiation and crack propagation, and the stress to extend these flaws determines the fracture stress. This porosity effect on the fracture stress is also related through the influence on the modulus of elasticity.

Another interesting effect results from the fact that at high strain rates, increased porosity yields brittle behavior (124). This is even true at moderately high temperatures. If the strain rate is decreased, however, plasticity may develop. As well, a density relationship with porosity has been shown to have an effect on the crack behavior of UO_2 (124). In the case of high density, a single through crack develops, but with lower density material, many part-through cracks were observed. A point to note is that not only could stress relief stop the

cracks, but the onset of plasticity could allow crack blunting and subsequent arrest.

As to the effect of grain size and porosity on the present analysis, the impact is not considered to be very critical. As the strain rate is high and the fracture mode brittle, grain size effects should be minimal. Further, from the data of Ref. 111, the slight increase in fracture stress for a smaller grain size would offset the slightly smaller critical flaw size in the calculation of K_{IC}, yielding essentially the same value.

A variation in the porosity could have a more significant impact. The greatest effect would be in altering of the average pore size, which, being the critical flaw size, alters the fracture stress. However, the direct dependence of K_{IC} on both flaw size and fracture stress tends to dampen the variations as there is an inverse relationship in the brittle region (121). This fact, along with the knowledge that the induced K_I values greatly exceed K_{IC} (requiring large variations in K_{IC} to make any noticeable difference) have led to the qualitative conclusion that the K_{IC} value employed herein is adequate.

5.10 Density change effect

When UO_2 solidifies, there is a change in the material density, and this perturbation on the problem is unaccounted for in previous sections of this report. In an

effort to determine the relative magnitude of the resulting effect and the consequences in light of the developing stresses, a parametric evaluation was conducted.

The first estimate was based on determining the magnitude of the developing void which would form if the outside radius of the drop remains fixed. A further simplification was made by assuming that the void developed uniformly in the liquid and had no effect on the progression of the solidification front. This may prove to be a poor approximation, as the void would be concentrated at the upper portion of the spherical drop (gravity/buoyancy effect) and thus inhibit solidification in this region. However, as the precise shape of the developing void is unknown, this approximation was considered adequate for initial estimates.

For this first case of R_o (outside radius) fixed, the initial mass of the drop is given as

$$m_o = \rho_\ell V_o = \frac{4}{3}\pi R_o^3 \rho_\ell \tag{5.21}$$

After a subsequent time step, the mass of developed solid is

$$m_s = \frac{4}{3}\pi(R_o^3 - a^3)\rho_s \tag{5.22}$$

and the volume of solid

$$V_s = \frac{m_s}{\rho_s} \tag{5.23}$$

Defining the void volume as

$$V_{void} = V_o - V_\ell - V_s \tag{5.24}$$

and the void fraction as

$$\text{void fraction} = \frac{V_{void}}{V_o} = \frac{V_o - V_\ell - V_s}{V_o} \tag{5.25}$$

substitution and manipulation leads to the expression

$$\text{void fraction} = \left[1 - \left(\frac{a}{R_o}\right)^3\right]\left(\frac{\rho_s}{\rho_\ell} - 1\right) \tag{5.26}$$

Equating the original mass to the mass of the solid yields an estimate of the final internal radius for complete solidification with R_o fixed (assuming the void is maintained at the center). This expression is given as

$$a = R_o\left(1 - \frac{\rho_\ell}{\rho_s}\right)^{1/3} \tag{5.27}$$

and for the current value of R_o = .36 cm, a = .2124 cm which yields a final void of approximately 20% by volume.

The interesting aspect of this void formation phenomenon is that in its presence, no internal pressurization will develop, and thus, no pressure stresses will be present in the shell.

In an effort to bring the initial estimate closer to reality, and to gain more insight into the actual effects on the pressurization, the thermal contraction of the shell was brought into play. The change in the internal shell radius, due to thermal effects alone, is given as

$$\Delta r_{th} = \frac{a}{E}[\sigma_{tt} - V(\sigma_{rt} + \sigma_{tt})] + \alpha\Delta T(r)a \tag{5.28}$$

It is noted that the limited compressibility of the liquid would inhibit complete thermal shrinkage until a void actually began to form. The first estimate was to calculate the volume reduction due to thermal contraction, and then reducing the generated void by this amount, to determine the actual void production rate. The plot of void generation rate for both the case of fixed R_o and the case of considering thermal contraction can be seen in Figure 5.22. Note that two curves are given for the latter case; one is void fraction based on the original outside R_o, and the other (perhaps the most pertinent) is based on the thermally contracted R_o.

The plot of Figure 5.22 demonstrates the fact that there would be an initial delay time prior to any void formation. This results from the fact that the original shell contraction rate exceeds the rate at which the density change would cause a void to form. As a result, in the early stages of solidification, pressurization will occur. Once the void begins to form, the pressure would rapidly decrease and only thermal stresses would be present in the shell. The net result is that the initial shell stresses will be high enough to successfully propagate an existing flaw. Once the pressure is relieved, the situation would become the same as the non-pressurized

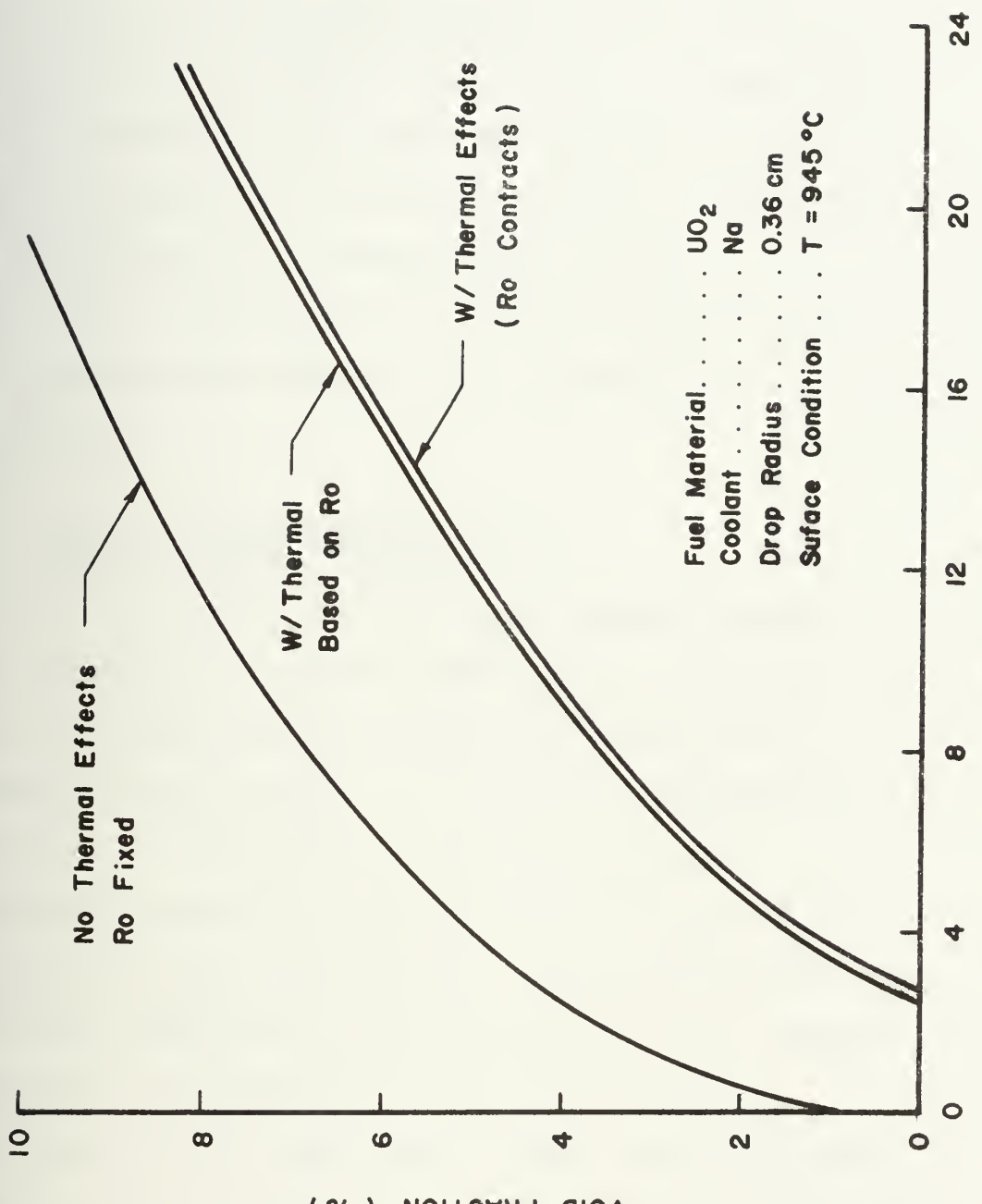

Figure 5.22--Rate of void formation for UO_2 in Na.

case investigated in the fracture section. The only difference is one of higher order, in that the shell structure in the region of the void would no longer be symmetric, and there would be a temperature field perturbation. However, the fracture calculations conducted for the non-pressurized case can be considered adequate for a conservative estimation.

5.11 Constraint developed when Na becomes trapped in UO_2

As described in the review of proposed models, when the contact interface temperature is greater than the homogenous vapor nucleation temperature, spontaneous nucleation of the coolant is possible. This fact, in some cases, could yield a vapor explosion. Normally, as illustrated in Figure 5.23, for UO_2 in sodium, the contact temperature is well below the spontaneous nucleation temperature. However, as pointed out by Fauske (74), this mechanism might apply to the case where a small amount of sodium becomes trapped in molten UO_2 and is subsequently heated to its homogenous nucleation temperature. It is of interest, therefore, to investigate the inverse problem of Na trapped in UO_2 to determine the amount of constraint

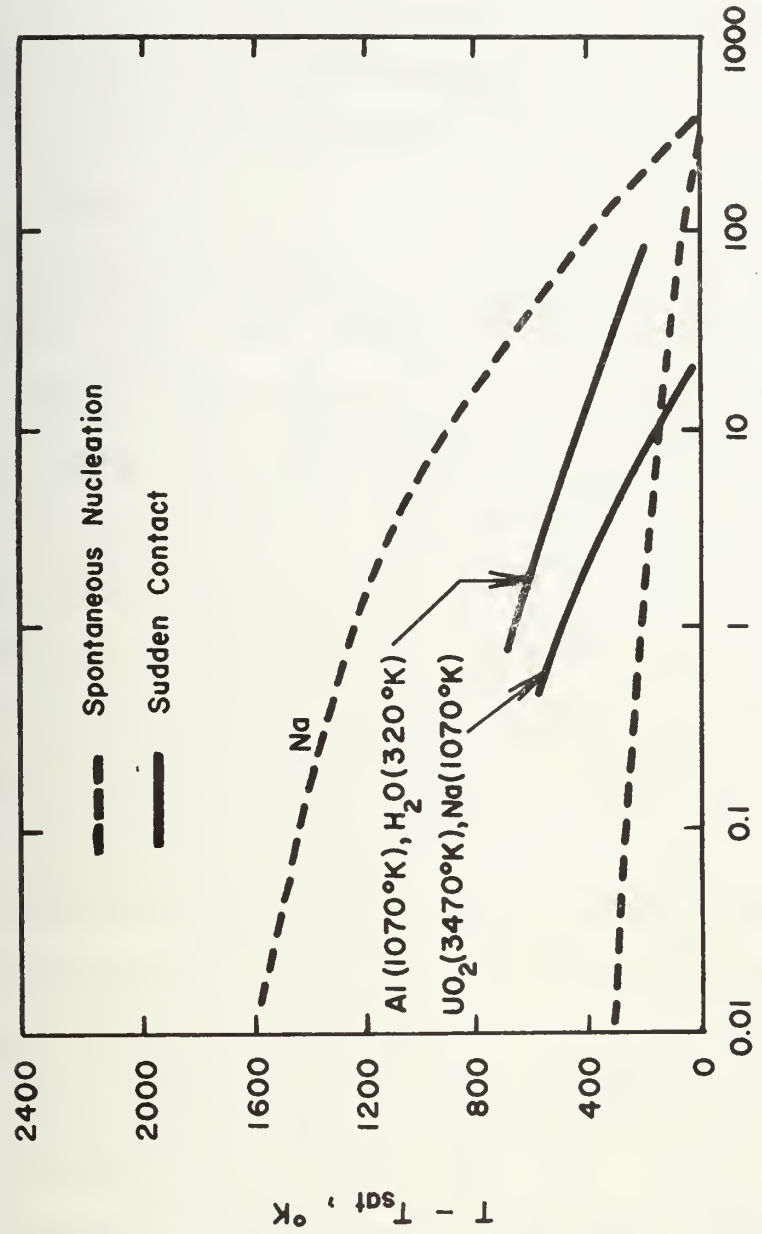

Figure 5.23--Comparison of the UO_2-Na contact interface temperature and that for spontaneous nucleation (73).

supplied by the solidifying UO_2 shell when the sodium reaches the point of spontaneous nucleation. Thus, a crude, first-order estimate was carried out for just this purpose.

The physical problem is postulated as illustrated in Figure 5.24. The internal sodium droplet is assumed spherical in shape and since it has a high thermal conductivity, its temperature is considered uniform, at an average value, for solidification calculations. As well, the external solidification front temperature is assumed to be constant at the UO_2 melting point, and the steady-state approximation of London and Seban is again utilized to evaluate the rate of advance of the solidification front. The method employed is a quasi-static analysis based on an energy balance. At each time step, the energy balance allows estimation of a new sodium temperature which can then be used to determine the solidification front movement to the next time step. Once the Na has exceeded its spontaneous nucleation temperature, the process is terminated.

The energy change in the sodium can be approximated as

$$\Delta E_{Na} = Mc_p\Delta T - [V\rho c_p(T_2 - T_1)]_{Na} \qquad (5.29)$$

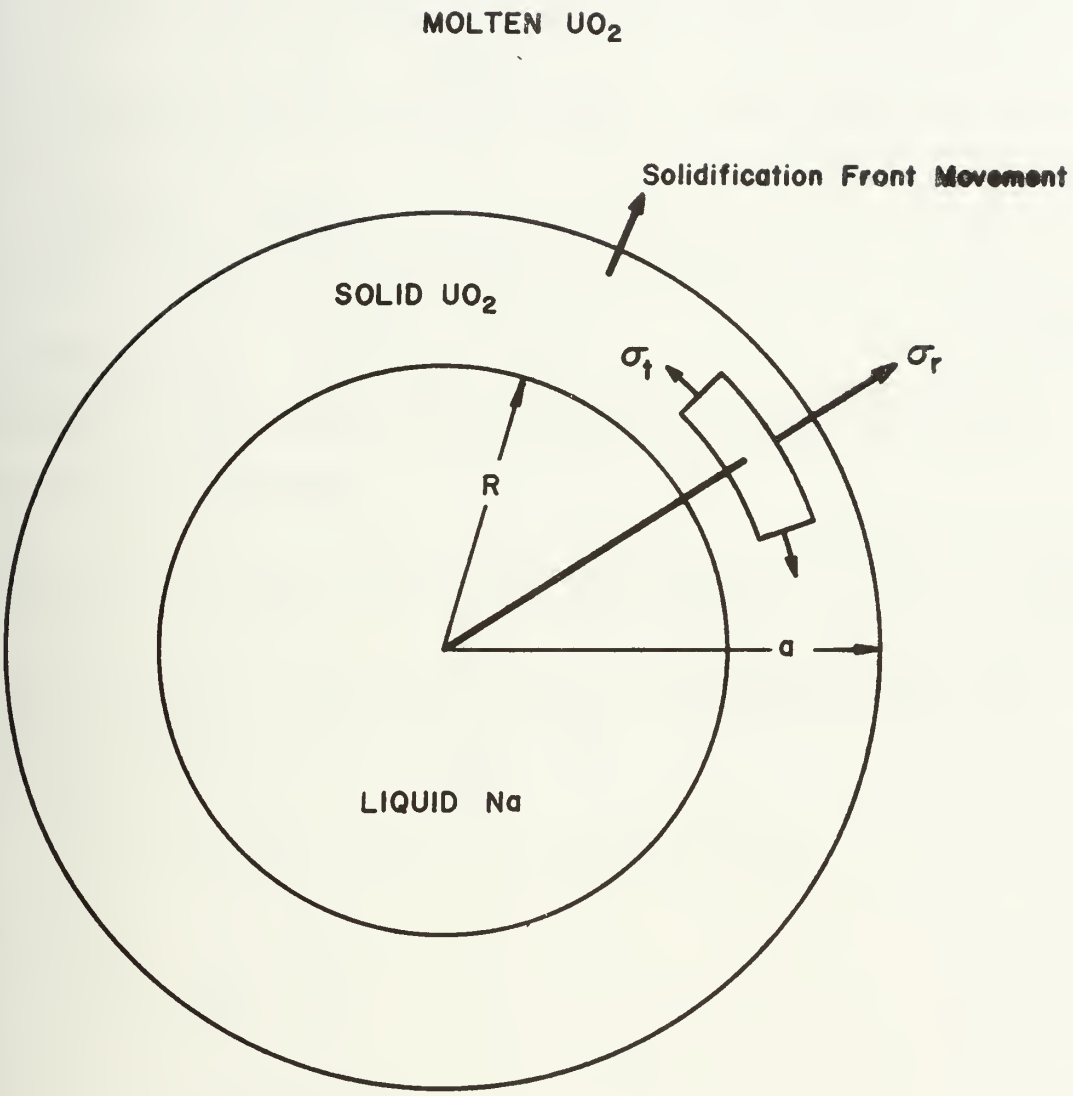

Figure 5.24--Liquid Na trapped in molten UO_2.

while that for the UO_2 is

$$E_{UO_2} = (Mc_p\Delta T)_{shell} + (ML)_{\substack{solidified \\ shell}} + (Mc_p\Delta T)_{liquid} \qquad (5.30)$$

$$= [Vc_p(T_{outside} - T_{inside})]_{shell} + (V\rho L)_{shell}$$

where $T_{outside} \equiv T_{melt}$.

The volume of solid shell added per time step is

$$V_{solid\ added/step} = \frac{4}{3}\pi(a^3_{new} - a^3_{old}) \qquad (5.31)$$

Equating the energy changes, substituting and manipulating leads to the following:

$$R^3\rho_{Na}c_{p_{Na}}(T_2 - T_1)_{Na} = [(T_m - T_1)\rho_{solid}c_{p_{solid}} + L](a^3_{new} - a^3_{old}) \qquad (5.32)$$

The solidification equation, similar to equation (19) for the inverse problem now becomes (79)

$$\bar{t} = \frac{1}{3}\left(\frac{1}{Bi} + 1\right)[\bar{r}^3 - 1] - \frac{1}{2}[\bar{r}^2 - 1] \qquad (5.33)$$

where

$$\bar{r} = a/R$$

and

$$\bar{t} = -T_{Na}kt/LR^2$$

Initially, to estimate a reasonable size and time step to use, a preliminary calculation was carried out. In this case a sodium drop is assumed to be instantly submerged in a pool of molten UO_2, and the sodium is assumed to have a negligible internal temperature gradient. Also, the effects of UO_2 solidification are neglected. For this case, the energy balance is written as

$$A_{Na\ surface} h(T_{Na} - T_f\ dt) = V\rho c_p\ dt \qquad (5.34)$$

which yields

$$t = \left(\frac{V\rho c_p}{A}\right)_{Na} \frac{1}{h}\ \ell n\left(\frac{T_f - T_1}{T_f - T_2}\right)$$

$$t = \frac{R}{3}\ \frac{\rho_{Na} c_{p_{Na}}}{h}\ \ell n\left(\frac{T_f - T_1}{T_f - T_2}\right) \qquad (5.35)$$

where

T_f = surrounding UO_2 temperature

T_1 = initial Na temperature

T_2 = final Na temperature

Taking a value of the sodium spontaneous nucleation temperature of approximately 2000°C (Figure 10) plots of time to spontaneous nucleation versus the surrounding fluid temperature for various Na drop radii and versus drop radii for various values of h can be constructed (see Figures 5.25 and 5.26). Based on this initial investigation, values of R = .3 cm and h = 10 Cal/sec cm^2°C were selected for use in the first-order investigation including solidification. Then, employing equations (26) and (27), and a quasi-static analysis, Figure 2.27 can be developed. This figure shows the average Na temperature and the solidification front variation with time. Noting the time at which the spontaneous nucleation temperature (determination of this value will be subsequently explained) of sodium is exceeded (t = 1.25 msec), the

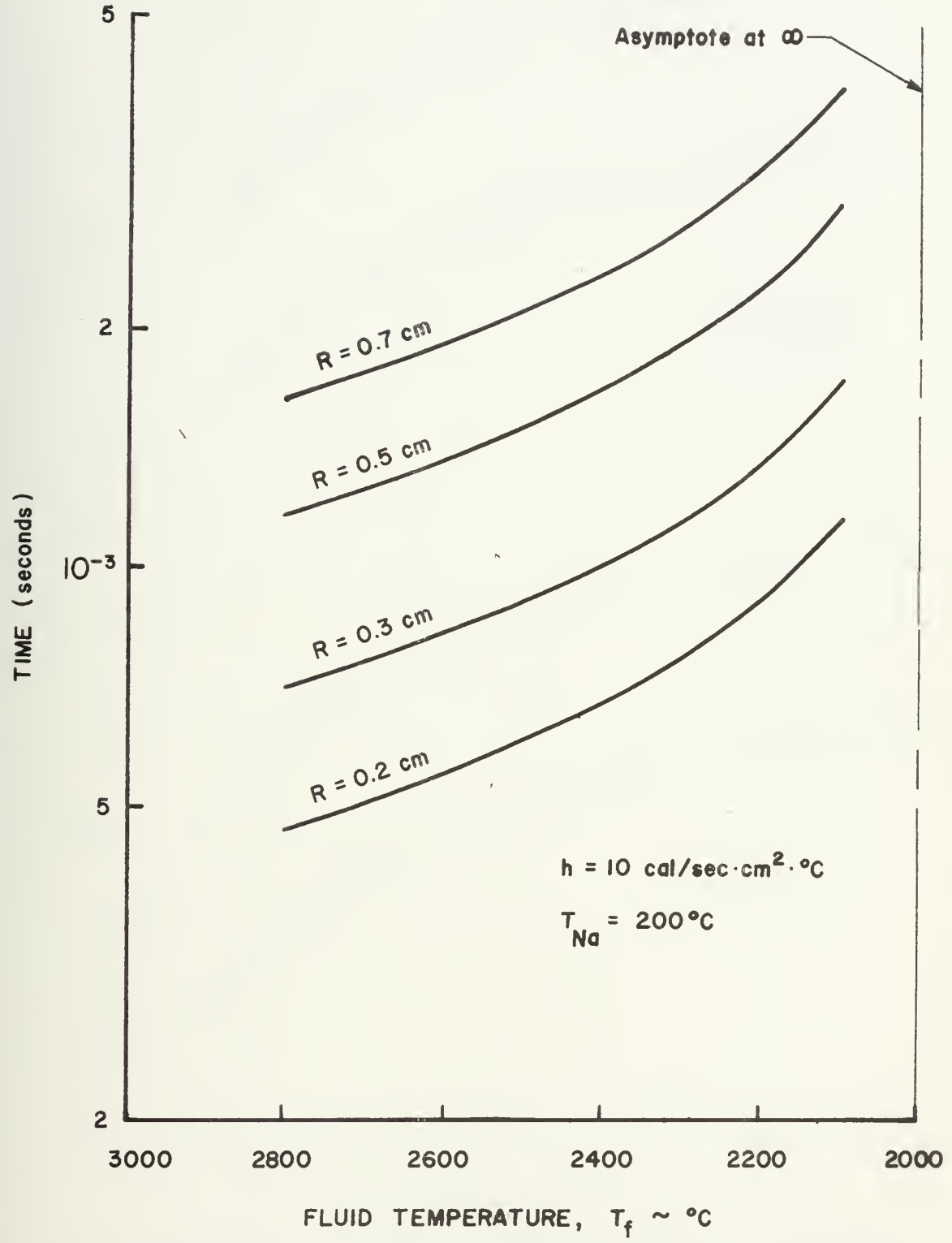

Figure 5.25--Time to spontaneous nucleation for Na versus temperature of surrounding fluid for varying drop size.

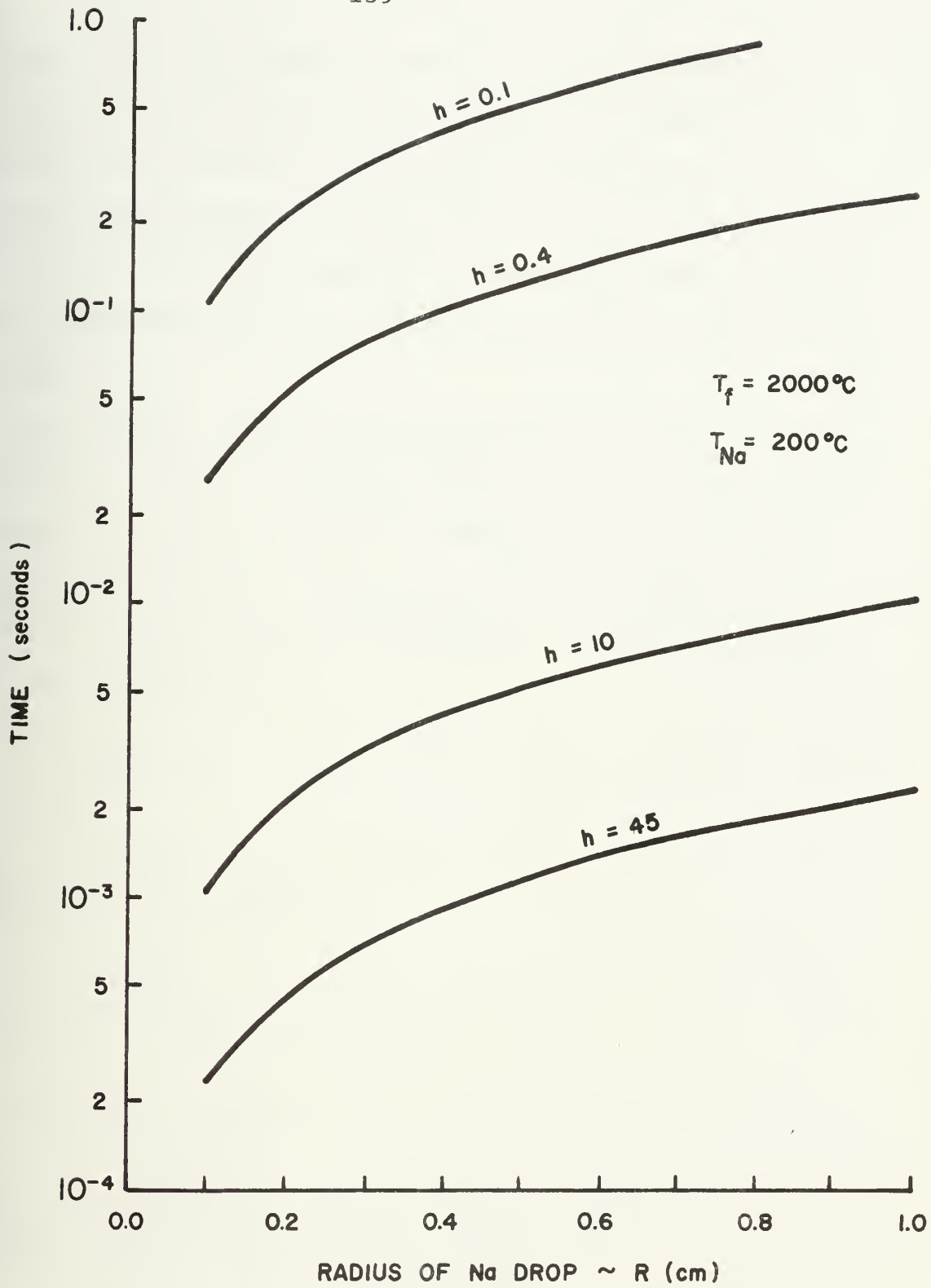

Figure 5.26--Time to spontaneous nucleation for Na versus drop size for varying surface heat transfer coefficients.

position of the solid-liquid interface can be determined (a = .315 cm), and the UO_2 shell thickness is then defined as .015 cm. The value of the spontaneous nucleation temperature shown in Figure 5.27 is based on Figure 5.23 with the saturation temperature and induced pressure being determined as described in the following.

The pressure induced in the sodium during the solidification of the UO_2 is computed neglecting the compressibility effects and the thermal expansion of the Na (offsetting effects). Similar to the development in Ref. 76 the stress effects on the radius of the solidifying shell can be given as

$$\Delta r_{thermal} = \frac{R}{E}[\sigma_{tt} - \nu(\sigma_{rt} + \sigma_{tt})] + \alpha_T T(r) R \qquad (5.36)$$

$$\Delta r_{press} = \frac{R}{E}[\sigma_{tP} - \nu(\sigma_{rp} + \sigma_{tp})] \qquad (5.37)$$

taking $r_{th} = r_{press}$ yields

$$P = \frac{6\alpha_T E}{R^3 + 2a^3 - \nu(4a^3 - R^3)} \int_R^a T(r) r^2 \, dr \qquad (5.37)$$

which, as before, reduces to (in nondimensional form)

$$\frac{P}{\alpha E(T_m - T_c)} = \frac{3\left(\frac{a}{R}\right)\left[\left(\frac{a}{R}\right)^2 - 1\right] + 2\left(\frac{a}{R}\right)\left[\left(\frac{a}{R}\right)^3 - 1\right]\left(\frac{1}{Bi} - 1\right)}{\left\{\left(\frac{a}{R}\right)^3 + 2 - \nu\left[4 - \left(\frac{a}{R}\right)^3\right]\right\}\left\{1 + \left(\frac{a}{R}\right)\left(\frac{1}{Bi} - 1\right)\right\}} \qquad (5.38)$$

Utilizing mean constant values of the thermophysical properties, equation (5.38) leads to the development of Figure 5.28, which shows the pressure history during

solidification. The peaking phenomenon is a result of the heating of the trapped Na, gradually reducing the temperature difference across the shell as solidification proceeds. The decreasing temperature difference reduces the amount of thermal shrinkage and thereby decreases the induced pressure. The vapor pressure versus T_{sat} curve for sodium is based on (125)

$$\log P_{mm} = \frac{-5567}{T} - 0.5 \log T + 9.235 \qquad (5.39)$$

Where T is in °K, and it can be seen in Figure 5.29. Figures 5.28 and 5.29 can be used in conjunction with Figure 5.23 to determine the spontaneous nucleation temperature of sodium with time which is the line plotted in Figure 5.27 and previously described as defining the solidification limit.

Finally, the stresses developed in the solidifying shell can be evaluated to estimate whether or not the shell would remain intact when the sodium reaches the spontaneous nucleation temperature. Thereby, a first-order estimate of the constraint at this time can be obtained. In order to estimate the temperature distribution in the shell, a quasi-static evaluation was carried out based on an isothermal surface boundary condition and constant conductivity in the shell with the temperature given as (84)

$$T = \frac{1}{a - R}\left[T_m\, a\left(1 - \frac{R}{r}\right) - T_i R\left(1 - \frac{a}{R}\right)\right] \qquad (5.40)$$

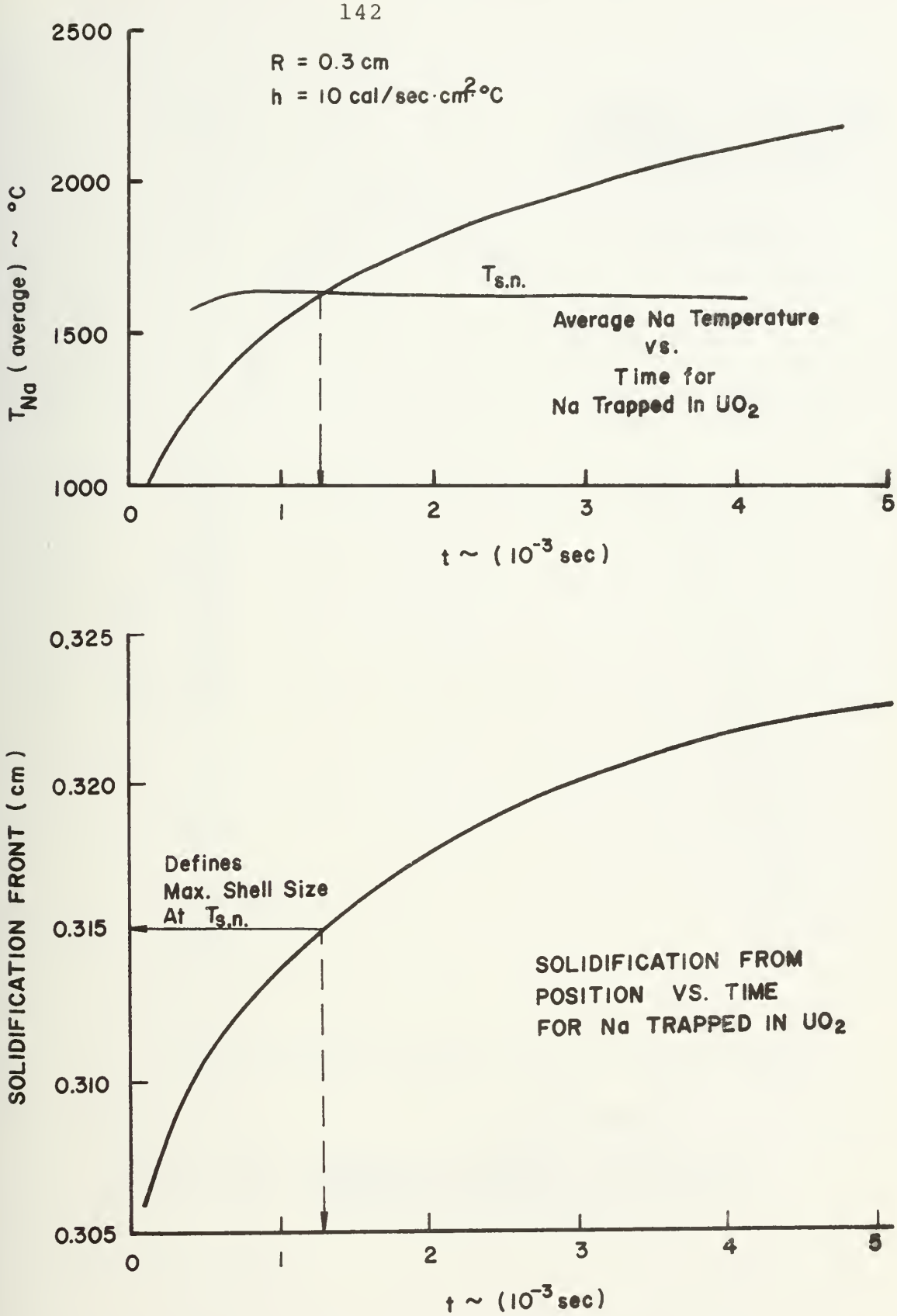

Figure 5.27--Na temperature and solidification front position versus time for Na trapped in UO_2.

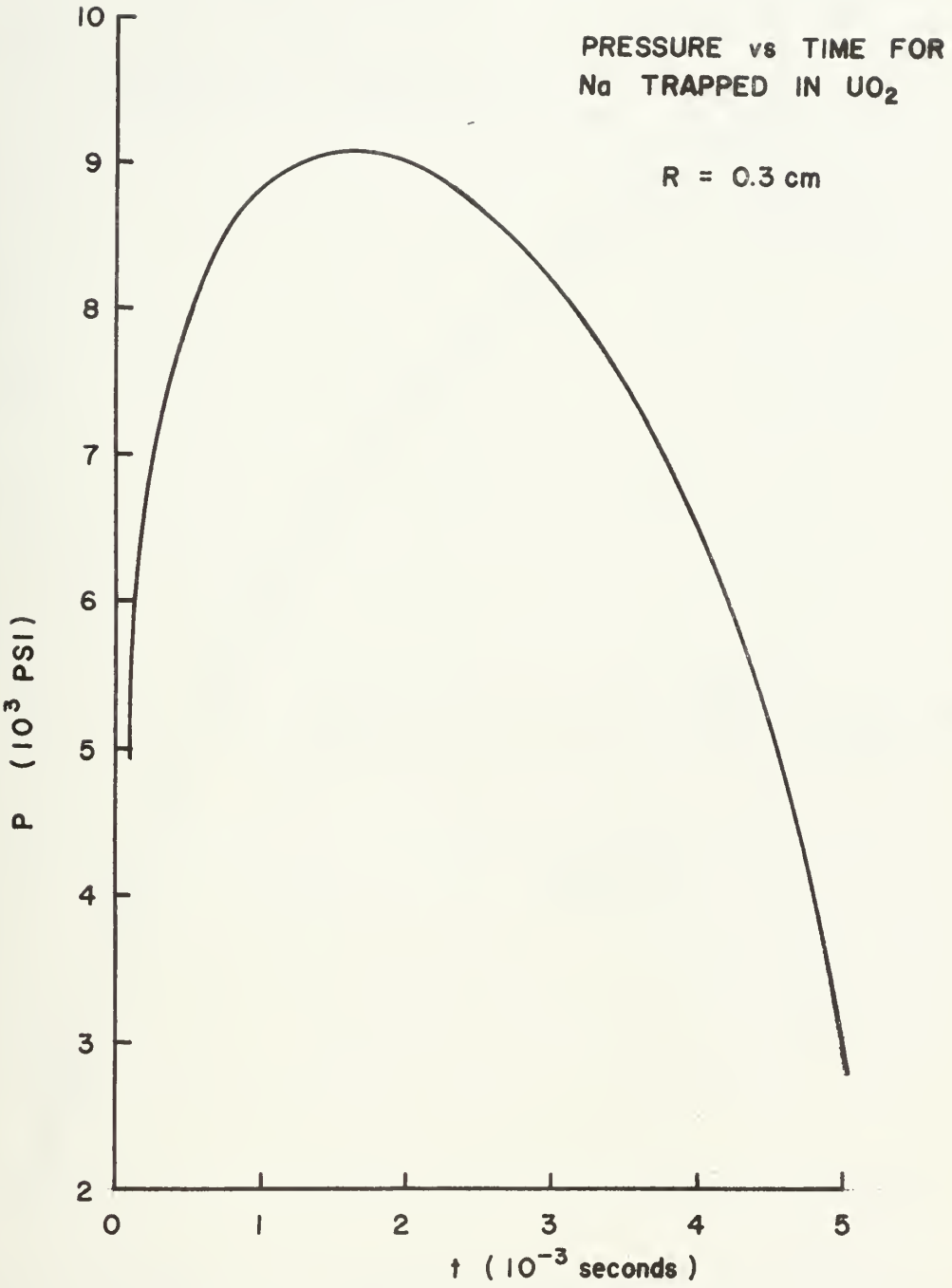

Figure 5.28--Pressure induced in Na droplet trapped in solidifying UO_2.

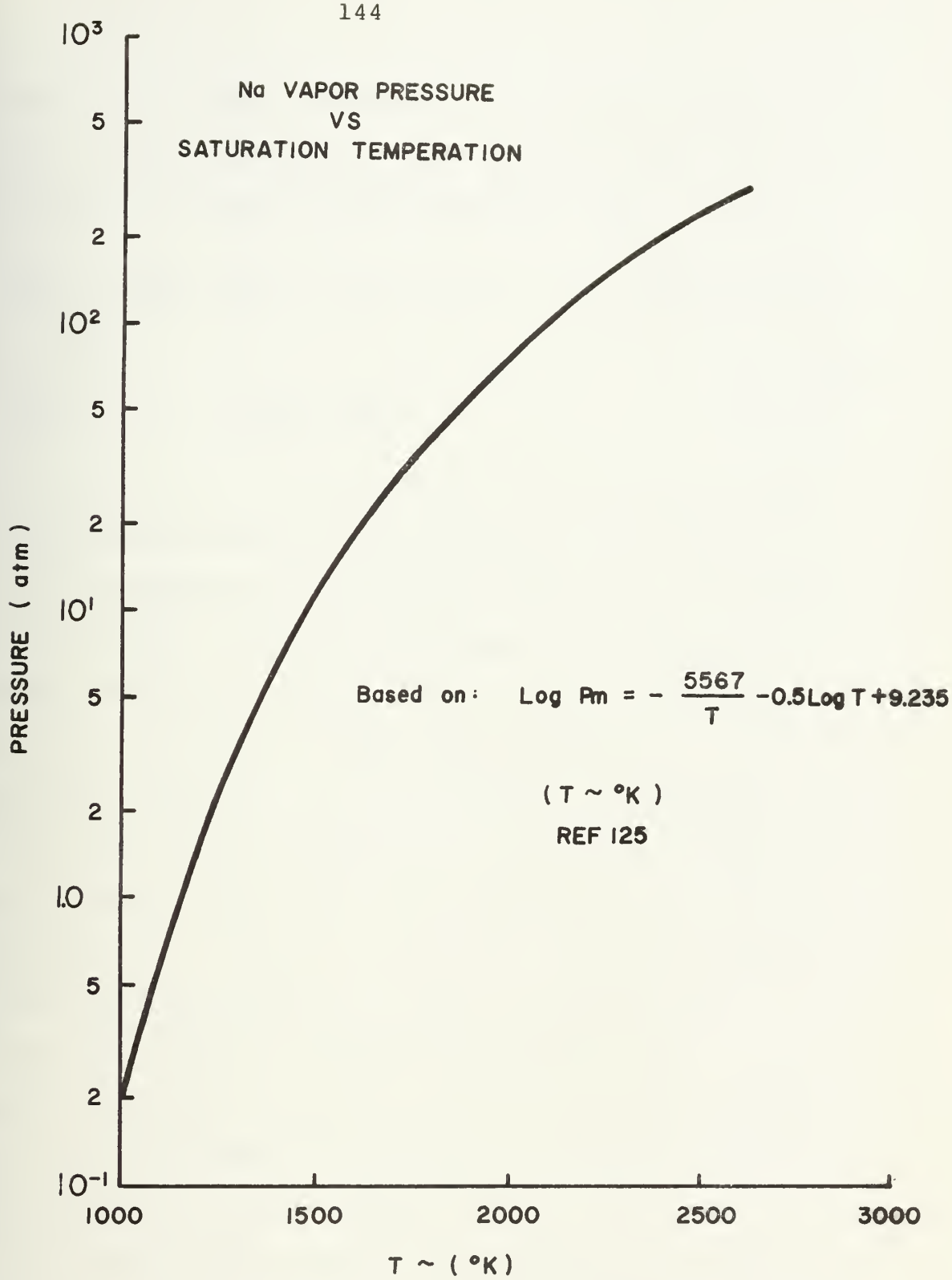

Figure 5.29--Sodium vapor pressure as a function of T_{sat}.

Based on the above temperature distribution and the previously evaluated pressurization (Figure 5.28), the total tangential stress is then calculated from

$$\sigma_t = \frac{2\alpha E}{1-\nu}\left[\frac{2r^3 + R^3}{2(a^3 - R^3)r^3}\int_R^a \bar{T}(r,t)r^2\,dr + \frac{1}{2r^3}\int_R^r \bar{T}(r,t)r^2\,dr - \frac{1}{2}\bar{T}(r,t)\right] + \frac{PR^3(2r^3 + a^3)}{2r^3(a^3 - R^3)} \tag{5.41}$$

which is equation (3.2) rewritten for the inverse problem.

The results of the stress calculations are shown in Figure 5.30 (plotted for the maximum value which is at the internal surface). Note that previously, even when only considering thermal stresses (Figure 5.21) in the original problem, the K_{IC} value of 2.407×10^3 psi$\sqrt{\text{in}}$ was substantially exceeded, i.e., by an order of magnitude. Even though the stresses found in this evaluation of the inverse problem are less than those yielding Figure 5.21 (approximately 5×10^5 psi), they are of the same order of magnitude, and thus fracture is again anticipated as occurring. The time to spontaneous nucleation was estimated as 1.25 msec (Figure 5.21) for the case at hand. The fact that the stress is high enough to generate K_I values sufficient to cause fracture for all times less than this leads to the conclusion that fracture will be instantaneous (i.e., prior to spontaneous nucleation). Thus, no solid shell constraint would exist at the time of spontaneous nucleation.

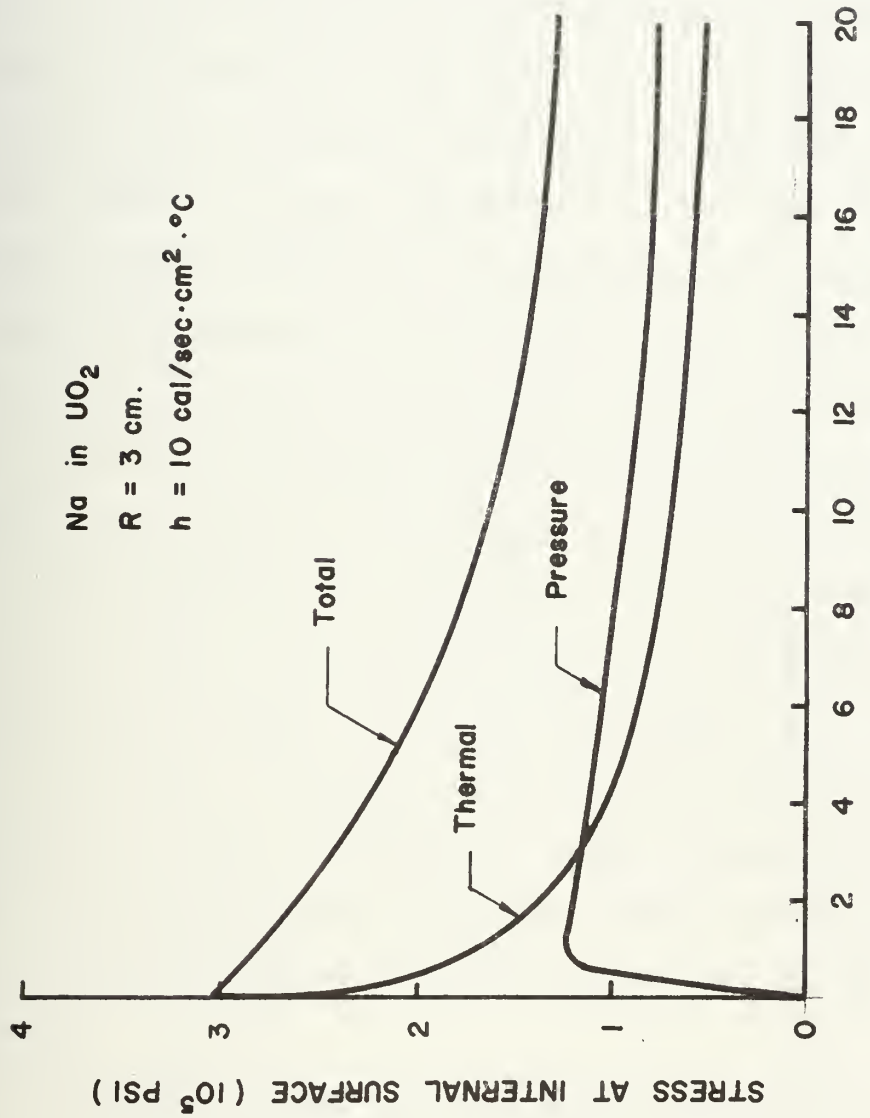

Figure 5.30--Tangential stress variation with time at internal shell surface for Na trapped in UO_2.

Before leaving this subject, it is of interest to make qualitative note of the impact of variation of drop size and/or the heat transfer coefficient. The variation in time to spontaneous nucleation illustrated in Figure 5.25, when the drop size is changed, is relatively small. This leads to the conclusion that small changes in drop size will lead to a minor fluctuation in the time of the occurrence of the spontaneous nucleation in the Na, and will alter the time scale of the stress plot. However, as the induced stresses in the shell are directly related to the temperature difference across the solidifying UO_2, the magnitude of these stresses will not significantly change. When considering variation in the heat transfer coefficient, this is no longer true, as the interface temperature will change. But, as illustrated in Section 5.6, when h is varied, the stress levels are still high enough to result in fracture. Qualitatively then, varying h will alter both the stress level and the time to spontaneous nucleation, but not the outcome of the overall interaction.

In conclusion, based on this basic first-order analysis, it appears reasonable to assume that the only constraint around the Na particle is that provided by the molten and partially solidified (but not contiguous) UO_2. Therefore, the speculation by Fauske (74) that spontaneous

nucleation (due to entrainment, wetting and superheating) leading to a small-mass vapor explosion is the fragmentation mechanism for Na trapped in UO_2 appears to be a plausible description of the interaction.

CHAPTER SIX

THERMAL STRESS FRAGMENTATION IN ALTERNATIVE MATERIAL COMBINATIONS

6.1 Introduction

Qualitatively, experimental results of FCI simulations using Alumina (Al_2O_3) as the hot material interacting with a sodium coolant (126) have shown behavior similar to that observed in UO_2-Na interactions. The interactions were relatively mild and no strong shock waves were observed. Also, the degree of fragmentation of the molten Alumina was extremely high. A secondary experiment done with Alumina shock-cooled in an Argon atmosphere exhibited fragmentation nearly identical to that observed in the Al_2O_3-Na experiments. The similarity of the materials and the resultant interaction lead one to believe that the Al_2O_3-Na simulation is comparable to the actual UO_2-Na interaction. Further, the similarity between the thermally shocked fragmentation residue and that observed in the simulation experiment seem to lend credence to the thermal stress mechanism of fracture under discussion here. Thus, an examination of both the Al_2O_3-Na interaction and that of Al_2O_3 with varying interface temperature was undertaken to assess the applicability of the thermal stress fragmentation model.

Furthermore, due to the extensive experimentation with metal-water simulants, it is desirable to assess the applicability of the thermal stress fragmentation model to such a case. Thus, an analysis of a Tin-H_2O interaction from a thermal stress point of view is included, as well.

6.2 Thermal stress fragmentation of alumina (Al_2O_3)

Initially, the case of alumina dropped into sodium comparable to experimental conditions described by Lazarrus, et al. (127) was considered. A molten Al_2O_3 droplet at its melting point (2040°C) was assumed instantaneously immersed in a pool of sodium at 450°C. Assuming perfect wetting, the contact interface temperature for this case is 1033°C. Based on a fixed surface temperature condition, the subsequently developed stresses at the external surface of the shell are as depicted in Figure 6.1a (excluding density change effects).

The values of K_I developed as the generated crack moves across the shell, for the stress conditions at various times is illustrated in Figure 6.2. The analysis is based on the progressive crack growth model described in the last chapter for UO_2/Na, and it can be seen that the K_I values are substantially larger than the material K_{IC} for Al_2O_3. The value of K_{IC} for Al_2O_3 is based on the experimental analysis of Davidge and Tappin (127) yielding a value for the surface energy at fracture of

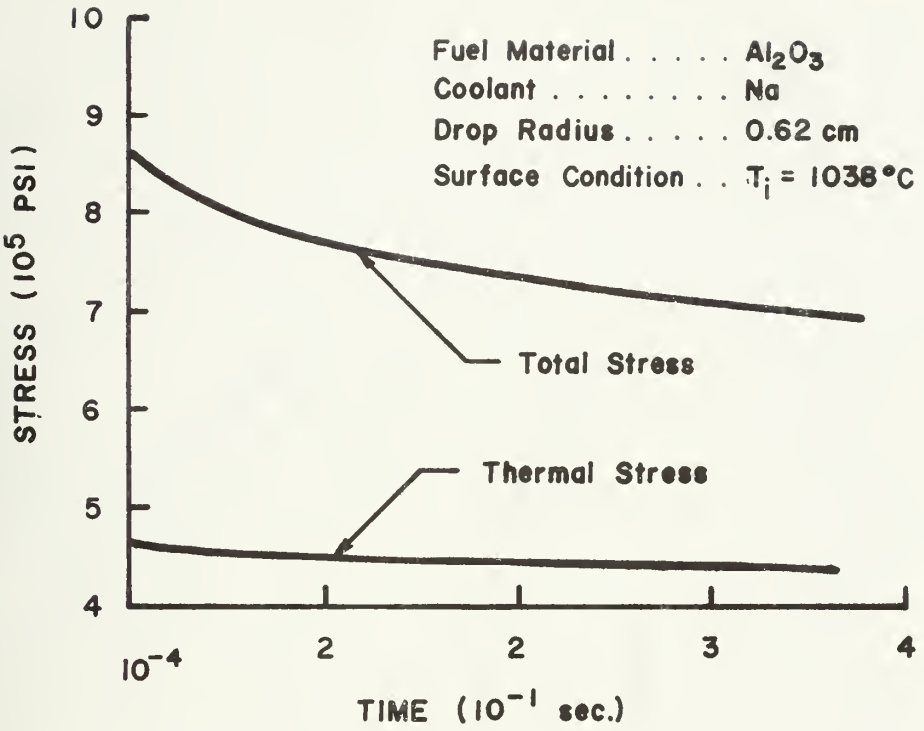

Figure 6.1a--Tangential surface stress for Al_2O_3 with T_I = 1033°C (Al_2O_3/Na interaction).

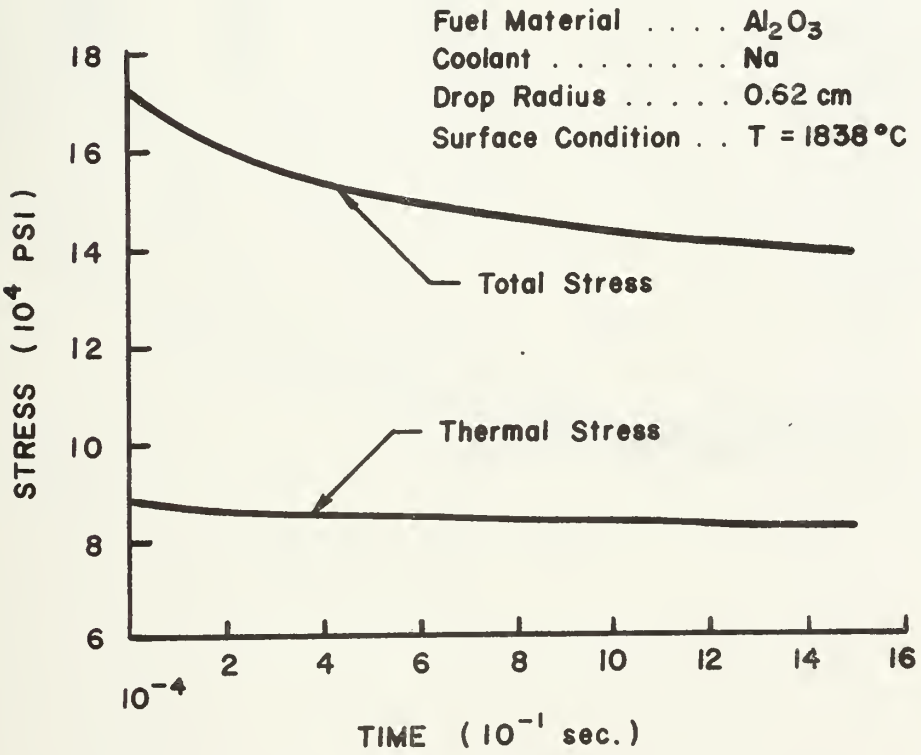

Figure 6.1b--Tangential surface stress for Al_2O_3 with T_I = 1838°C.

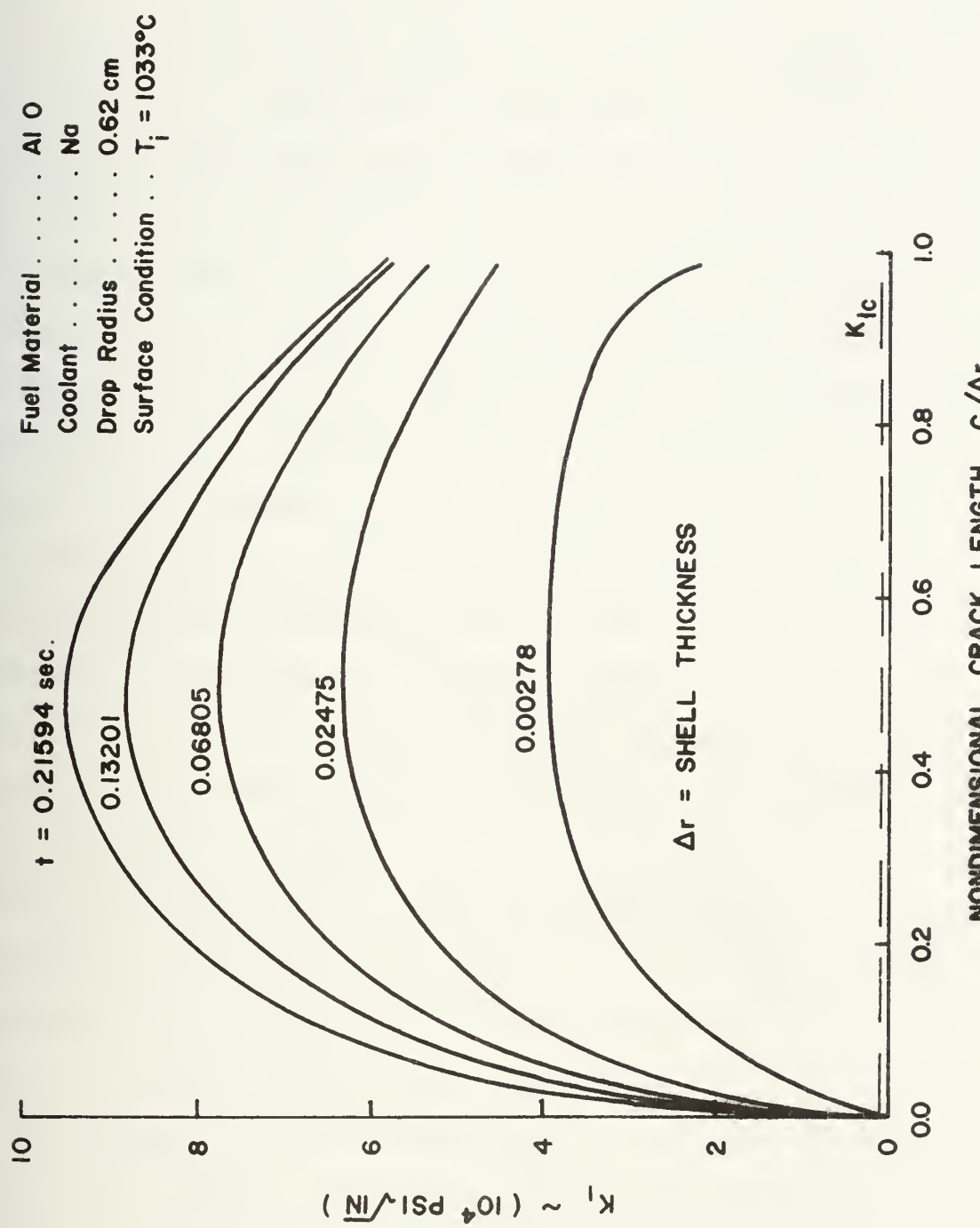

Figure 6.2--Value of K_I for progressive crack growth at various time steps for Al_2O_3 in Na.

γ_I = 6 j/m, and a fracture stress in three point bending of $\sigma_f = 1.595 \times 10^4$ psi for an anticipated flaw size of 100 μm. Utilizing the analysis described in Ref. 110, the mean value of K_{IC} was determined to be 1.5×10^3 psi$\sqrt{in}$.

The generated K_I values based on the total generated stress would lead to almost immediate propagation through the shell, relieving the internal pressure. This fact, coupled with the knowledge that alumina decreases in volume by approximately 20% upon solidification (128), also yielding reduced internal pressures, necessitates an evaluation only considering the thermal stresses. The values of K_I based only on thermal stresses are shown in Figure 6.3. Again, it can be seen that K_{IC} is substantially exceeded. This fact is more easily seen in the expanded view of Figure 6.3. Here, the value of K_{IC} is plotted against the actual, and not the non-dimensionalized, crack depth. The interesting aspect of this figure is that the values of K_I for all times are nearly on top of one another. It is of further significance to note that K_{IC} is exceeded for flaw sizes less than the anticipated 100 μm in all cases. Therefore, if the actual flaw size is around 100 μm, the crack movement can be anticipated as being initiated with an excess of stored energy, leading to a propagation through the shell. Thus, as in the case of UO_2/Na, the thermal stresses alone appear significant enough to result in complete shell failure.

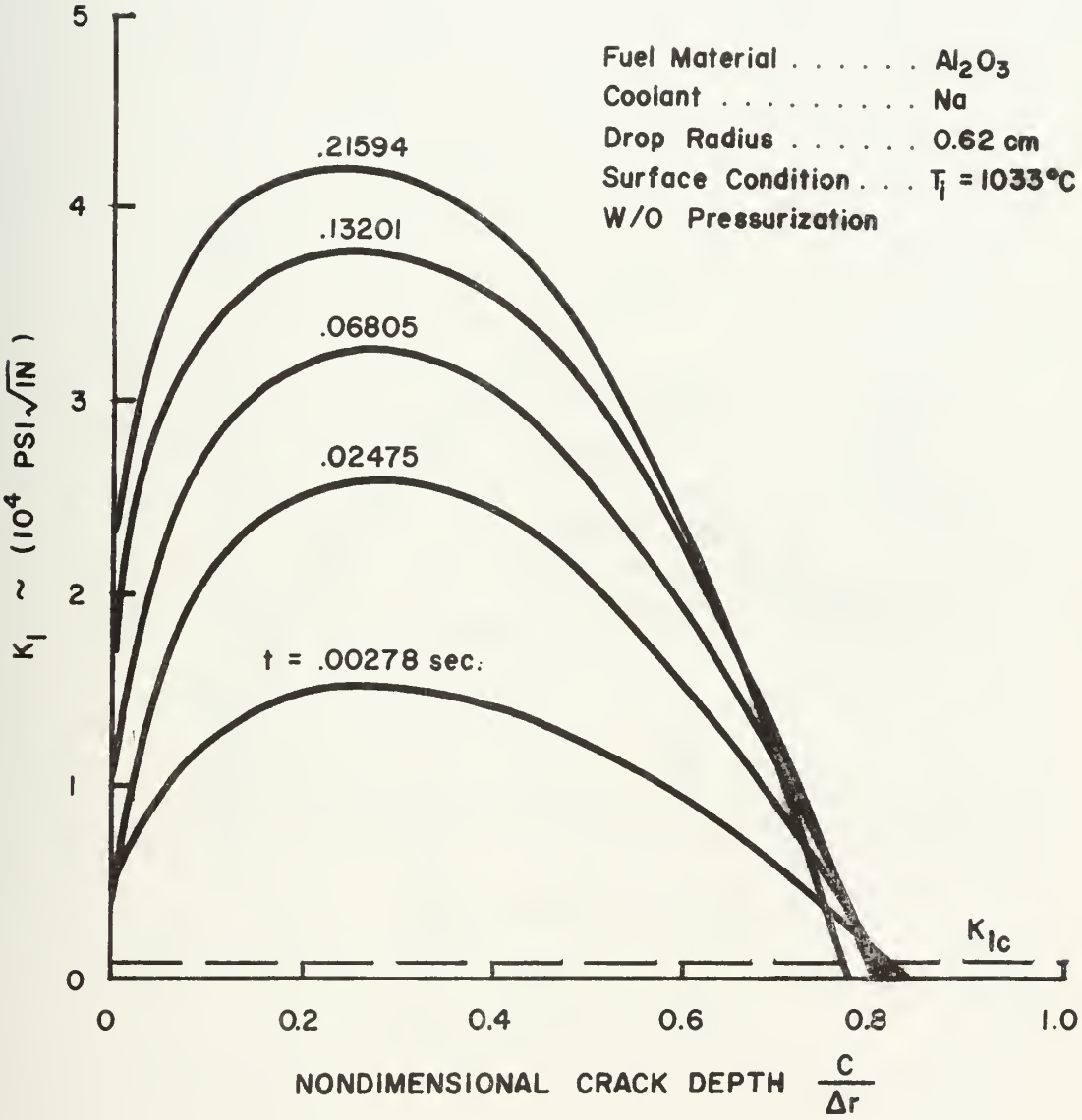

Figure 6.3--Value of K_I for progressive crack growth at various time steps for Al_2O_3 in Na (thermal stress only).

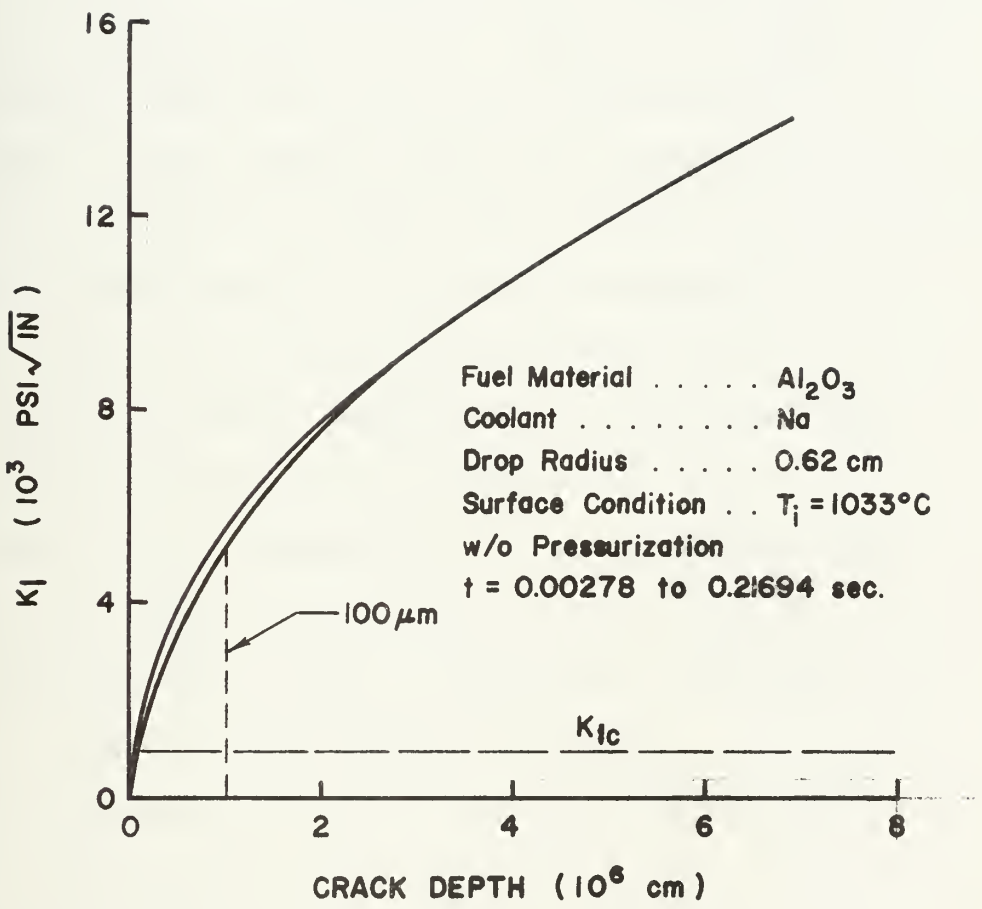

Figure 6.4--K_I versus actual crack depth for $Al_2)_3$ (thermal stress only).

An analysis based on varying the interface temperature to simulate experimental conditions where a varying h occurs at the interface was carried out for Al_2O_3. The results for an interface temperature of 1838°C are illustrated in Figures 6.1b, 6.5-6.7. Again it is seen that flaws greater than 100 μm will be propagated by thermal stresses alone. However, when the interface temperature is increased to 2020°C the required flaw size increases significantly, and greatly exceeds the 100 μm size. This fact is graphically illustrated in Figure 6.8. As the surface temperature will decrease with time, the flaw size required for fracture will also decrease. Thus, as the required flaw size approaches the actual flaw size, fracture will occur. In the case of thermal stress fracture in such a simulation, the delay time will be related to the changing interface temperature rather than the time to develop the shell and generate the stresses (the case for Al_2O_3 in Na). The fracture mechanism, however, will be the same in both cases.

These calculations appear to verify the experimental observations of Ref. 126 and further substantiate the thermal stress mode of fragmentation for brittle ceramic materials. Furthermore, the experimental simulation of the UO_2/Na interaction appears to be well modeled through the use of Al_2O_3.

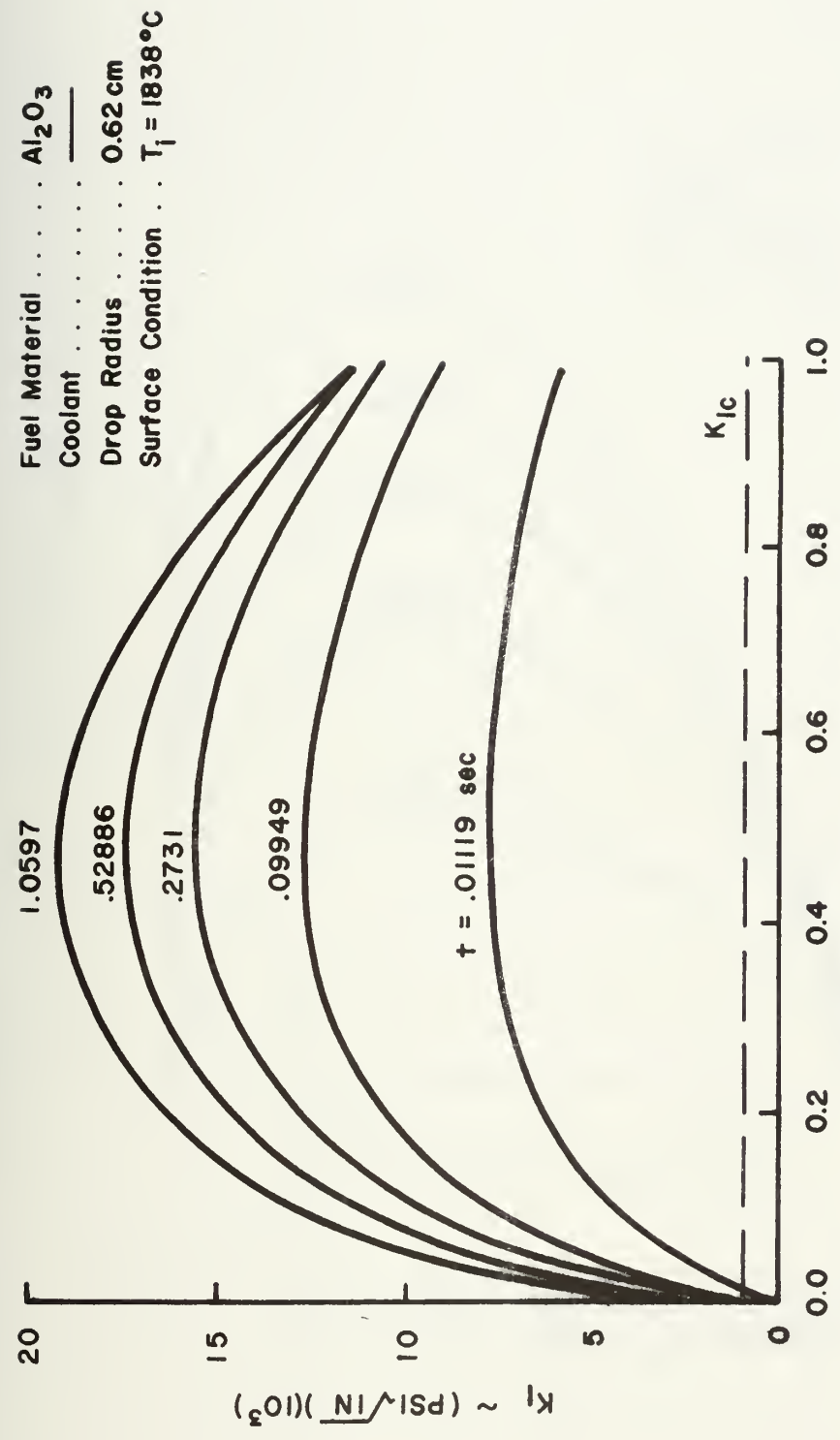

Figure 6.5--Value of K_I for progressive crack growth at various time steps for AL_2O_3 with T_I = 1838°C.

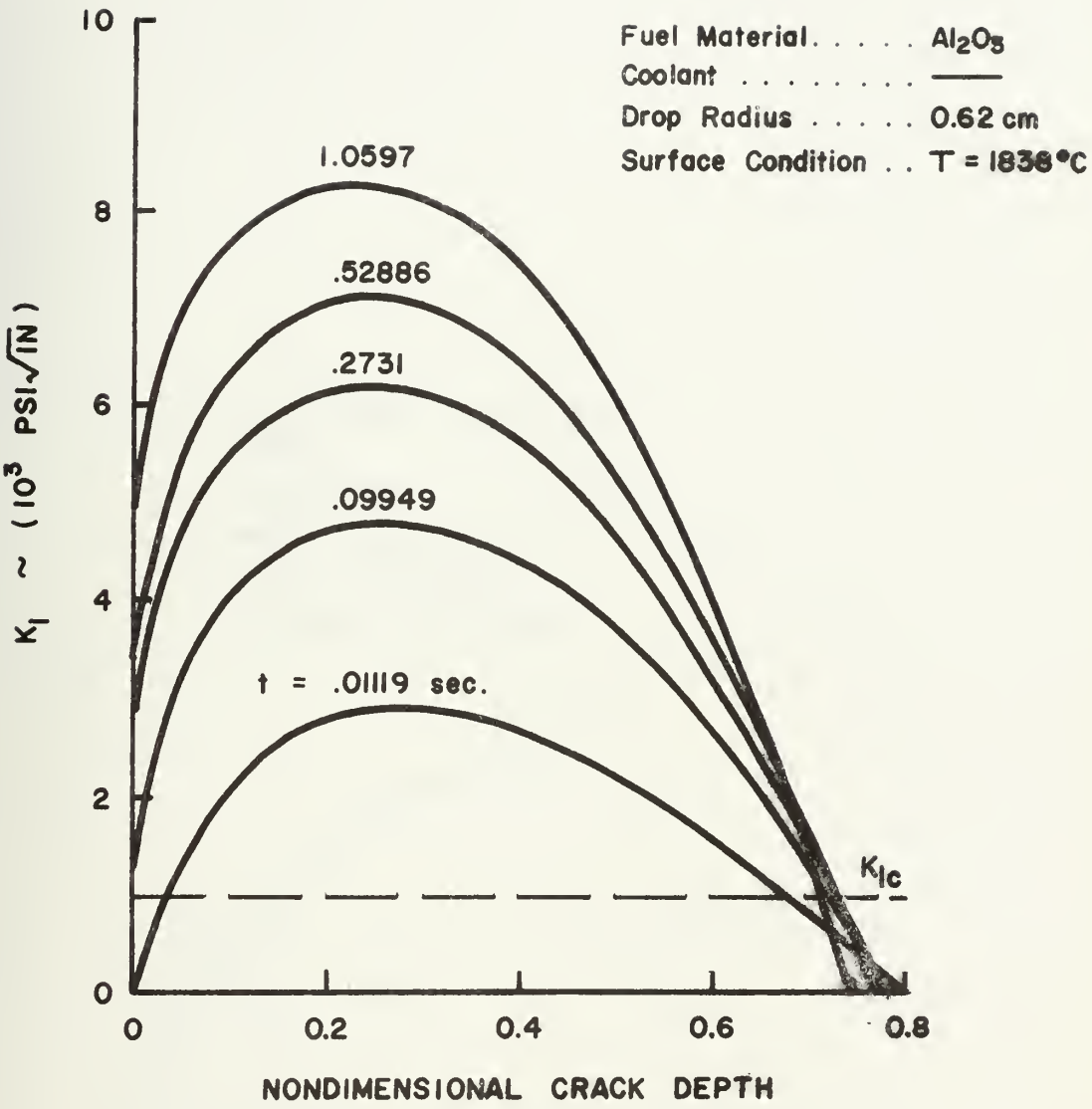

Figure 6.6--Value of K_I for progressive crack growth at various time steps for Al_2O_3 (thermal stress only) for T_I = 1838°C.

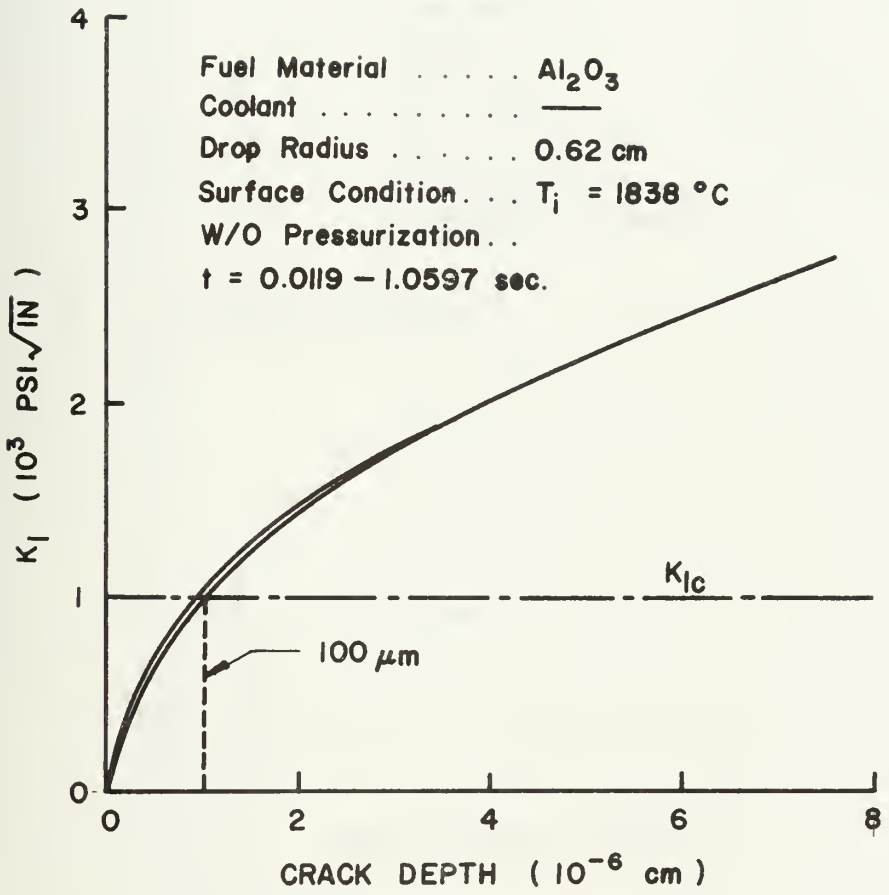

Figure 6.7--K_I versus actual crack depth for AL_2O_3 (thermal stress only) for T_I = 1838°C.

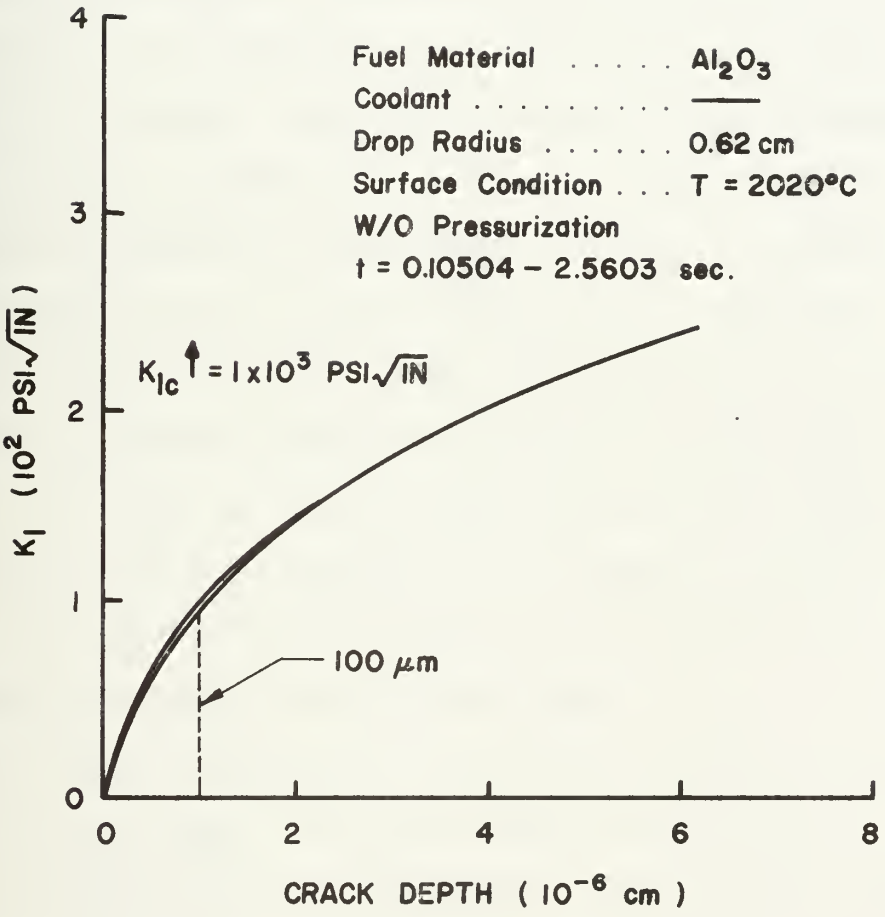

Figure 6.8--K_I versus actual crack depth for Al_2O_3 (thermal stress only) for T_I=2020°C.

6.3 Applicability to the tin/H_2O interaction

The numerous experimental simulations utilizing molten metals dropped into water, many involving tin/H_2O interactions, led to a desire to determine the applicability of the thermal stress fragmentation mechanism to these simulations. It is apparent from the outset that molten metals heated significantly above their melting point would invalidate the solidification phenomenon over the time scale of interest. This would immediately invalidate the thermal stress fragmentation model for many of the existing high temperature experimental results. As well, the extreme ductility of metals such as lead, aluminum, and tin led to some doubt as to the applicability of linear-elastic fracture mechanics and brittle fracture mechanisms. In light of these observations, an estimation of the plastic zone size expected in the case of tin/H_2O (for tin at temperatures not substantially in excess of the melting point; 232°C) was carried out.

In the case of tin/H_2O, the interface temperature is known to vary with time, as in the case of Al_2O_3/argon. Thus, in an attempt to gain some insight into whether the thermal stress fragmentation model was applicable or not, the interface temperature was varied from 200°-100°C, while employing the fixed surface temperature solution. The values of K_I developed in the shell for relatively comparable times based on differing interface temperatures

are illustrated in Figure 6.9. Even though the volumetric reduction upon solidification in tin is only 2.6%, in an effort to make the analysis conservative, the pressurization was neglected and the resulting K_I values are seen in Figure 6.10.

The radius of the plastic zone around the tip of a flaw in the shell can be estimated as (129)

$$r_y = \left(\frac{1}{2\pi}\right)\left(\frac{K_I}{\sigma_y}\right)^2 \qquad (6.1)$$

where σ_y is the tensile yield stress. For tin, a mean value at elevated temperatures of 800 psi was selected for the yield stress (132). Figure 6.11 illustrates the variation of the size of the induced plastic zone with increasing flaw size. It can be seen that in all cases, for flaws less than 10% of the shell thickness in size, the plastic zone diameter exceeds the shell thickness. This percentage rapidly decreases with decreasing interface temperature. For such a case, K_I loses its validity and complete plastic deformation will take place over the tensile zone of the shell (130). Another way of looking at this phenomenon is through the gross approximation that the behavior will be elastic as long as the plastic zone size is on the order of or less than the crack depth. This would only apply to small cracks, as the plastic zone size still must remain significantly smaller than the specimen dimensions. A line representative of this

Fuel Material . . . . . Tin
Coolant . . . . . H_2O
Drop Radius . . . . . 0.3 cm
Surface Condition . . . T_i fixed

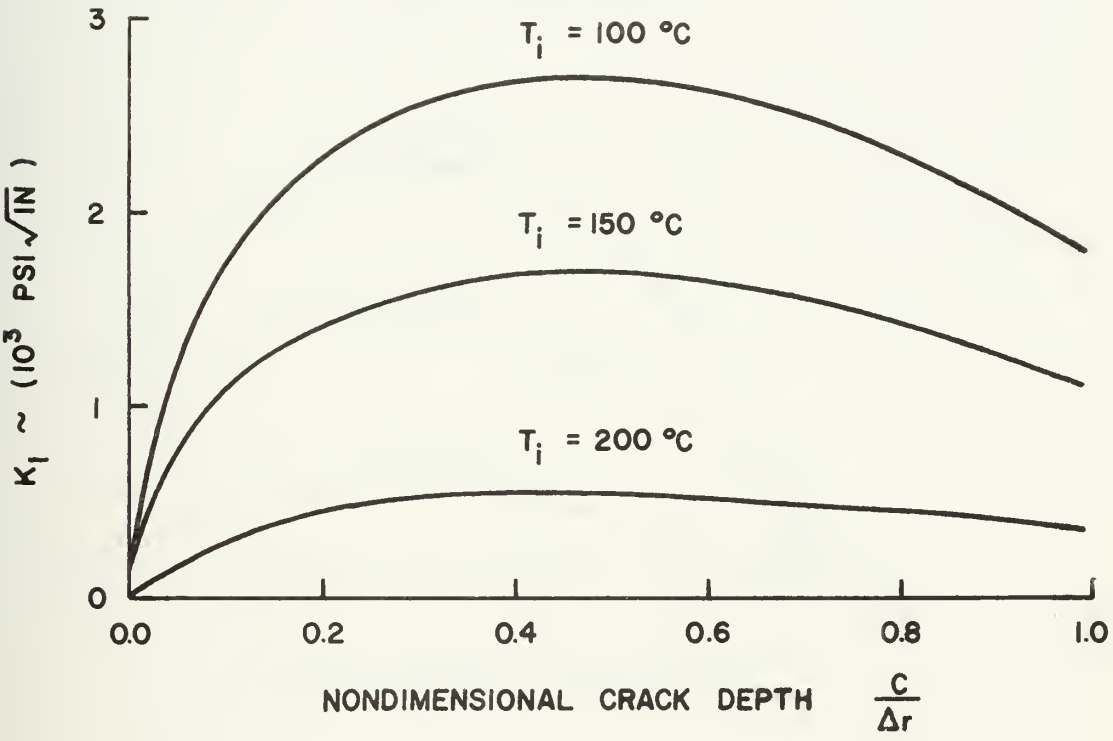

T_i	t	a
200 °C	1.1 msec	0.29 cm
150 °C	1.77 msec	0.28 cm
100 °C	1.15 msec	0.28 cm

Figure 6.9--K_I values for progressive crack growth at various interface temperatures for tin in H_2O.

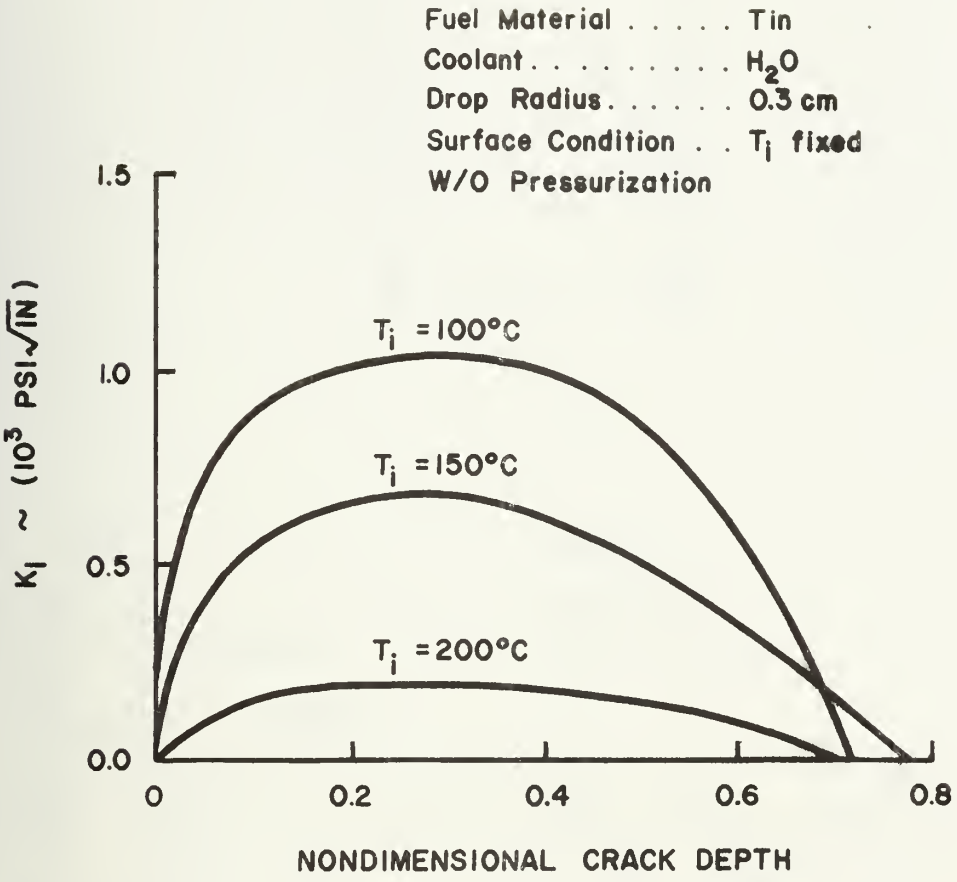

T	t	a
200°C	1.10 msec	0.29 cm
150°C	1.77 msec	0.28 cm
100°C	1.15 msec	0.28 cm

Figure 6.10--K_I values for progressive crack growth at various interface temperatures for tin in H_2O (thermal stress only).

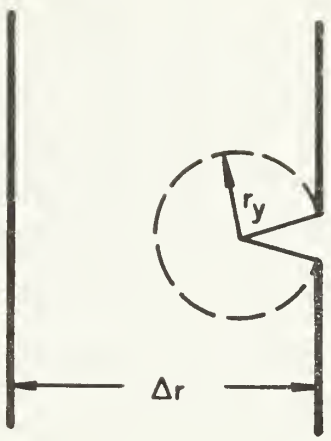

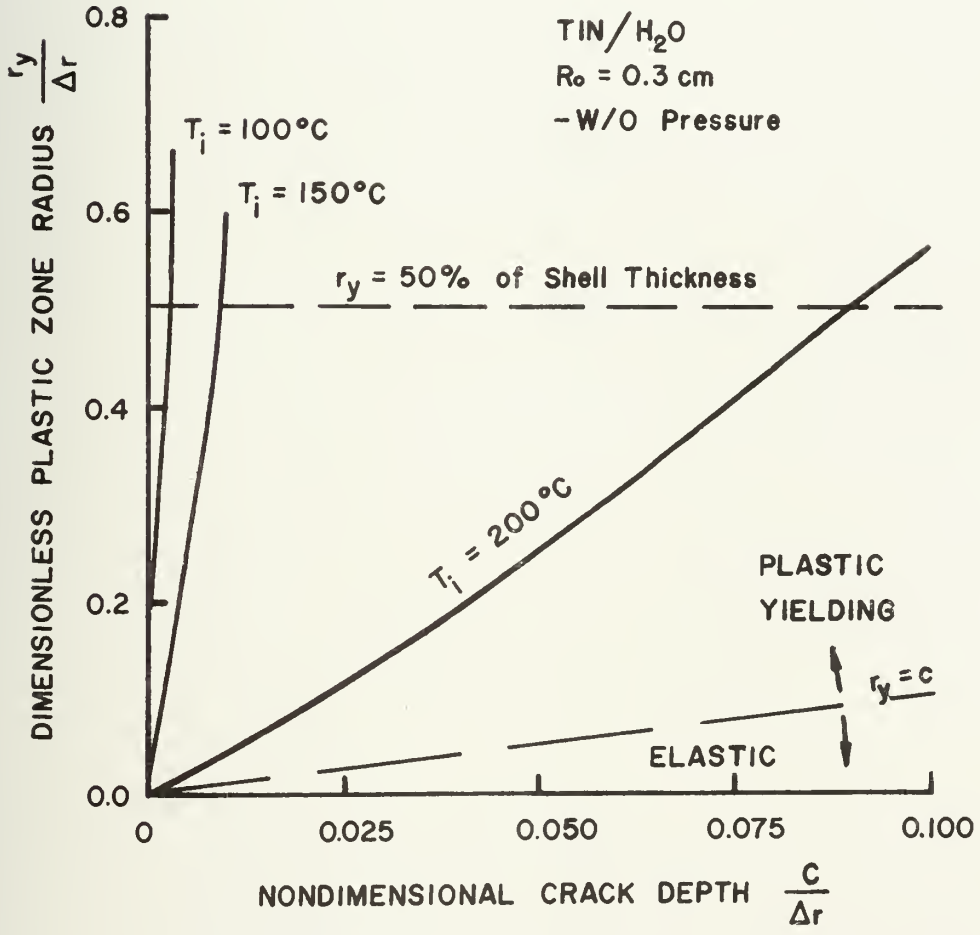

Figure 6.11--Estimation of generated plastic zone size versus crack depth for molten tin in H_2O at various interface temperatures.

criterion is also included in Figure 6.11 for crack depths less than 10% of the shell width. Based on this analysis, the model of thermal stress fracture would not be applicable to ductile materials such as tin, lead, or aluminum, and an alternative mechanism must be considered responsible for the fragmentation in these materials.

CHAPTER SEVEN

CONCLUSION

7.1 Summary

In this analysis, it has been determined that during a UO_2/Na thermal interaction the stresses generated in the solidifying UO_2 are sufficient enough to result in fracturing of the solid shell. This stands then as analytical verification of the original postulations of Cronenberg et al. (77). The value of K_I resulting from the stress field in the shell exceeds the critical fracture toughness, K_{IC}, of UO_2 by such a margin that rapid, instantaneous crack propagation is anticipated. It has been determined that the high initial K_I values will result in the opening of an initial fissure, thereby relieving the internal pressure. In this case, any subsequent fracture would have to be the result of thermal stresses alone. When only considering the thermal stresses, the generated value of K_I was still found to be sufficient to cause fracture initiation. Furthermore, a qualitiative assessment of the crack growth stability led to the determination that even though K_I is driven to zero within the shell, due to the compressive stresses, the dynamic crack growth should be enough to allow propagation through the shell. This would

then allow for multiple cracking from other flaws, even after the initial one relieves the pressure.

If, perchance, the initial pressure-relieving fissure fails to develop, the density change during solidification would cause an internal void to develop within the solidifying droplet, reducing the pressure. The actual pressure level existing within the shell is in some doubt, in this case. It could be as low as the saturation pressure of UO_2 or, if gases have been driven into solution during the initial stages of solidification while the drop is pressurized, it could be some combination of the non-condensable gas pressure and the saturation pressure, as the non-condensables come out of solution during void formation. In any case, during the initial stages of solidification the pressurization is present and the stresses are high enough to result in immediate fracture.

In a separate parametric study, it was found that variation of the surface heat transfer coefficient did not significantly affect the conclusions drawn from the fixed surface temperature solution. The surface heat transfer coefficient was decreased from $h_{nucleate} = h_{boiling}$ (comparable to T_I-constant) and the total stress level was found to increase. This was primarily a result of increased pressures working over a thinner shell, as solidification was retarded, raising the pressure stress. The thermal stress, however, was found to decrease. Thus, initial

fracture under pressurization is more likely. Here again, even with the relief of the internal pressure, the thermal stresses appear significant enough to cause fracture.

In the inverse problem, when small amounts of liquid sodium become entrapped in larger amounts of molten UO_2, it was determined that the total stresses were high enough to result in the fracture of the solidifying UO_2. As a result, the only constraint estimated as existing by the time the trapped sodium has been heated to its spontaneous nucleation temperature is the surrounding partially solidified and molten UO_2. Therefore, the spontaneous nucleation theory, uninhibited by mechanical constraint, appears to be directly applicable in this case.

Extending the analysis to experimental simulants led initially to an investigation of themal stress fracture of Al_2O_3 in sodium. The analysis demonstrated that the behavior of Al_2O_3 was the same as that for UO_2, with fracture imminent under the generated stresses. As well, the volume change on solidification is similar, further verifying comparability. In an effort to ascertain the feasibility of utilizing Al_2O_3 for experimental verification of the thermal stress fragmentation model, the surface temperature was varied to simulate a range considered applicable to a thermal quench. The results indicate that initially, while the surface temperature is still at a high level, solidification will proceed but fracture

will not initiate, as the critical flaw size required is excessive. As the surface cools, however, K_I will increase (decreasing the critical flaw size) and fracture will follow. Even though the perfect wetting and fixed surface temperature conditions which are characteristic in sodium may not be present in this case, the fracture mechanism and fracture behavior of the Al_2O_3 would be similar to that occurring in a sodium quench. The major difference would be the delay time to fracture.

An evaluation of the potential applicability of the thermal stress fragmentation model to metal/water interactions was conducted as well. In this case, a significant factor came to light. That is, that in the case of ductile materials such as lead, tin, and aluminum, the plastic zone size was found to grow to sizes approaching the specimen dimensions for very small flaws, at short times. This results in invalidating the critical stress intensity factor approach, as gross plastic yielding would take place in the tensile zone of the solidifying shell. This fact, coupled with the knowledge that metal/water interactions result in fragmentation even when the molten material temperature is high enough to prevent solidification over the time span of interest, has led to the conclusion that fragmentation in such a system is the result of an alternative mechanism. The validity of the thermal stress fragmentation model is, therefore, limited to semi-brittle

or brittle materials which, for the most part, behave elastically during the interaction process.

The overall conclusion reached is that thermal stress initiated fracture is a viable description of the fragmentation process in the UO_2/Na system. Furthermore, it is concluded that other, easier to handle brittle ceramics, such as Al_2O_3, will sufficiently model the interaction to allow correlation of theory and experiment.

7.2 Recommendations for future work

7.2.1 Experimental

From the standpoint of experimental study, it is highly recommended that a thermal shock-type experiment utilizing Al_2O_3 be carried out. This would allow verification and correlation of experimental and theoretical work. An example of the types of correlations which would be meaningful is illustrated by Figures 7.1 and 7.2. These figures are based on the limited data generated in this study and are not all-inclusive. Figure 7.1 illustrates the variation of K_I with time for various values of the interface temperature, based on the most probable flaw size of 100 μm. Experimental values would be directly obtainable for comparison on such a basis. The interesting aspect of this figure is that it demonstrates the fact that for a specific flaw size, an interface temperature cutoff exists above which fracture would not occur. Eventually, determination and verification of the value of this cutoff

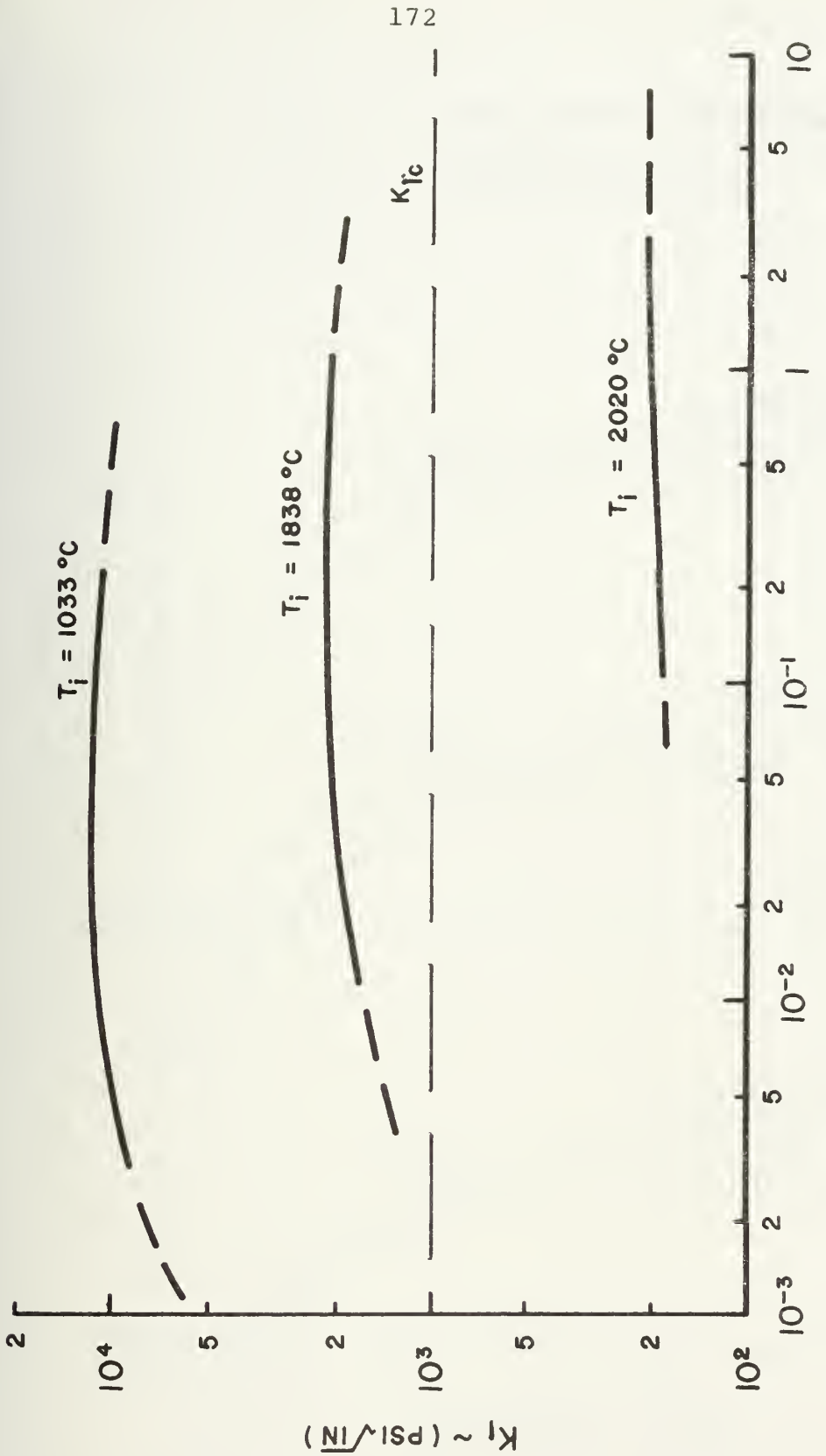

Figure 7.1--K_I versus time at various interface temperatures for a specified flaw size.

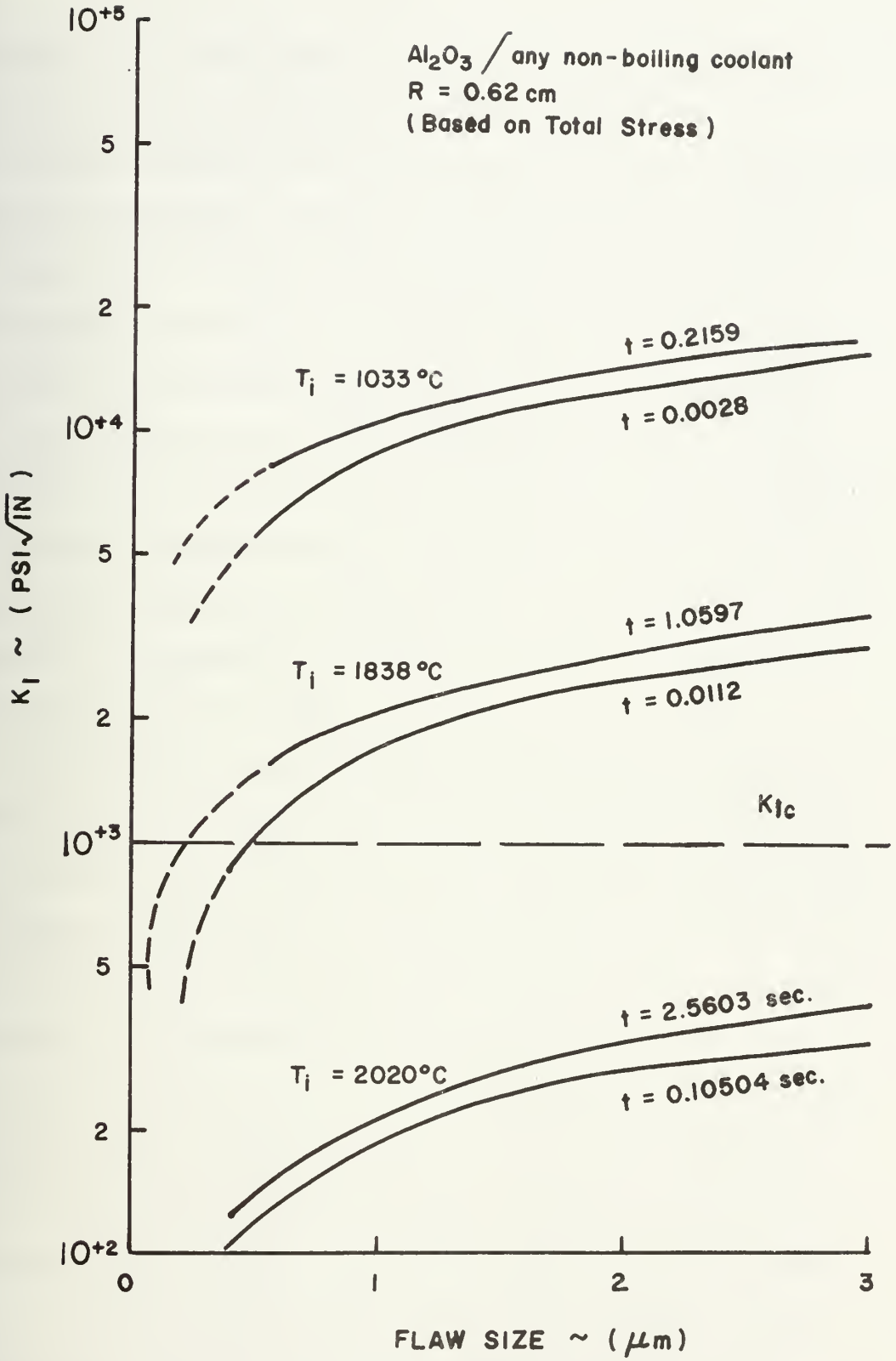

Figure 7.2--K_I versus flaw size at various interface temperatures.

temperature for the UO_2/Na system should be carried out, as it would seem to indicate that if the coolant temperature reached a certain level all further fragmentation would be suppressed. Figure 7.2 provides for a slightly different point of view which is equally applicable to experimental evaluation. In this case, if the time span envelopes are expanded analytically to cover the times from t_{min} (governed by solidification kinetics) to t_{max} (complete solidification), the anticipated time to fracture for various interface temperatures could be predicted and subsequently verified experimentally. Note that the cutoff temperature phenomenon is exhibited in this figure for a 100 μm flaw size, as well.

In evaluating coolant materials for experimental use, it was originally considered desirable to use an inert gas such as argon, as it would help to eliminate complications from second-order effects (such as boiling, in the case of water) while still allowing for "observability". However, in conducting preliminary heat transfer analyses, it was found that the poor heat transfer characteristics of gases required either a tremendously long fall, for dropping experiments, or an extremely high velocity for injection experiments to allow the interface temperature to reach levels capable of generating significant stress levels. Investigation of other feasible materials led to the consideration of molten salt (NaCl). It was found that

for a molten salt coolant at approximately 900°C, the interface temperature would be approximately 1074°C. This value of the interface temperature is sufficient to result in fracture within reasonable times as compared to gases. The adequacy of interface temperatures in this range was demonstrated in the earlier analysis of hte Al_2O_3 interaction and in Figures 7.1 and 7.2. Thus, utilization of a molten salt coolant would appear to provide a reasonable experimental evaluation of the interaction. An experimental verification of this type is considered essential to the final acceptance of the thermal stress fragmentation mechanism.

7.2.2 Analytic confirmation

In parallel with the above experimental work, a verification of the results obtained thus far for Al_2O_3, based on a more streamlined calculation procedure, is desirable. Specifically, a numerical solution, such as that of Tao (134) would be the most useful, as it provides the capability of including various heat transfer coefficients at the surface, if required. Subsequently, further improvements such as including the finite element solution for predicting K_I values would be beneficial. Then, once an accurate prediction of the surface heat transfer condition/coefficient is obtained, theoretical predictions of increased accuracy and reliability would be available for comparative purposes.

It would also be desirable to make a more detailed analytic analysis of the crack growth and stability under the influence of thermal stresses alone, thus making it possible to analytically verify what are at present qualitative observations. Further, the anticipated inherent flaw size and distribution require more accurate definition. This would then allow determination of the number of initiating cracks, and the resultant particle size distribution, with the possibility of further extension to include variation with time.

One other aspect, of higher order, which requires analytical interpretation concerns the actual, nonsymmetric solidification process. The density change, resulting in void formation, will lead to a region in which there are significant temperature and stress field perturbations. The impact of these effects, anticipated as being small, awaits detailed analysis.

These analytical improvements to the thermal stress fragmentation model, as it stands, coupled with the experimental work outlined above would surely provide a strong foundation for the concept, as a whole. The work accomplished to date is only the first step toward this end.

APPENDIX A

MATERIAL PROPERTIES

UO_2

$k = .005$ cal/sec cm°C

$\rho_s = 11$ gm/cm^3

$c_p = .11$ cal/gm°C

$K = 4 \times 10^6$ psi

$E = 26.5 \times 10^6 \left(1. - \frac{0.6T(C)}{2700}\right)$ psi

$\alpha = \left(4.2 + \frac{2.8}{2000} T(F)\right) \times 10^6$ in/in°F

$T_m = 2800$°C

$\nu = .5$

$\rho_\ell = 8.74$ gm/cm^3

$L = 67$ cal/gm

Al_2O_3

$k = .00827$ cal/sec°C

$\rho = 3.98$ gm/cm^3

$c_p = .35$ cal/gm°C

$K = 35.5 \times 10^6$ psi

$E = 40 \times 10^6$ psi

$\alpha = 10.8 \times 10^{-6}$ in/in°C

$T_m = 2040$°C

$\nu = .5$

$L = 256$ cal/gm

Sn

$k = .079$ cal/sec cm°C

$\rho = 7.3$ gm/cm^3

$c_p = .054$ cal/gm°C

$K = 5.88 \times 10^6$ psi

$E = 4 \times 10^6$ psi

$\alpha = 25 \times 10^{-6}$ in/in°C

$T_m = 231.9$°C

$\nu = .5$

$L = 14.5$ cal/gm

Na

$k = .184$ cal/sec cm°C

$\rho = .896$ gm/cm^3

$c_p = 0.30$ cal/gm°C

$T_c = 200 - 450$°C

External B.C.	Shell Sensible Heat	Method	Comment
Fixed Surface Temperature Condition	Included	Adams	Truncated series solution
	Included	Poots	Integral approximation
	Included	Cho & Sunderland	Finite difference solution
	Included	Pederoso & Demoto	Perturbation technique (approx.)
	Included	Tao	Numerical solution
	Not included	London & Seban	Analytical steady-state approx.
Not Specified	Included	Langford	Exact for specified solidification rate

APPENDIX B. Thermal methods for problem of a solidifying sphere.

APPENDIX C

ANALYTIC SOLUTION TECHNIQUE

The purpose of this appendix is to summarize and outline the basic solution technique employed when using the thermal stress fracture model. This, hopefully, will allow future workers to utilize or to extend this model without having to start from the beginning.

The primary tool employed is the computer solution, based on the fixed surface temperature condition, included in this appendix. The thermal solution employed is that of Adams (82) which, through numerical integration, provides the times for successive positions of the solidification front, and the temperature profile in the shell at these times. Subsequently, this information is used as input to equations 3.1-3.3 which are also numerically integrated to yield the induced pressure and stresses within the shell. Note that the pressure here is a result of a balance between the attempted thermal contraction of the shell and the slightly compressible molten UO_2. The primary inputs, variable designation and the output of the program are all included on comment cards in the program listing included herein. Operation of the program is self-explanatory. Figures 5.10-5.12

are illustrative of the type of information obtained from the program. As well, the complete shell stress distribution for a given time is obtained, as seen in Figures 5.18 and 5.19.

For convenience in checking the program, a sample output for 2800°C UO_2 in 200° sodium with the interface temperature at 945°C is included following the program listing in this appendix. This was a run for a solidification front position of .3467 cm and it employed the UO_2 property values given in Appendix A. (Note: ensure that the thermal contraction coefficient value used is converted to "per °C" to be compatible with the rest of the input data.)

Utilization of the stress distribution at various times (e.g., Figure 5.19) and equation 5.17 allow determination of K_I for various crack depths as illustrated in Figures 5.20 (for total stress) and 5.21 (for thermal stress only). A comparison with the material fracture toughness, K_{IC}, then allows determination of whether fracture will occur or not. Finally, an investigation of the point where K_I exceeds K_{IC} for a known flaw size leads to determination of an anticipated delay time to fracture for the material under consideration.

Note that a critical input to this solution is the surface temperature of the molten drop, and a determination of its value must be made prior to initiating any analysis.

There is a provision for varying the surface temperature in the program to allow for parametric evaluations which simulate the surface temperature variation anticipated when a surface heat transfer coefficient exists. This is only good for cursory estimates as were made in this report, as the time rate of variation is a critical factor in any meaningful analysis. Thus, a solution such as that of Tao (134) is recommended when it is known that the fixed surface temperature condition is not applicable.

```
C
C
C     SOLIDIFICATION RATE AND GENERATED STRESSES IN A SPHERICAL MOLTEN DROP.
C
C     INPUT VARIABLES
C     NN=NUMBER OF SOLIDIFICATION FRONT POSITIONS
C     M=NUMBER OF RADIAL POSITIONS ACROSS THE SHELL FOR STRESS CALCS.
C     L=INTEGRATION SUBDIVISICNS (SIMPSON'S RULE)
C     R=OUTSIDE DROP RADIUS
C     ZZ=FINAL POSITION OF SOLIDIFICATION FRONT
C     SPHT=SPECIFIC HEAT OF SOLIDIFYING MATERIAL
C     LM=INTEGRATION SUBDIVISIONS (SIMPSON'S RULE)
C     TS=THERMAL DIFFUSIVITY OF THE SOLIDIFYING MATERIAL
C     SL=LATENT HEAT OF SOLIDIFICATION
C     BULK=BULK MODULUS OF THE FUEL
C     TM=MELTING POINT OF THE FUEL
C     TI=INTERFACE TEMPERATURE
C     ANU=POISSON'S RATIO
C     ALPHA=THERMAL CONTRACTION COEFFICIENT
C     E=YOUNG'S MODULUS
C     THI=HIGHEST INTERFACE TEMPERATURE DESIRED
C     TLOW=LOWEST INTERFACE TEMPERATURE DESIRED
C     MM=NUMBER OF SURFACE TEMPERATURE VALUES USED (INTERFACE)
C
C     THE OUTPUT YIELDS THE STRESS COMPONENTS,AND THE TOTAL STRESS IN
C     BOTH THE RADIAL AND TANGENTIAL DIRECTIONS.  THE TEMPERATURE PROFILE
C     IN THE SHELL IS ALSO INCLUDED.  THE SOLIDIFICATION FRONT, THE TIME
C     TO REACH THAT POSITION AND THE INDUCED PRESSURE ARE ALSO GIVEN.
C
C

      COMMON R,SPHT,TM,TI,SL,TS,DADT,B,TBAR
      DIMENSION A(25),RAD(100)
      EXTERNAL FUNCT,FCT2
      READ(5,100)NN,M,L,R,ZZ,SPHT
      READ(5,200)LM,TS,SL,BULK,TM,ANU
      READ(5,300)MM,THI,TLOW,ALPHA,E
```

```
  100 FORMAT(3I4,3F5.4)
  200 FORMAT(I4,F7.5,F5.0,F10.0,F5.0,F5.4)
  300 FORMAT(I4,2F5.0,F10.7,F10.0)
      TCHG=(THI-TLOW)/FLOAT(MM-1)
      DO 50 II=1,MM
      TI=THI-TCHG*FLOAT(II-1)
      R1=0.0
      R2=R
      ACHG=0.0
      DRAD=0.0
      FIRST=R
      NL=L
      ACHG=(R-ZZ)/FLOAT(NN-1)
      DO 1 I=1,NN
      A(I)=R-ACHG*FLOAT(I-1)
      IF(A(I).EQ.R) GO TO 15
      GO TO 20
   15 WRITE(6,500)
  500 FORMAT(' AT TIME=0.0:  NO INTERFACE MOVEMENT.')
      GO TO 1
   20 END=A(I)
      DADT=1./FUNCT(A(I))
      TIME=SIMPS(FIRST,END,NL,FUNCT)
      NL=NL+2
      B=A(I)
      R1=A(I)
      WRITE(6,1000)
      WRITE(6,2000) TIME,B,DADT
 1000 FORMAT(1H1)
 2000 FORMAT(' TIME=',F10.7,5X,'S-L INTERFACE POSITION=',F5.4,5X,'DADT='
     1,E12.4)
      LL=LM
      DRAD=(R-A(I))/FLOAT(M-1)
      DO 2 J=1,M
      RAD(J)=B+DRAD*FLOAT(J-1)
      R3=RAD(J)
```

```
      AINT1=SIMPS(R1,R2,L,FCT2)
      AINT2=SIMPS(R1,R3,LL,FCT2)
      LL=LL+2
      PC=(6.*ALPHA*E)/(R**3.+2.*A(I)**3.-ANU*(4.*A(I)**3.-R**3.)+((2.*E)
     1/(3.*BULK))*(R**3.-A(I)**3.))
      PPESS=PC*AINT1
      SIGPT=(PRESS*A(I)**3.*(2.*RAD(J)**3.+R**3.))/(2.*RAD(J)**3.*(A(I)*
     1*3.-R**3.))
      SIGPR=(-1.0)*(PRESS*A(I)**3.*(R**3.-RAD(J)**3.))/(RAD(J)**3.*(A(I)
     1**3.-R**3.))
      SIGTT=((2.*ALPHA*E)/(1.0-ANU))*(((2.*RAD(J)**3.+A(I)**3.)/(2.*(R**
     13.-A(I)**3.)*RAD(J)**3.))*AINT1+(1.0/(2.*RAD(J)**3.))*AINT2-.5*TBA
     1R)
      SIGTR=((2.*ALPHA*E)/(1.-ANU))*(((RAD(J)**3.-A(I)**3.)/((R**3.-A(I)
     1**3.)*RAD(J)**3.))*AINT1-(1./RAD(J)**3.)*AINT2)
      TOTT=SIGTT+SIGPT
      TOTR=SIGTR+SIGPR
      TEMP=TBAR+TM
      WRITE(6,3000)R3,PRESS,TBAR,TEMP
      WRITE(6,4000)SIGPT,SIGTT,TOTT
      WRITE(6,5000)SIGPR,SIGTR,TOTR
 3000 FORMAT('0RADIUS=',F8.7,10X,'PRESSURE=',E12.4,5X,'TBAR=',E12.4,5X,'
     1TEMP=',E12.4)
 4000 FORMAT(' SIGPT=',E12.4,3X,'SIGTT=',E12.4,3X,'TOTT=',E12.4)
 5000 FORMAT(' SIGPR=',E12.4,3X,'SIGTR=',E12.4,3X,'TOTR=',E12.4)
    2 CONTINUE
    1 CONTINUE
   50 CONTINUE
      STOP
      END
```

```
      FUNCTION  FUNCT(Y)
      COMMON R,SPHT,TM,TI,SL,TS
      DENOM=2.*TS*SPHT*(TM-TI)
      Z=1.0+((4.*R*SPHT)/(3.*Y*SL))*(TM-TI)
      DENUM=(SL*Y-(SL*Y**2.)/R)*(1.0+SQRT(Z))
      FUNCT=DENUM/DENOM*(-1.0)
      RETURN
      END
```

```
      FUNCTION  FCT2(Y)
      COMMON R,SPHT,TM,TI,SL,TS,DADT,B,TBAR
      GRP1=(SL/(TS*SPHT))*((R-Y)/(R*Y))*B**2.*DADT
      GRP2=B*DADT**2*SL/SPHT*((1.0/TS)**2.)*((R-Y)/(R-B))*(R/3.-Y/6.-B**
     12./(2.*Y)+B**3./(3.*R*Y))
      TBAR=TI-GRP1+GRP2-TM
      FCT2=TBAR*Y**2.
      RETURN
      END
```

```
      FUNCTION  SIMPS(D,E,N,F)
      TWOH=(E-D)/FLOAT(N)
      H=TWOH/2.
      SUMED=0.0
      SUMID=0.0
      DO 10 K=1,N
      X=D+FLOAT(K-1)*TWOH
      SUMED=SUMED+F(X)
      SUMID=SUMID+F(X+H)
   10 CONTINUE
      SIMPS=(2.0*SUMED+4.0*SUMID-F(D)+F(E))*H/3.
      RETURN
      END
C
C     PLACE DATA CARDS CORRESPONDING TO STATEMENT NUMBERS 100-300
C     HERE UTILIZING THE SPECIFIED FORMAT.
C
```

```
TIME= 0.0116435      S-L INTERFACE POSITION=.3467     DADT= -0.5778E 00

RADIUS=.3466666          PRESSURE= -0.2456E 05     TBAR= 0.1809E 00     TEMP=  0.2800E 04
SIGPT=  0.3195E 06    SIGTT= -0.4044E 06   TOTT= -0.8488E 05
SIGPR= -0.2456E 05    SIGTR=  0.0          TOTR= -0.2456E 05

RADIUS=.3500000          PRESSURE= -0.2456E 05     TBAR= -0.3541E 03    TEMP=  0.2446E 04
SIGPT=  0.3163E 06    SIGTT= -0.2345E 06   TOTT=  0.8181E 05
SIGPR= -0.1806E 05    SIGTR= -0.6137E 04   TOTR= -0.2420E 05

RADIUS=.3533333          PRESSURE= -0.2456E 05     TBAR= -0.8062E 03    TEMP=  0.1994E 04
SIGPT=  0.3132E 06    SIGTT= -0.2034E 05   TOTT=  0.2928E 06
SIGPR= -0.1181E 05    SIGTR= -0.8464E 04   TOTR= -0.2028E 05

RADIUS=.3566666          PRESSURE= -0.2456E 05     TBAR= -0.1318E 04    TEMP=  0.1482E 04
SIGPT=  0.3102E 06    SIGTT=  0.2199E 06   TOTT=  0.5301E 06
SIGPR= -0.5797E 04    SIGTR= -0.6474E 04   TOTR= -0.1227E 05

RADIUS=.3600000          PRESSURE= -0.2456E 05     TBAR= -0.1855E 04    TEMP=  0.9450E 03
SIGPT=  0.3073E 06    SIGTT=  0.4694E 06   TOTT=  0.7767E 06
SIGPR=  0.0           SIGTR=  0.7187E-01   TOTR=  0.7187E-01
```

REFERENCES

1. Teague, H. J., "Summary of the Papers Presented at the CREST Meeting on Fuel-Sodium Interaction at Grenoble in January 1972 and Report on Conference Papers 38 a-k on Fuel-Sodium Interactions", Presented at Int. Conf. Engineering of Fast Reactors for Safe and Reliable Operation, Karlsruhe, Oct. 1972.

2. Caldarola, L., "Current Status of Knowledge of Molten Fuel/Sodium Thermal Interactions," Presented at meeting of "Safety Working Group" (Coordinating Committee for Fast Reactors), Brussels, Feb. 1974.

3. Fauske, H. K., "A Review of the November 1973 CSNI Specialist Meeting on FCI, ANL.

4. Percy, J., Metallurgy, p. 625, J. Murray, London, 1864.

5. Lipsett, S. G., "Explosions From Molten Materials and Water," Free Technology 2, 118-126, May 1966.

6. Long, G., "Explosion of Molten Aluminum in Water--Cause and Prevention," Metal Progress 71, 107-112, May 1957.

7. Thompson, T. J., "Accidents and Destructive Tests," in The Technology of Nuclear Reactor Safety, Vol. 1, T. J. Thompson and J. G. Becknley (ed.), MIT Press, Cambridge, MA, 1964.

8. Dietrich, "Experimental Determination of the Self-Regulating and Safety of Operating Water-Moderated Reactors," Proc. Int. Conf. on Peaceful Uses of Atomic Energy, Vol. 13, 88-101, 1955.

9. Kittel, J. H., et al., "The EBR-I Meltdown, Physical and Metallurgical Changes in the Core", Nucl. Sci. Eng. 4, 180-199, 1958.

10. "Final Report of SL-1 Recovery Operation", IDO-19311, July 1962.

11. Eglert, J. O., and Brown, A. W., "In-Pile Molten-Metal Water Reactions," IDO-16257, June 1956.

12. Epstein, E. F., "Metal Water Reactions: VI Analytical Formulation for the Reaction Rate," GEAP-3272, Sept. 1959.

13. Hess, P. D., and Brandyke, K. J., "Molten Aluminum Water Explosions," Metal Progress, 93-100, April 1969.

14. Kazimi, M. S., "Theoretical Studies of Some Aspects of Molten Fuel-Coolant Thermal Interaction," Sc.D. Thesis, Nucl. Eng. Dept., MIT, Cambridge, MA, May 1973.

15. Armstrong, D., and Cho, D., "LMFBR Nuclear Safety Program Annual Report," ANL-7800, 340-358, July 1971.

16. Swift, D., and Paulik, J., "Chemical Engineering Division Semiannual Report, July-December 1965, ANL-7125, 187-193, May 1966.

17. "Reactor Development Program Progress Report, January 1966," ANL-71-52, 90-96, Feb. 1966.

18. "Core Design Developments Needs in Relation to Fuel Failure Propagation, Sodium Boding and Clad/Fuel-Sodium Thermal Interaction," GEAP-13639-2, 770-4, Oct. 1970.

19. Ambland, M., et al., "Contact Effects Between Molten UO_2 and Sodium and Molten UO_2 and Water," EURFNR-811, March 1970.

20. Armstrong, D. R., Testa, F. J., and Rariden, D., "Molten UO_2-Sodium Dropping Experiments," Trans. Amer. Nucl. Soc. 13, 660, 1970.

21. Westwater, J. W., Advances in Chemical Engineering, Vol. 1, Academic Press, New York, 1957.

22. Ivins, R. O., "Reactor Development Program Progress Report, Nov. 1967," ANL-7399, 162-165, Dec. 1967.

23. Hinze, J. O., "Fundamentals of the Hydrodynamic Mechanism of Splitting in Dispersion Processes," A.I.Ch.E. Journal 1, 3, pp 289-295, Sept. 1955.

24. Brauer, F. E., et al., "Metal/Water Explosions," Nucl. Sci. Eng., 31, 551-4, March 1968.

25. Flory, K., et al., "Molten Metal-Water Explosions," Chem. Eng. Progress 65, 50-54, Dec. 1969.

26. Sallack, J. A., "On Investigation of Explosions in the Soda Smelt Dissolving Operation," Canadian Pulp and Paper Association Meeting, Quebec, Canada, June 6-8, 1955.

27. Gronveld, P., "Explosive Vapor Formation," Trans. ASME, J. of Heat Transfer, 236-8, May 1972.

28. Witte, L. C., et al., "Rapid Quenching of Molten Metals," ORO-3936-6, August 1971.

29. Bradley, R. H. et al., "Investigation of the Vapor Explosion Phenomena Using a Molten-Metal Jet Injection Into Distilled Water," ORO-3936-7, Oct. 1971.

30. Stevens, J. W., et al., "Transient Film and Transition Boiling From a Sphere," ORO-3936-9, September 1972.

31. Board, S. J., et al., "Fragmentation in Thermal Explosions," Central Electricity Generating Board Report RD/B/N2423, Oct. 1972.

31a. Witte, L. C., Cox, J. E., Gelabert, A. A., and Vyas, T. J., "The Vapor Explosion--Heat Transfer and Fragmentation IV. Rapid Quenching of Molten Metal," University of Houston Technical Report No. ORO-3936-6, August 1971.

32. Anderson, R., and Armstrong, D., "Laboratory Tests of Molten-Fuel-Coolant Interactions," Trans. Am. Nucl. Soc., 15 (1), p. 313, June 1972.

33. Fauske, H. K., "The Role of Nucleation in Vapor Explosions," Trans. Am. Nucl. Soc., 15 (2), p. 813, Nov. 1972.

34. Zivi, S. M. et al., "Kinetic Studies of Heterogenous Water Reactors," Annual Summary Report 1963, STL-6312, 5-49; Annual Summary Report 1964, STL-372-13, 5-44; Annual Summary Report 1965, STL-372-30, 7-23.

35. Wright, R. W., "Pressure Pulses in Rapid Transient Boiling," Trans. Am. Nucl. Suc. 6 (2), p. 338, Nov. 1963.

36. Wright, R. W., "Kinetic Studies of Heterogeneous Water Reactors, Annual Summary Report 1965," STL-372-30, TRW Systems, Dec. 1965 and "Annual

37. Liimatainen, R. C., and Testa, F. J., "Chemical Engineering Division Semiannual Report, July-December 1965," ANL-7125, 120-178, May 1966.

38. Miller, R. W., and Lussie, W. G., "Power Bursts in Zircaloy-2 Clad Oxide Fuel Rods," Trans. Am. Nucl. Soc. 12 (1), 344-6, 1969.

39. Martinson, Z. R., "Behavior of 5-Inch Long, 1/4-Inch OD, Zircaloy-2 Clad Oxide Fuel Rods Subjected to High Energy Power Bursts," IN-ITR-107, August 1969.

40. Dickerman, "Studies of Fast Reactor Core Behavior Under Accident Conditions," Nuclear Safety II, 195-205, May-June 1970.

41. Barghusen, J. J., et al., "LMFBR Nuclear Safety Program Annual Report," ANL-7800, 321-339, July 1971.

42. Wright, R. W. et al., "Reactor Development Program Progress Report, June 1971," ANL-7833, p. 8.23, July 1971.

43. Wright, R. W. et al., "Reactor Development Program Progress Report, August 1971," ANL-7854, 8.19-8.21, September 1971.

44. Barghusen, J. J., "Reactor Development Program Progress Report, March 1972," ANL-RDP-3, 8.34-8.38, April 1972.

45. Dickerman, C. E. et al., "Fuel Dynamics Experiments On Fast Reactor Oxide Fuel Performance Under Transient Heating Conditions Using the TREAT Reactor," Trans. Am. Nucl. Soc. Supplement No. 1 to Volume 14, p. 28, April 1971.

46. Wright, R. W. et al., "Summary of Autoclave TREAT Tests on Molten-Fuel-Coolant Interactions," Presented at the ANS Topical Meeting on Fast Reactor Safety, Beverly Hills, April 1974.

47. Epstein, M., and Cho, D. H., "Fuel Vaporization and Quenching by Cold Sodium; Interpretation of TREAT Test S-11," Presented at the ANS Topical Meeting on Fast Reactor Safety, Beverly Hills, April 1974.

48. Speis, T. P., and Fauske, H. K., "UO_2/Na Interactions--Recent In- and Out-of-Pile Experimenta in the U.S. and Their Interpretation for Fast Reactor Safety Analysis," Presented at the Second Specialist Meeting on Sodium Fuel Interactions in Fast Reactors, Ispra, Italy, November 21-23, 1973.

49. Hicks, E. P., and Menzies, D. C., "Theoretical Studies On the Fast Reactor Maximum Accidents," in Proc. Conf. Safety, Fuels and Core Design in Large Fast Power Reactors, ANL-7120, October 1965.

50. Johnson, T. R., Baker, L., Jr., and Paulik, J. R., "Large-Scale Molten UO_2-Sodium Interaction Experiments," Presented at the ANS Topical Meeting on Fast Reactor Safety, Beverly Hills, April 1974.

51. Klickman, A. E., "Summary of Energy Release Analyses of the Hypothetical Meltdown Design Accident for Core A of the Enrico Fermi Reactor," APDA-LA-7, July 1969.

52. Judd, A. M., "Calculation of the Thermodynamic Efficiency of Molten-Fuel-Coolant Interactions," Trans. Am. Nucl. Soc. 13 (1), p. 369, 1970.

53. Padiller, A., "Analysis of Mechanical Work Energy for LMFBR Maximum Accidents," Nucl. Technology 12, No. 4, p. 348-355, December 1971.

54. Pfefferlen, H., "Analytical Evaluation of the Consequences of a Hypothetical Instantaneous Loss of Coolant Flow to a Fast Flux Test Facility Driven Fuel Assembly," Compiled by L. M. McWethy, GEAP-10059, July 1969.

55. Biasi, L. C. et al., "Heat Transfer and Fluid Dynamics of Fuel-Sodium Interaction," Paper presented at the International Center for Heat and Mass Transfer, Trogian, Yugoslavia, September 1971.

56. Padilla, A., "Transient Analysis of Fuel-Sodium Interaction," Trans. Am. Nucl. Soc. 13 (1), p. 375, 1970.

57. Cho, D. et al, "Pressure Generation by Molten Fuel-Coolant Interactions Under LMFBR Accident Conditions," Proc. Conf. New Developments in Reactor Mathematics and Applications, Idaho Falls, Idaho, March 1971, Conf-710302.

58. Cho, D. et al., "Effects of Gas/Vapor Blanketing on Pressure Pulses and Mechanical Work Produced by Molten Fuel-Coolant Interactions," Trans. Am. Nucl. Soc. 15 (1), p. 314, 1972.

59. Reynolds, A. B.; Erdman, C. H.; Garner, P. L.; Haas, P. M.; and Allen, C. L., "Evaluation of Conservatism in the Analysis of Fuel/Coolant Interactions," Paper presented at the CREST second specialist meeting on Sodium Fuel Interaction in Fast Reactors, Ispra, Italy, November 21-23, 1973.

60. Caldarola, L., and Koutsoundis, G., "The Karlsruhe Variable Mass Model for the Description of the Fuel-Coolant Interaction," Paper presented at the CREST second specialist meeting on Sodium Fuel Interaction in Fast Reactors, Ispra, Italy, November 21-23, 1973.

61. Grossgut, W.; Kottowski, H. M.; Holtbecker, H.; and Randles, J., "On the Process of Thermal Interactions Between Molten Fuel and Coolant."

62. Carelli, M. D., "Fission Gas and Molten Fuel Ejection From Failed Fuel Rods in an LMFBR," Proc. Conf. New Developments in Reactor Mathematics and Applications, Idaho Falls, Idaho, March 1971.

63. Lorenzini, P. G., and Flanagan, G. F., "An Evaluation of Fuel-Coolant Interactions During Disassembly of an LMFBR," Proc. Conf. New Developments in Reactor Mathematics and Applications, Idaho Falls, Idaho, March 1971.

64. Smith, L. L. et al., "SAS/FCI: A Fuel-Coolant Interaction Model for LMFBR Whole-Core Accident Analysis," ANS Topical Meeting on Mathematical Models and Computational Techniques for Analysis of Nuclear Systems," Ann Arbor, Michigan, April 1973.

65. Annenberg, A. W., and Grolmes, M. A., "A Review of Fragmentation Models Relative to Molten UO_2 Breakup when Quenched in Sodium Coolant," Paper Presented at 1974 ASME Winter Meeting, New York, November 17-21, 1974.

66. Paoli, R. M., and Mesler, R. B., "Explosion of Molten Lead in Water," Proc. of the 8th International Conf. on High-Speed Photography, John Wiley and Sons, 1968.

67. Hewitt, G. F., and Hall-Taylor, N., "Interfacial Waves,"Ch. 6, Annular Two-Phase Flow, Pergamon Press, 1970.

68. Swift, D., and Baker, L., Reactor Development Program Progress Report, ANL-7152, p. 87-96, January 1965.

69. Cronenberg, A. W., "A Thermohydrodynamic Model for Molten UO_2-Na Interaction, Pertaining to Fast-Reactor Fuel-Failure Accidents," App. A, ANL-7947, 1972.

70. Caldarola, L., and Kastenberg, W. E., "On the Mechanism of Fragmentation during Molten Fuel-Coolant Thermal Interactions," Proc. of ANS Conf. on Fast Reactor Safety, Los Angeles, 1974.

71. Benjamin, T. B., and Ellis, A. T., "The Collapse of Cavitation Bubbles and the Pressure Thereby Produced Against Solid Boundaries," Phil. Trans. Royal Soc., A260, p. 221, 1966.

72. Fauske, H. K., "The Role of Nucleation in Vapor Explosions," Trans. Am. Nucl. Soc. 15 (2), p. 813, November 1972.

73. Fauske, H. K., "On the Mechanism of UO_2-Na Explosive Interactions," Nucl. Sci. and Eng., Vol. 51, p. 95-101, 1973.

74. Fauske, H. K., "Some Aspects of Liquid-Liquid Heat Transfer and Explosive Boiling," presented at the Fast Reactor Safety Conference, Beverly Hills, Calif., April 2-4, 1974.

75. Epstein, M., "Thermal Fragmentation: A Gas Release Phenomenon," Reactor Development Progress Report for February 1974, 1974.

76. Hsiao, K. H. et al., "Pressurization of a Solidifying Sphere," J. of Applied Mech., Vol. 39, p. 71-77, March 1972.

77. Cronenberg, A. W., Chawla, T. C., and Fauske, H. K., "A Thermal Stress Mechanism for the Fragmentation of Molten UO_2 Upon Contact with Sodium Coolant," Nucl. Eng. and Design.

78. Cronenberg, A. W., and Fauske, H. K., "UO_2 Solidification Phenomena Associated with Rapid Cooling in Liquid Sodium," J. of Nucl. Materials.

79. Cronenberg, A. W., and Fauske, H. K., "UO_2 Solidification Phenomena and Fragmentation During Quenching in Sodium Coolant," Trans. Am. Nucl. Soc., Vol. 16, 1973.

80. London, A. L., and Seban, R. H., "Rate of Ice Formation," Transactions ASME, 65, 1943.

81. Stowell, Z. E., "A Phenominological Relation Between Stresses, Strain Rate, and Temperature for Metals at Elevated Temperatures," NACA Technical Note 4000, May 1957.

82. Adams, C. M., "Thermal Considerations in Freezing, in Liquid Metals and Solidification," American Society for Metals, Cleveland, 1958.

83. Carslaw, H. S., and Jeager, J. C., Conduction of Heat in Solids, Oxford, 1959.

84. Nowinski, J., "Thermoelastic Problem for an Isotropic Sphere with Temperature-Dependent Properties," ZAMP, 10, 1959.

85. Kent, C. W., "Thermal Stresses in Spheres and Cylinders Produced by Temperatures Varying with Time," Transactions ASME, APM-54-18, 1932.

86. Henry, R. E., "A Correlation for the Minimum Film Boiling Temperature," Proc. of AIChE Heat Transfer Conference, Atlanta, 1973.

87. Griffith, A. A., "Phenomena of Rupture and Flow in Solids," Philosophical Transactions of the Royal Society, Vol. A221, p. 163, 1920.

88. Tettleman, A. S., and McErily, A. J., Fracture of Structural Materials, John Wiley and Sons, New York, 1967.

89. Berry, J. P., "Equations of Motion of Griffith Crack at Constant Force," Journal of Mech. Phys. Solids, Vol. 8, p. 194, 1960.

90. Sack, R. A., "Extension of Griffiths Theory of Rupture to Three Dimensions," Proc. Physical Society of London, Vol. 58, p. 729, 1946.

91. Sneddon, I. N., "The Distribution of Stress in the Neighborhood of a Crack in an Elastic Solid," Proc. Royal Soc., Vol. A187, p. 229, 1946.

92. Roberts, D. K. et al., "The Velocity of Brittle Fracture," Engineering, Vol. 178, p. 820, 1954.

93. Yoffee, E. H., "The Moving Griffith Crack," Phil. Mag. Vol. 42, p. 739, 1951.

94. Nakayama, J., "Direct Measurements of Fracture Energies of Brittle Heterogeneous Materials," Journal of the American Ceramic Society, Vol. 48, No. 11, p. 584.

95. Broberg, K. B., "The Propagation of a Brittle Crack," Arkin for Fysik, Vol. 18, No. 10, p. 159, 1960.

96. Mott, N. F., "Brittle Fracture in Mild Steel Plates," Engineering, Vol. 165, p. 16, 1948.

97. Schardin, H., "Fracture of Glass," Ceramic Abstracts, Vol. 20, No. 8, p. 191, 1941.

98. Schardin, H., "Velocity Effects in Fracture," Fracture, Proc. Int. Conf., MIT Press, p. 297, April 1959.

99. Shand, E. B., "Experimental Study of Fracture of Glass," Journal American Ceramic Society, Vol. 37, No. 12, p. 559, 1954.

100. Irwin, G. R., "Fracture Mechanics," Structural Mechanics, (Naval Symposium), Pergamon Press, 1960.

101. Irwin, G. R., "Analysis of Stresses and Strains Near the End of a Crack Traversing a Plate," Transactions, Am. Soc. Mechanical Engineers, J. App. Mech., Vol. 24, 1957.

102. Bartholome, G., and Dorner, H., "Safety Evaluation of Nuclear Reactor Pressure Vessels for Pressurized Water Reactors," Practical Application of Fracture Mechanics to Pressure-Vessel Technology, The Institute of Mechanical Engineers, 1971.

103. Tada, H., The Stress Analysis Handbook, Del Research Corporation, Hellertown, Pa., 1973.

104. Wells, A. A., Br. Welding Journal, May 1968.

105. Begley, J. A., and Landes, J. D., "The J Integral as a Failure Criterion," Westinghouse Scientific Paper ul-iE7-FMPWRP-3, May 1971.

106. Rice, J. R., "A Path Independent Integral and the Approximate Analysis of Strain Concentration by Notches and Cracks," Trans. ASME, J. Appl. Mech., Vol. 90, Series E, 1968.

107. Williams, M. L., "On the Stress Distribution at the Base of a Stationary Crack," Trans. ASM, J. of Applied Mech., Vol. 24, No. 1, 1957.

108. Orowan, E., "Fracture and Strength of Solids," Report on Progress in Physics, Physics Soc., London, Vol. 12, 1949.

109. Murray, W. M. (ed.), Fatigue and Fracture of Metals, John Wiley, New York, 1952.

110. Davidge, R. W., and Evans, A. G., "The Strength of Ceramics," Mater. Sci. Eng., 6, 1970.

111. Evans, A. G., and Davidge, R. W., "The Strength and Fracture of Stoichiometric Polycrystalline UO_2," S. of Nucl. Mater., 33, 1969.

112. Mager, T. R., and Riccardella, P. C., "Use of Linear Elastic Fracture Mechanisms in Safety Analysis of Heavy-Section Nuclear Reactor Pressure Vessels," Practical Application of Fracture Mechanisms to Pressure-Vessel Technology, The Institute of Mechanical Engineers, 1971.

113. Roberts, J. T. A., and Voglewede, J. C., "Application of Deformation Maps to In-Reactor Behavior of Oxide Fuels," Journal of the American Ceramic Society, Vol. 56, No. 9, September 1973.

114. Hanson, J. E., Hanford Engineering Development Laboratory, private communication.

115. McCarthy, J. R., and Wolf, H., "The Heat Transfer Characteristics of Gaseous Hydrogen and Helium," Rocketdyne Research Report No. RR-60-12, December 1960.

116. Blaud, J. G.; Kalthoff, J. F.; and Stahn, D., "Model Experiments for Thermal Shock Fracture Behavior," Journal of Engineering Materials and Technology, October 1974.

117. Hsu, L. C., "An Analytic Study on Brittle Fracture of GE-BWR Vessels Subject to the Design Basic Accident," General Electric Atomic Power Equipment, San Jose, July 1969.

118. Chow, C. L., and Lam, P. M., "Stability Conditions in Quasi-Static Crack Propagation for Constant Strain Energy Release Rate," Journal of Engineering Materials and Technology, January 1974.

119. Hasselmen, D. P. H., "Crack Propagation Under Constant Deformation and Thermal Stress Fracture," Int. Journal of Fracture Mech., Vol. 7, No. 2, June 1971.

120. Svoboda, Milan, "Experimental Results on the Influence of Thermal Stresses on the Stability of a Crack," Int. Journal of Fracture Mech., Vol. 5, no. 4, December 1969.

121. Knudsen, F. P., "Dependence of Mechanical Strength of Brittle Polycrystalline Specimens on Porosity and Grain Size," J. Am. Ceramic Society 42 (8), 376-87 (1959).

122. Knudsen, F. P.; Parker, H. S., and Burdick, M. D., "Flexural Strength of Specimens Prepared from Several Uranium Dioxide Powders; . . ." J. Am. Ceramic Society, 43 (12), December 1960.

123. Cannon, R. F., Roberts, J. T. A., and Beals, R. J., "Deformation of UO_2 at High Temperatures," J. Am. Ceramic Society, 54 (2), February 1971.

124. Roberts, J. T. A., and Veda, Y., "Influence of Porosity on Deformation and Fracture of UO_2," Journal of the American Ceramic Society, 55 (3), March 1972.

125. Miller, R. R. (ed.), Liquid Metals Handbook, AEC and BuShips, Washington, DC (3rd edition), June 1955.

126. Lazarrus, J.; Navarre, J. P.; and Kottowski, H. M., "Thermal Interaction Experiments in a Channel Geometry Using Al_2O_3 and Na," paper presented at the Fuel Coolant Interaction Meeting, Ispra, 21-23 November, 1973.

127. Davidge, R. W., and Tappin, G., "The Effects of Temperature and Environment on the Strength of Two Polycrystalline Aluminas," Proc. of the British Ceramic Society, No. 15, January 1970.

128. Gitzen, W. H. (ed.), Alumina as a Ceramic Material, American Ceramic Society, Columbus, Ohio, 1970.

129. Liebowitz, H., Fracture, Vol. VII, Academic Press, N.Y., 1972.

130. McClintock, F., private communication.

131. Lynch, J. F., Ruderer, C. G., and Duckworth, W. H., "Engineering Properties of Ceramics," Battelle Memorial Institute, Tech Report AFML-TR-66-52, June 1966.

132. Bolz, R. F., and Tine, G. L. (eds.), Handbook of Tables for Applied Engineering Science, The Chemical Rubber Co., Cleveland, Ohio, 1973.

133. Mantell, C. L. (ed.), Engineering Materials Handbook, McGraw-Hill, N.Y., 1958.

134. Tao, L. C., "Generalized Numerical Solutions of Freezing a Saturated Liquid in Cylinders and Spheres," AIChE Journal, Vol. 13, No. 1, January 1967.

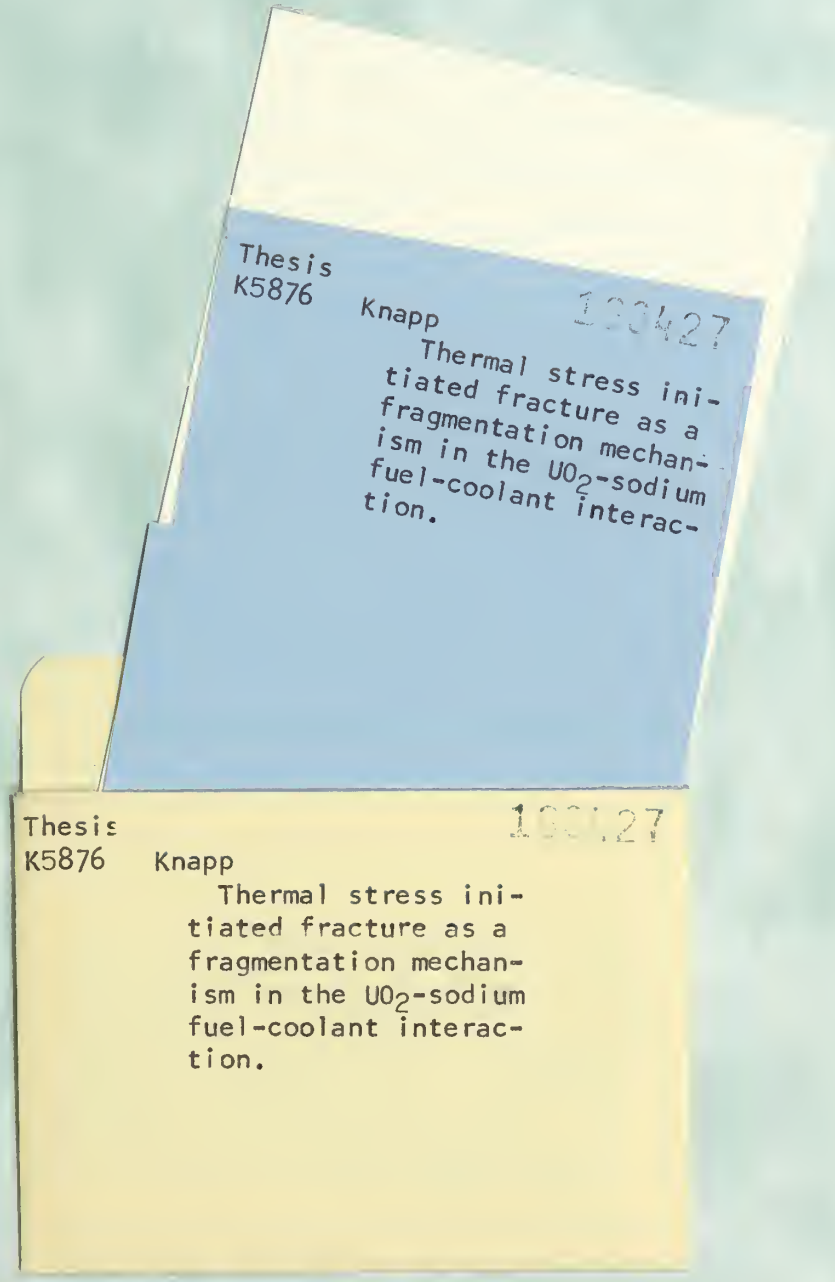
Thesis
K5876
Knapp
Thermal stress initiated fracture as a fragmentation mechanism in the UO_2-sodium fuel-coolant interaction.
Thesis
K5876
Knapp
Thermal stress initiated fracture as a fragmentation mechanism in the UO_2-sodium fuel-coolant interaction.